INVESTIGATING MARINE PARTICLE DISTRIBUTIONS AND PROCESSES USING *IN SITU* OPTICAL IMAGING IN THE GULF OF ALASKA

By

Jessica S. Turner

RECOMMENDED:

Dr. Ana Aguilar Islas

Dr. Mark Johnson

Dr. Andrew McDonnell
Advisory Committee Chair

Dr. Katrin Iken
Program Head, Marine Sciences and Limnology

APPROVED:

Dr. Joan Braddock
Interim Dean, School of Fisheries and Ocean Sciences

Dr. John Eichelberger
Dean of the Graduate School

7 December 2015

Date

INVESTIGATING MARINE PARTICLE DISTRIBUTIONS AND PROCESSES USING *IN*

SITU OPTICAL IMAGING IN THE GULF OF ALASKA

A

THESIS

Presented to the Faculty

of the University of Alaska Fairbanks

in Partial Fulfillment of the Requirements

for the Degree of

MASTER OF SCIENCE

By

Jessica S. Turner

Fairbanks, AK

December 2015

Abstract

The Gulf of Alaska is a seasonally productive ecosystem surrounded by glaciated coastal mountains with high precipitation. With a combination of high biological production, inputs of suspended sediments from glacial runoff, and contrasting nutrient regimes in offshore and shelf environments, there is a great need to study particle cycling in this region. I measured the concentrations and size distributions of large marine particles (0.06-27 mm) during four cruises in 2014 and 2015 using the Underwater Vision Profiler (UVP). The UVP produces high resolution depth profiles of particle concentrations and size distributions throughout the water column, while generating individual images of objects >500 μm including marine snow particles and mesozooplankton.

The objectives of this study were to 1) describe spatial variability in particle concentrations and size distributions, and 2) use that variability to identify driving processes. I hypothesized that UVP particle concentrations and size distributions would follow patterns in chlorophyll a concentrations. Results did not support this hypothesis. Instead, a major contrast between shelf and offshore particle concentrations and sizes was observed. Total concentrations of particles increased with proximity to glacial and fluvial inputs. Over the shelf, particle concentrations on the order of 1000-10,000/L were 1-2 orders of magnitude greater than offshore concentrations on the order of 100/L. Driving processes over the shelf included terrigenous inputs from land, resuspension of bottom sediments, and advective transport of those inputs along and across the shelf. Offshore, biological processes were drivers of spatial variability in particle concentration and size. High quantities of terrigenous sediments could have implications for enhanced particle flux due to ballasting effects and for offshore transport of particulate phase

iron to the central iron-limited gyre. The dominance of resuspended material in shelf processes will inform the location of future studies of the biological pump in the coastal Gulf of Alaska. This work highlights the importance of continental margins in global biogeochemical processes.

Table of Contents

List of Figures

Page

List of Tables

Introduction

Particles and the Biological Carbon Pump

What is a particle? Marine particles are objects in seawater that range in size from microscopic to visible with the naked eye. Phytoplankton and their skeletons, fecal pellets from zooplankton, aggregates of detritus, and inorganic grains derived from continental crust are all considered particles. Operationally defined, a particle is anything that can be trapped on a filter, in size classes ranging from 0.02 μm, just larger than colloidal substances, to macro-particles several cm in size. These particles are essential to global carbon cycling and regional ecosystem functioning.

Marine particles sequester atmospheric carbon dioxide and thus help to regulate global climate. After photosynthetic organisms take up carbon dioxide from the atmosphere and incorporate it into their bodies, those organisms and their skeletons sink through the water column as marine particles. Some of those particles eventually reach depths at which the organic carbon can be stored on longer time scales. This phenomenon is called the biological carbon pump (Broecker, 1982; Siegenthaler and Wenk, 1984; Volk and Hoffert, 1985).

Marine particles also play an important role in ecosystem function. In coastal and shelf systems, sinking particles are an important food source for benthic organisms. For example, the shallow shelves of the Bering and Chukchi Seas host a rich biomass of benthic organisms due to the annual pulse of sinking particulate matter from the surface rich in nutrients and carbon (Grebmeier et al., 1988). In the deep ocean, pelagic and benthic organisms rely on sinking organic matter as a habitat and a food source. Large marine snow particles are often colonized by deep sea bacteria and zooplankton, and thus considered islands of biological activity and diversity in the relatively homogenous deep sea. Concentrations and diversities of bacteria on

1

particles were much higher than those of free-living organisms, and zooplankton fecal pellets'

chemical signatures confirmed that grazers consume bacterially-colonized marine snow particles

(Lampitt et al., 1993; Silver, 1978). Sinking particles enhance the health of both deep-sea and

benthic communities.

Although organic matter is the main focus of the biological carbon pump, inorganic

particles play an important role in the transfer of material from the surface ocean to depth.

Inorganic particles have a ballasting effect on organic matter, including silicate and calcium

carbonate planktonic skeletons, as well as lithogenic clays, silts and sands transported from land

by rivers and winds (Armstrong et al., 2001; Klaas and Archer, 2002). These minerals can help

protect the organic matter from bacterial remineralization, and can increase the density of the

resulting aggregates to enhance their sinking rates (Ittekkot, 1993; Iversen and Ploug, 2010). In

this way inorganic and lithogenic particles are meaningful components of the biological carbon

pump.

Size Contributions to the Biological Pump

The strength of the biological carbon pump is greatly influenced by the size distributions

of the objects produced at the surface. Historically, much work has gone into distinguishing

which size classes contribute most to the flux of particulate organic carbon (POC) from the

surface to the deep sea. Some studies show that smaller particles (<100 μm) play an important

role in carbon flux. For example, 0.2-20 μm particles contributed to carbon flux during surface

phytoplankton blooms in the Norwegian Sea (Dall'Olmo and Mork, 2014), and 11-64 μm

particles made up over a third of total carbon flux at several temperate stations in the Atlantic,

with the small-particle contribution increasing in importance with depth (Durkin et al., 2015).

Even picoplankton cells <0.5 μm are an important source of the sinking carbon that is incorporated into the zooplankton-driven and detritus-driven portions of overall sinking particle flux (Richardson and Jackson, 2007). However, most studies agree that the greatest contribution to flux overall comes from large (>100 μm) particles (Fowler and Knauer, 1986; McCave, 1975; Riley et al., 2012; Stemmann et al., 2008). In particular, a size range of particles that are both relatively large (0.2 – 0.8 mm) and more abundant than the very large, rare particles (>1 mm) make up a considerable portion of particle flux to depth. For example, particles sized ~0.5 mm made up the highest proportion of the mass spectrum in the Mediterranean Sea (Stemmann et al., 2004), medium-sized particles (0.2 – 0.8 mm) made up more of the volume flux than other size classes in the Southern Ocean (Ebersbach and Trull, 2008), and carbon flux was dominated by particles between 320 and 520 μm in the Sargasso Sea (McDonnell and Buesseler, 2012). Ideal investigation of particles should target all sizes from the submicron scale to several cm, but unfortunately, no instrument yet exists to sample such a wide size range (Stemmann and Boss, 2012). To learn the most about carbon transfer processes from only one sub-range of particle size classes, middle-to-large size classes (100 μm – 1 mm) merit study as the greatest contributors to flux.

The dynamics of large particles such as aggregates and marine snow, including how they are formed near the surface and slowly broken apart with depth, are driven by interactions between organisms in the upper 1000 m of the water column (Burd and Jackson, 2009). Phytoplankton cells and zooplankton fecal pellets in the surface ocean coagulate into larger particles, by way of physical shear or differential sinking velocities. Small particles collide physically via Brownian motion, while larger particles collide due to laminar and turbulent fluid shear. Different sizes also coagulate due to their differential sinking velocities, when faster-

sinking particles catch up to slower-sinking particles and incorporate them (Elimelech et al., 1995; Freidlander, 2000; McCave, 1984). Those aggregates are later broken apart by physical disaggregation, microbial respiration, and zooplankton interactions. Marine snow physically disaggregates when the surface of the particles is eroded, when there is differential pressure across the particle, or when the particle fractures (Parker et al., 1972). However, models and observations agree that relatively high turbulent force is required to break apart aggregates (turbulent energy dissipation rates up to $10^{-4}\,\mathrm{m^2/s^3}$), especially to break up aggregates formed from sticky zooplankton feeding matrices (Alldredge et al., 1990; Jackson, 1995). Biologically, large particles disaggregate through microbial decomposition when bacteria directly metabolize and solubilize the material (Grossart and Simon, 1998; Smith et al., 1992). Lastly, zooplankton fragment large particles via direct grazing, sloppy feeding behavior, and micro-turbulence caused by their swimming motion (Dilling and Alldredge, 2000; Dilling et al., 1998; Goldthwait and Yen, 2004). Zooplankton also repackage larger aggregates into smaller, denser, rapidly-sinking fecal pellets (Kiørboe, 2001; Lampitt et al., 1990). Overall the aggregation and disaggregation of marine snow particles involves many complex processes, highlighting the importance of measuring the concentrations and size distributions of these relatively large particles.

Measuring Sinking and Suspended Particles

Marine particle fluxes and concentrations are surprisingly hard to quantify. Sinking particles are measured as a flux, while suspended particles are measured as a concentration. These parameters are measured separately and are related by the equation $F = w * c$ (e.g. Bishop et al., 1986), where F is flux, w is particle settling velocity, and c is concentration. Thus, the flux of particles to depth depends not only on the number of particles present, but also on

4

those particles' settling velocities, based on their size, mass and the viscosity of seawater according to Stokes' Law and its many applications (McCave, 1975). Although Stokes' Law cannot fully explain sinking rates of all size classes (Burd and Jackson, 2002), particle mass, size, density, and morphology are crucial to their ability to carry carbon to the deep ocean. Large, dense particles enhance the carbon pump because their greater density allows them to sink before they can be remineralized, with the largest marine snow particles sinking faster than 100 m per day (Alldredge and Gotschalk, 1988; Peterson et al., 2005). In contrast, smaller, lighter objects such as single phytoplankton cells sink as slowly as <1 m per day (Smayda, 1969). The proportion of quickly sinking particles in a given ecosystem is a major driver of that system's carbon export to depth.

Historically, fluxes of sinking particles to depth have been measured using conical or cylindrical shaped sediment traps to capture falling particles. These traps are moored to the ocean floor, free-drifting at a certain depth, or neutrally buoyant in the water column. To tackle the challenges posed by sediment traps, such as degradation of the material and the accidental entrapment of zooplankton swimmers, traps contain poison and gels to preserve particles and discourage consumers (Buesseler et al., 2007). Chemically, POC export to depth has been measured using the disequilibrium between Uranium-238 and Thorium-234 as a proxy for particle scavenging by Thorium-234. Though this particle-reactive tracer method accurately predicted POC fluxes from surface waters, it was less accurate at intermediate depths of 150-300 m and did not effectively tackle the problem of particle size classes (Buesseler et al., 1992). Measuring sinking particle fluxes is integral to understanding the strength of the biological carbon pump.

Many particles' small sizes, fragile structures or low densities cause them to be suspended in the water column rather than sinking through it, so they do not make up part of the flux to depth as they are not collected by sediment traps. These suspended or neutrally-buoyant particles are made up largely of transparent exopolymeric (TEP) gel substances. Although usually smaller than 100 μm, suspended particles can be as large as several cm (Baltar et al., 2010; Verdugo et al., 2004). Suspended particles have different compositions from sinking particles, and often contain more "fresh" phytoplankton cells and aggregates (Abramson et al., 2010). A very important habitat and food source for microbial life forms, most suspended particles are remineralized by bacteria and metazoans in the mesopelagic "twilight zone" between the base of the euphotic zone and 1000 m depths (Arístegui et al., 2009; Baltar et al., 2009; Riley et al., 2012). Concomitant measurements of sinking particles and suspended particles in the northeast Atlantic showed that suspended particles outnumber sinking particles by 2 orders of magnitude (Baltar et al., 2010). Globally, suspended particles remain mostly unquantified (Arístegui et al., 2009; Baltar et al., 2009; Burd and Jackson, 2009), and constraining the populations of suspended or slowly settling particles could help complete many regional carbon budgets (Burd et al., 2010).

To capture suspended particles, seawater can be collected in Niskin bottles or filtered through *in situ* pumps to analyze the amount of particulate matter in a known volume. Particle concentrations are measured to determine the total amount of particulate organic matter (POM), and this particulate matter can also be analyzed for chemical composition in terms of carbon, macronutrients, and trace metals. However, marine snow particles tend to settle within bottles and stick to the sides, causing an underestimation of particle concentration and a bias in size classifications (McDonnell et al., 2015). *In situ* pumps sample a larger volume than Niskin

bottles, but rapid filtration speeds can fragment particles and larger size classes can be lost with this method as well (Bishop et al., 2012). To improve the quantification of these elusive suspended particles, the concentration of particles in the water column needs to be measured using non-destructive methods.

Optical Imaging of Particles

As an alternative to the physical collection of particles, optical instruments and imaging systems have provided researchers with a way to sample sinking and suspended particulate matter *in situ* without using bottles, filters, or traps. The optical instruments most frequently used in conjunction with CTD rosettes sample subsections of the array of particles in the water column based on their designs. *In situ* fluorometry measures the concentration of small objects based on the fluorescence of the pigments in living cells. Fluorometry can overestimate small size classes of phytoplankton because smaller cells fluoresce more per unit chlorophyll *a* than larger cells, and fluorometry does not detect detrital particles that are no longer actively fluorescing (Alpine and Cloern, 1985). Transmissometry measures the amount of light scattered and absorbed by particulate, dissolved and colloidal substances. Transmissometers' pathlengths have very small acceptance angles, causing them to target the smaller cells and particles <100 μm (Boss et al., 2009). More advanced optical instruments expand on the scattering technique to calculate the sizes of particles passing a laser beam, although they are still most accurate for objects <100 μm (Boss et al., 2015). Imaging systems photograph objects in addition to measuring their basic light-scattering properties. Flow-cytometry systems were designed to image phytoplankton, while several stationary or depth-profiling camera systems were designed to target larger objects such as zooplankton, ichthyoplankton, and large detrital particles (see

Chapter 1 of this thesis). Most of these imaging systems require inefficient processing time because they create an excess of unfocused images, and most systems lack a large sampling volume (Picheral et al., 2010).

Statistically, a large sampling volume is needed to capture particle counts sufficient for statistical analysis. Because the large, rapidly-sinking particles that contribute so strongly to vertical POC flux are relatively rare, large volumes of water need to be sampled to find a representative number of the large aggregates (Burd et al., 2007; McCave, 1975; Walsh and Gardner, 1992). When counting the particles of different size classes, error is the square root of the total count per Poisson distribution counting statistics (Young, 1962). To quantify the spatial variability in particle size distributions, I needed to minimize error, because I could only quantitatively say that certain depths and stations had different particle concentrations or size distributions if the ranges of error for those particle counts did not overlap. My goals were to obtain detailed concentrations and size distributions of large particles (>100 m) from hundreds of full water column depth profiles with minimal sampling error.

Here I used the Underwater Vision Profiler (UVP), manufactured by Hydroptic, Inc. in Villefranche, France. The UVP is a digital camera that photographs 1-liter parcels of water during descent, counts and calculates size classes of all particles (0.06-27 mm; Figure 0.1) within the photographs, and creates images of all the largest objects (>0.5 mm). Unlike other optical methods and imaging systems, the UVP has both a fine enough resolution to detect small particles (to 60 μm) and a large enough image volume to detect large objects (to ~3 cm), while also maintaining a fast enough sampling frequency to capture thousands of photographs during descent through the water column (Picheral et al., 2010; Stemmann et al., 2008). This large sampling volume and high number of photographs is important for the statistical quantification

of particles. The high counts yielded by the UVP decrease the error in counting statistics,

allowing me to confidently assess differences between depths and regions.
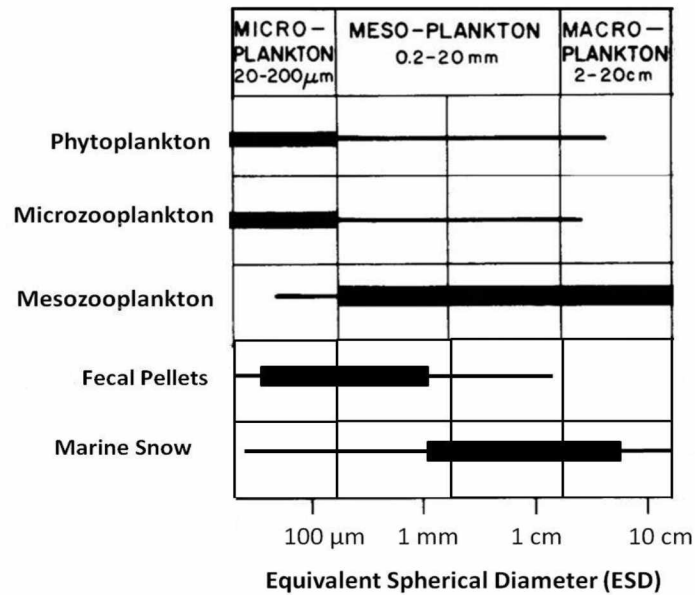
Figure 0.1. Types of particles that are detected by the UVP based on their size, within the range of 60 μm to several cm. (Marine snow size estimates from Kilps et al., 1994; figure adaption and planktonic size estimates from Sieburth and Lenz, 1978; fecal pellet size estimates from Smayda, 1969).

Past Research Using the UVP

Although the UVP is a relatively new optical instrument, it has already been deployed in

many parts of the world. Of the multiple versions of the UVP that have been used, only those

studies that used the same model as my study, the UVP 5, will be discussed here. In the

southeastern Pacific, the UVP was used alongside a HIAC/Royco particle counter to span a large

range of particle sizes (3.5-2000 μm). The number spectrum generated by UVP counts was

sufficient to estimate particle mass, and that the total mass of large particles >100 μm was

roughly equal to the mass of smaller particles (Stemmann et al., 2008). That study also

compared UVP data to sediment trap fluxes and concluded that large particulate matter (LPM)

export is spatially heterogeneous because it is mediated by many abiotic and biotic factors (Guidi et al., 2008a). A California Current System study using the UVP observed an increase in organic aggregates at a deep-water front (Ohman et al., 2012). When the UVP was deployed in the Canadian Arctic (Beaufort Sea), researchers found that both the mean size of particles and the percentage of >500 μm particles identifiable as mesozooplankton increased with distance from shore. They also found lower sediment trap fluxes in locations where copepods were more abundant in both UVP images and net tows (Forest et al., 2013, 2012). In the Southern Ocean near the Kerguelen Plateau, the UVP was used to assess temporal variability at one station before and after a bloom event, and showed that the greatest volumes of particles at depth were slightly lagged behind high surface chlorophyll *a* values over a 48 hour period (Jouandet et al., 2014). In the Persian Gulf of the Arabian Sea, oxygen minimum zone stations were also characterized by a greater proportion of large particles at all depths seen with the UVP, suggesting greater large particle export to depth in those areas. Low counts of zooplankton in the UVP large-particle images on this cruise made them turn to net tows instead of the images for zooplankton abundances (Roullier et al., 2014). In the subtropical North Pacific just off the coast of Hawaii, UVP-derived POC flux was estimated alongside sediment traps, sea surface height, and *Trichodesmium spp.* abundances. A convergent zone between two mesoscale eddies was found to physically mediate POC export by downwelling (Guidi et al., 2012). Guidi et al. (2008b) combined many of these datasets in a global comparison with sediment trap fluxes to create an empirical relationship that can be used to calculate flux from UVP concentration size distributions alone. This empirical relationship was used to calculate flux estimates by Jouandet et al. (2014) and Roullier et al. (2014). Furthermore, Guidi et al. (2009) combined the slopes of the UVP particle size distributions at all profiles in their global dataset to look at the widespread

patterns in the shape of the depth profiles of size distributions. The overall patterns revealed that particle size distributions and estimated flux at 400 m depths were intrinsically related to phytoplankton community compositions in the overlying euphotic zone. Although the UVP has been used in Southern, Arctic, North Atlantic, and subtropical Pacific oceans, as well as the Mediterranean and Arabian seas, it has not yet been deployed in the higher latitudes of the North Pacific.

The Gulf of Alaska

Physically, the study region is a high-latitude ocean surrounded by glaciated coastal mountains with high precipitation. Diffuse coastal rivers and streams having discharge rates up to 23000 m^3 per second (Royer, 1982) carry vast amounts of freshwater laden with suspended material into the Gulf of Alaska (GOA). The largest point-source input, the Copper River system, is estimated to contribute 107 million tons per year of suspended material (Feely et al., 1979; Reimnitz, 1966). Of the total freshwater discharge to the GOA, approximately 47% is sourced from glaciers and icefields, which cover an area larger than 75,000 km^2 (Neal et al., 2010). Approximately half of the runoff from glaciers to the GOA comes directly from tidewater glaciers, which can move significant amounts of sediment (Powell and Molnia, 1989; Syvitski, 1989). The high levels of seasonally-variable freshwater discharge help to force the Alaska Coastal Current (ACC) counterclockwise around the gulf, which is maintained by wind stress. Counterclockwise prevailing winds set up a sea-surface slope that drives downwelling over the shelf and upwelling in the center of the gyre. The ACC flows close to surface within 20-50 km of the shoreline (Royer, 2005, 1982, 1975). Offshore, the Alaska Stream flows in the same direction at ~150 m depth along shelf break (Feely et al., 1981). The coexistence of these two

parallel along-shelf currents unifies the GOA with the Bering, Chukchi and Beaufort seas, creating a widespread feature deemed the Riverine Coastal Domain (Carmack et al., 2015). Anticyclonic eddies generated nearshore transport coastal waters into the offshore environment, while storm and tidal mixing brings deep, offshore waters back onto the shelf via canyons and troughs (Crawford et al., 2007; Ladd et al., 2005; Tang et al., 2014).

Biologically, the coastal GOA is surprisingly productive for a downwelling system. Phytoplankton production is estimated to be at least 300 g C per m^2 each year (Sambrotto and Lorenzen, 1987). Seasonally, each year is marked by a spring bloom and smaller-magnitude fall bloom, the timing of which is extremely variable (Napp, 1996). Fresh spring melt and runoff stratify the water column nearshore to prompt the first pulse of the spring bloom, while warmer temperatures stratify the water column over the rest of the shelf slightly later. Away from the coast, the central GOA experiences wind-driven upwelling, increasing nutrient availability in the offshore environment. Given the discrepancy between high macronutrient concentrations and only moderately high production offshore, the central GOA is known as a high-nutrient-low-chlorophyll (HNLC) region (Martin et al., 1989). Both nearshore and offshore, the GOA supports significant zooplankton production dominated by large calanoid copepods (Coyle and Pinchuk, 2003; Hopcroft et al., 2010). This high production of zooplankton is an essential food source for many higher trophic level organisms, including several important fisheries (Coyle and Pinchuk, 2005), as well as marine mammals important to the tourism industry (Sharma et al., 1974). Hosting five species of pacific salmon, as well as cod, pollock, and many others, the GOA is one of the most economically productive fisheries in North America (Laevastu et al., 1979).

Past studies have investigated particle fluxes in the GOA using traditional methods such as geological surveys, water sampling, and sediment traps. In the coastal environment, moored sediment traps were placed nearshore in the northeastern gulf near Icy Bay, in which inorganic material from land dominated the bulk of the particulate matter collected (Landing and Feely, 1981). Offshore of this study's location, shipboard observations over the continental shelf included benthic surveys and water sampling to determine the nature of the suspended and shelf sediments. These shelf-based studies found that by dry weight, lithogenic material vastly overshadowed organic material in the traps, grabs, and water samples (Burbank, 1974; Feely and Massoth, 1982; Feely et al., 1981, 1979). In the offshore GOA, Station P or "papa" in the south-central GOA (49.904 N, 145.243 W) has for decades been the site of long-term particle flux studies using sediment traps (Takahashi et al., 2002; Wong et al., 1999). Particles in the GOA have also been studied from a trace-metal perspective, particularly with regards to iron. VERTEX cruises studied carbon cycling in the GOA to investigate the Martin iron hypothesis (1987), followed by a series of iron fertilization experiments that measured post-bloom sedimentation using drifting sediment traps (Boyd et al., 2005).

In the present study of marine particles, I will discuss the optical imaging method used and present the results of my research in the GOA in 2014 and 2015. The following chapters will focus on 1) improvements in knowledge of the methodology and operation of the UVP during trials in different oceanographic environments, and 2) the drivers of spatial patterns in particle concentrations and size distributions measured with the UVP in the GOA. My hypothesis, that particle concentrations and size distributions collected with the UVP would follow patterns in chlorophyll a and zooplankton abundances, was supported only in the offshore

13

environment, while processes over the shelf were instead driven by physical processing such as

river discharge, glacial runoff, and resuspension of bottom sediments by mixing forces.

Chapter 1   Using the Underwater Vision Profiler as an oceanographic tool for the study of

marine particles

Abstract

The Underwater Vision Profiler (UVP), an innovative tool for the study of marine particles 60 μm to 2.7 cm in size, produces high resolution depth profiles of particle concentrations and calculates their size classes throughout the water column. The UVP also generates individual images of objects >500 μm such as marine snow particles and mesozooplankton. This *in situ* camera excels at measuring particles and zooplankton that are often overlooked by traditional methods of particulate matter collection with *in situ* filtration pumps, bottles, and net tows. To validate and facilitate the use of the UVP by the McDonnell laboratory at the University of Alaska Fairbanks, I tested this instrument in the Gulf of Alaska and the Pacific Ocean, wrote code to process the numerical datasets, and created step-by-step documentation for deployment and data processing. This chapter will discuss what I have learned about working with the UVP over the course of several cruises in different oceanographic environments.

Methods

The UVP was deployed in the New York/New Jersey Bight in October 2013, on the Seward Line in May 2014* and September 2014*, in the Beaufort Sea in August 2014, on the 152°W line in the Pacific Ocean on the CIVAR Repeat Hydrography P16N cruise in March-June 2015*, and in the coastal Gulf of Alaska (GOA) in July-August 2015. I participated in three of these cruises (marked*), and helped with the other three by analyzing data and/or mentoring the

student field technicians for the other three cruises. The following methods detail the basic operations of the camera, data storage format, concentration calculations, selection of the downcast using descent rate, size class calculations, the image sorting process, and other methods used alongside the UVP. For more information, Appendix I contains thorough step-by-step instructions for UVP deployment and data analysis.

The Underwater Vision Profiler

The UVP was designed to detect and photograph objects 60 µm to 27 mm in diameter within rectangular 1-liter water parcels during descent through the water column (Picheral et al., 2010). The known image volume used for the calibration of the instrument (0.93 L) was mapped in an indoor testing tank based on the characteristics of the light field. Particle counts for this camera system (serial number 009) were adjusted relative to the original UVP camera using a side-by side deployment in the Mediterranean Sea. This known volume was used to calculate particle concentrations. Although the exact volume of each image was 0.93 L, I will refer to the photographed water parcels as 1-liter images throughout this text. Each water parcel was a rectangular prism 12.8 cm wide, 9.6 cm long, and 3.5 cm deep in the vertical direction. To capture each 1-liter image, two LED lighting units flashed red light (625 nm wavelength) into a rectangular prism of water to illuminate the objects within it (Figure 1.1). At a fixed distance of 365 mm from these flashing lights, the 1.3-megapixel camera was optically configured to detect objects within the image volume that scatter light towards the camera. It was designed to detect objects 60 µm to 2.7 cm in diameter, including particles smaller than an individual pixel because of the way they scatter light from the LED strobes. As the UVP descended through the water column, the camera captured approximately 11 1-liter images per second, or one image every 9

16

cm at a descent rate of 1 m/s. The instrument is versatile and can be deployed alone in its own frame (Figure 1.1) or mounted on a CTD rosette frame, since it works in sync with SeaBird CTD equipment. Its small size (1 m in height, 35 cm in diameter at the base) and weight (30 kg) allows it to be easily accommodated into CTD rosette frames of various sizes (Figure 1.1).
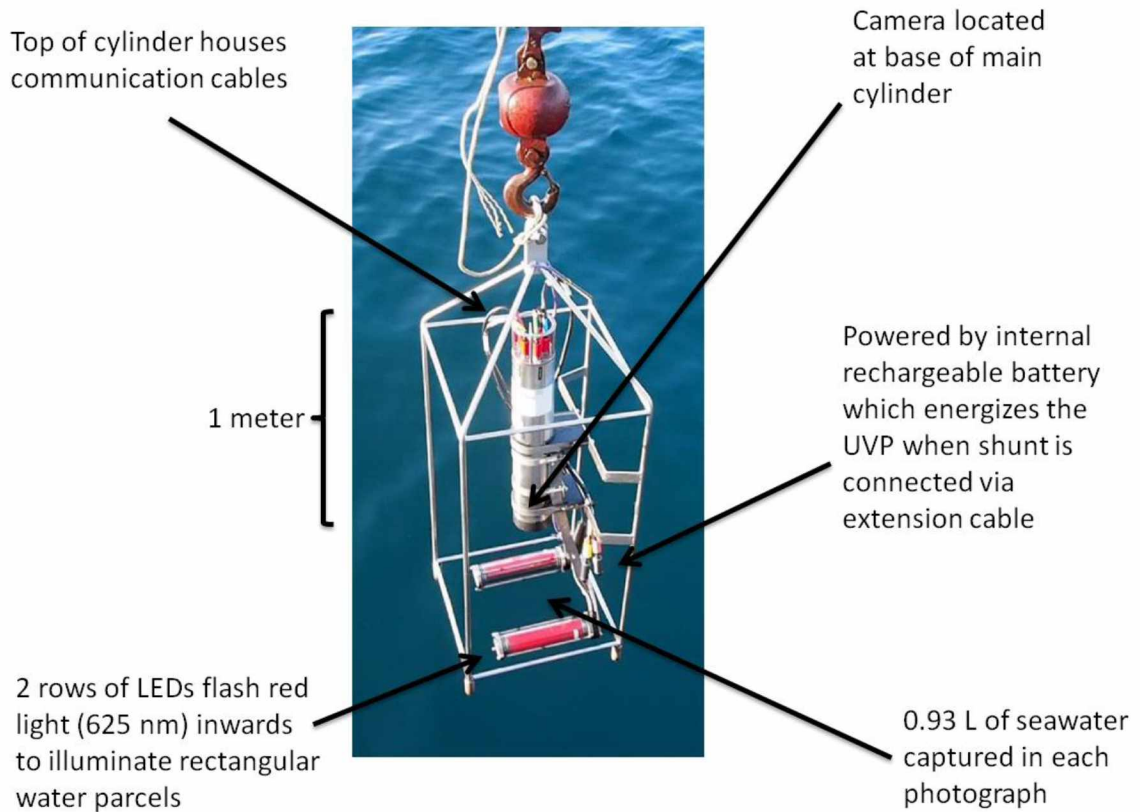
Figure 1.1. Major features of the Underwater Vision Profiler 5 (UVP), pictured when deployed separately from the CTD rosette in May 2014 in the coastal Gulf of Alaska.

Based on the 1-liter images, the UVP counted particles, calculated their sizes in pixel area, and generated photographs of objects larger than a certain user-defined diameter (i.e., >500 μm). The large-object photographs, called vignettes, were saved as individual black-and-white 8-bit jpegs labeled with a scale bar, the 1-liter image in which it was detected, the station number, and the depth at which it was photographed (Figure 1.2).
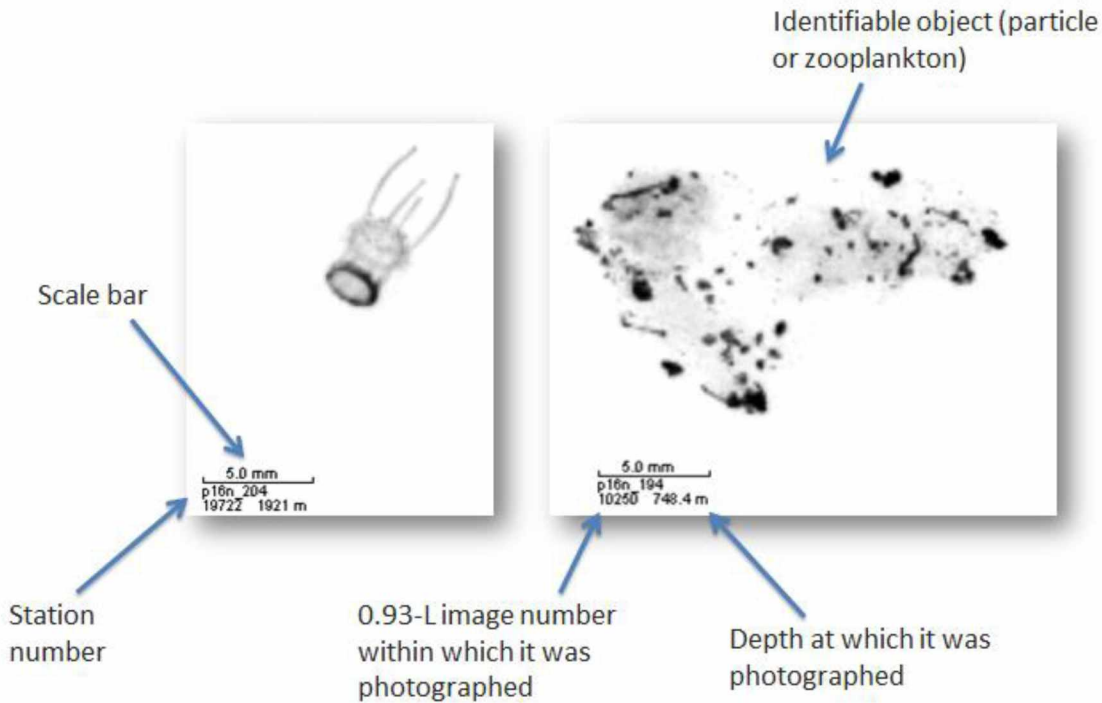
Figure 1.2. Example vignettes and their features, generated by the UVP at two offshore stations in the central Gulf of Alaska, showing a medusa (left) and a marine snow particle (right).

This instrument was powered by an internal 7-celled lithium-ion battery. While storing the UVP on deck between casts, it was recharged using the extension cables and the deck unit. While the manufacturer recommended recharging the battery at least every 12 hours, I found in the field that it was best to recharge the battery after every cast, if possible. The battery was most depleted after very deep casts (>4000 m). When the instrument ran out of battery power during a cast, it caused the camera power to flicker on and off and to go in and out of acquisition mode, storing multiple cast data files for many portions of the same cast. Also, I found that the battery cells could become unbalanced, causing the instrument's maximum internal voltage to drop, which limited sampling time before the camera turned off due to insufficient voltage. To

fix this battery malfunction, I discharged all the stored voltage from the battery cells using computer fans, then recharged the battery fully so all cells had the same level of charge.

The camera was configured to begin sampling using one of two methods, either manually plugging in shunts or programming it to begin sampling autonomously using pressure cues. The first method, called input/output (I/O) mode, involved using the yellow colored shunt to put the camera into acquisition mode so that the lights flashed to actively take photographs before the instrument was submerged. I/O mode was most useful for very shallow stations (<100 m) when it was more efficient in terms of time, as opposed to taking the time to lower the CTD rosette to the soaking depth used in deeper casts. However, there was a time lapse of several minutes between when the I/O shunt was plugged in and when the LED lights actually began flashing, thus extending deck time and delaying the deployment of the rosette. For most deployments, especially in deeper waters, the most efficient configuration for the camera was depth mode. Depth mode required programming the camera with pilot tools through the Zooprocess software to set descent and ascent signals for the instrument's internal pressure sensor, based on the sampling plan for each cruise. For example, a descent signal of 30 decibars was appropriate for the P16N cruise in the North Pacific where 30 m was the standard CTD soaking/rinsing depth. In depth mode, I performed a surface check to make sure the LED lights were flashing before the rosette made its full water column descent.

In terms of data acquisition, the UVP was operated in mixed acquisition mode, although different acquisition modes could be used depending on location of the cruise and the sampling goal. The three different data acquisition modes available were *fullhd*, *mixthd*, and *mixtfd*. In the full mode, the UVP would save every 1-liter images as well as the computed concentrations, size information, and vignettes for each cast, a much slower process with an acquisition rate of 3 Hz.

In the mixed modes that I used, in which raw data were stored on the hard drive or the flash drive of the instrument, the UVP saved only the numerical data for concentrations and sizes along with the vignettes of the largest objects. This allowed for a faster acquisition rate of up to 11 Hz. Therefore, using mixed acquisition mode was the most efficient way to collect data, since it saved data storage space while still generating high-resolution particle size distribution data and individual vignettes of larger particles (>0.5 mm). In one downcast in mixed acquisition mode, the UVP can photograph many thousands of images, capturing the dimensions of millions of individual particles and saving thousands of individual vignettes of the largest particles. Although the UVP's storage capacity of 8GB did provide enough space to store all the profiles from a 1-2 week cruise using mixed acquisition mode, storing a lot of data on the instrument limited downloading efficiency. Thus the data collected in mixed acquisition mode were both detailed enough for solid statistical analysis without compromising file storage space on the instrument.

Data Storage Format

Understanding how this sophisticated camera and its software store data was one of the most challenging aspects of testing the UVP. Data were analyzed on PC computers using Zooprocess software, a macro plugin for Java-based image-processing program ImageJ. Within the Zooprocess software, using pilot tools to directly access the camera flash drive and hard drive, I downloaded the data stored on the camera in one folder per cast filled with all of the raw 1-liter image files. Raw data were stored in one folder for each cast, labeled with the date and time of the cast in Greenwich Mean Time (GMT). To unpack what was "seen" in each cast, I processed the data in Zooprocess through two sequences. With the first sequence, numerical

particle data were processed to eliminate superfluous data and calculate concentrations and size distributions using the numerical .txt files and .bru files (see Appendix I for more information on processing steps). With the second sequence, the large-object images were processed into individual .jpeg vignettes and .PID files, which were later sorted using Plankton Identifier (PID) software.

The central axis of the data organization format was the project folder for each cruise. In this project folder, three separate pre-made folders contained the raw data, the processed data, and the image identification portion of the analysis (Figure 1.3). During some processing steps, Zooprocess software made multiple copies of processed files, placing these other copies in different sections of the project folder. After processing the numerical particle data and sorting the vignettes, a single project folder from each cruise was typically 20-30 GB in size.
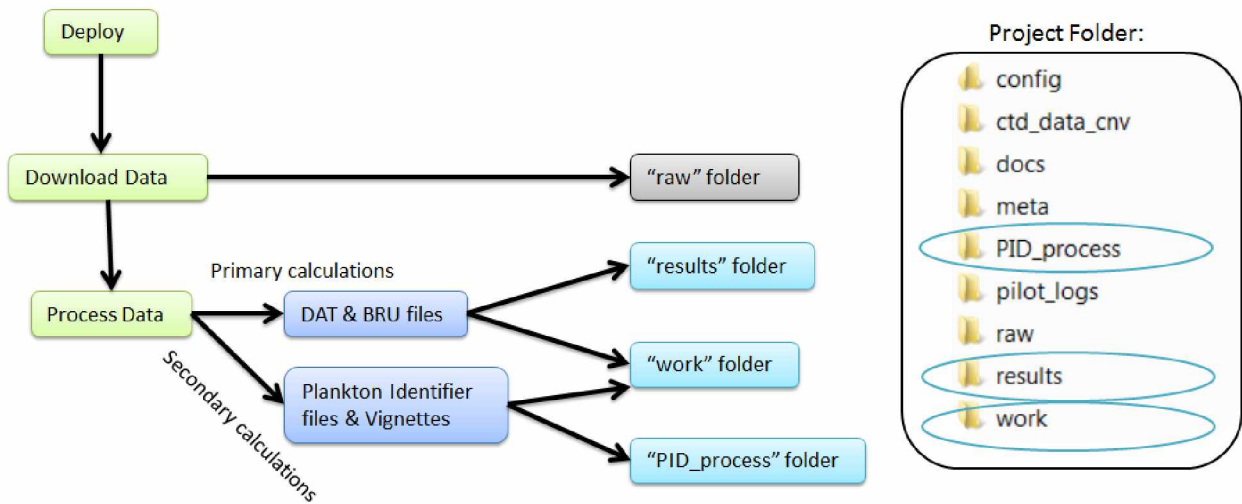
Figure 1.3. Data processing flowchart and contents of a single-cruise project folder. Folders circled in blue contain the information available for data analysis. Analysis of particle concentrations and size distributions draws information from the "results" and "work" folders, while sorting of images draws from the "work" and "PID_process" folders.

Calculating Particle Concentrations

Concentration in this study was calculated as a count per unit volume, or the number of particles detected within the measured volume of seawater photographed (#/L). Therefore, concentration as a count was analyzed using Poisson distribution counting statistics (Young, 1962), where the greatest counts yielded the lowest errors and the smallest counts yielded the highest errors.

$$E = \sqrt{n}$$

where E is the standard error and n is the number of particles detected. The goal of the data processing code was to create detailed datasets with minimal statistical error. For example, if 100 particles of a certain size were detected in one depth bin, error for the concentration of particles of that size would be +/-10%. If 10 larger particles were detected in one depth bin, error for the concentration of particles of that size would be +/- 31.6%, and if only one particle of a given size is detected, error is +/-100%. In my analysis, the goal was to be able to distinguish between particle size distributions at different depths and different stations. To quantitatively state differences between depths and stations, error must be low enough that the values do not overlap. To decrease the amount of error involved in counting statistics, the downcast was selected using descent rate and the data were binned into depth intervals to yield statistically sound particle counts.

Downcast Selection and Descent Rate

I analyzed data collected during the downcast, eliminating any 1-liter images photographed during upward motion or stillness from the dataset. In this way I only analyzed the images of seawater and the particles within it that had not yet been disturbed by the motion of

the CTD rosette. At an average descent rate of 1 m/s, the UVP will capture one 1-liter images every 9 cm in depth. In practice, it was impossible to achieve a perfectly uniform descent rate due to ship motion. Descent rate greater than 0.3 m/s allowed the camera to operate properly (Figure 1.4). Descent rates ranging from 0.4 to 1 m/s were typical speeds for the downcasts on most deployments, with an average of 0.8 m/s.

To account for ship motion, soaking near the surface, and pauses during the cast, I wrote code that calculated the descent rate and eliminated all portions of the dataset in which the camera was stationary or moving upward. Since the camera snapped photographs at a fixed rate, slower descent rates caused overlapping of the 1-liter images which resulted in pseudoreplication. If images overlapped too much, the UVP counted the same particles many times over, saving duplicate vignettes of large objects. Overlapping images increase particle counts but hinder statistical analysis because they create erroneously low error, especially for larger size classes of particles. Therefore, a faster descent rate causing minimal overlap between images is ideal for statistically sound particle counts (Figure 1.4).
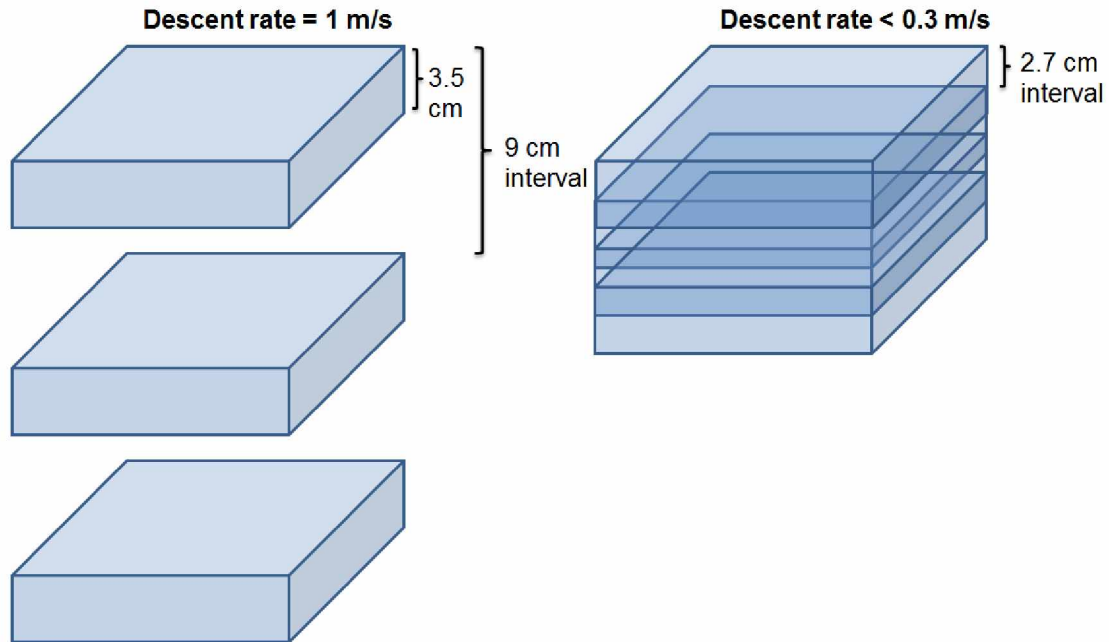
Figure 1.4. Conceptual diagram of the locations of 1-liter images photographed at different descent rates of the UVP. Assuming flat seas without the effects of ship motion due to waves, a sampling frequency of 11 Hz in mixed acquisition mode, at a descent rate of 1 m/s, the UVP photographs consecutive parcels of water at 9 cm intervals without overlap. Overlap (right) occurs at descent rates < 0.3 m/s, because the camera will photograph at < 2.7 cm-intervals, which is less than the depth of the camera's 3.5 cm vertical field of view.

In my analysis, data were removed if the descent rate was negative or less than 0.3 m/s. The variability in the remaining portion of the descent rate was most likely driven by the motion of the ship (Figure 1.5). In the data collected during the slower descent rates (0.4-0.8 m/s) the UVP did create duplicate images of some particles, as seen in the duplicate .jpeg vignettes of some of the objects. However, if the sampling process caused the UVP to overestimate large, rare particles due to image overlap, it therefore also overestimated particles of all size classes in the same proportions. Under this assumption, duplicates did not need to be subtracted from the

total particle count on the principle of scale, as there were few duplicates amid many thousands of images.
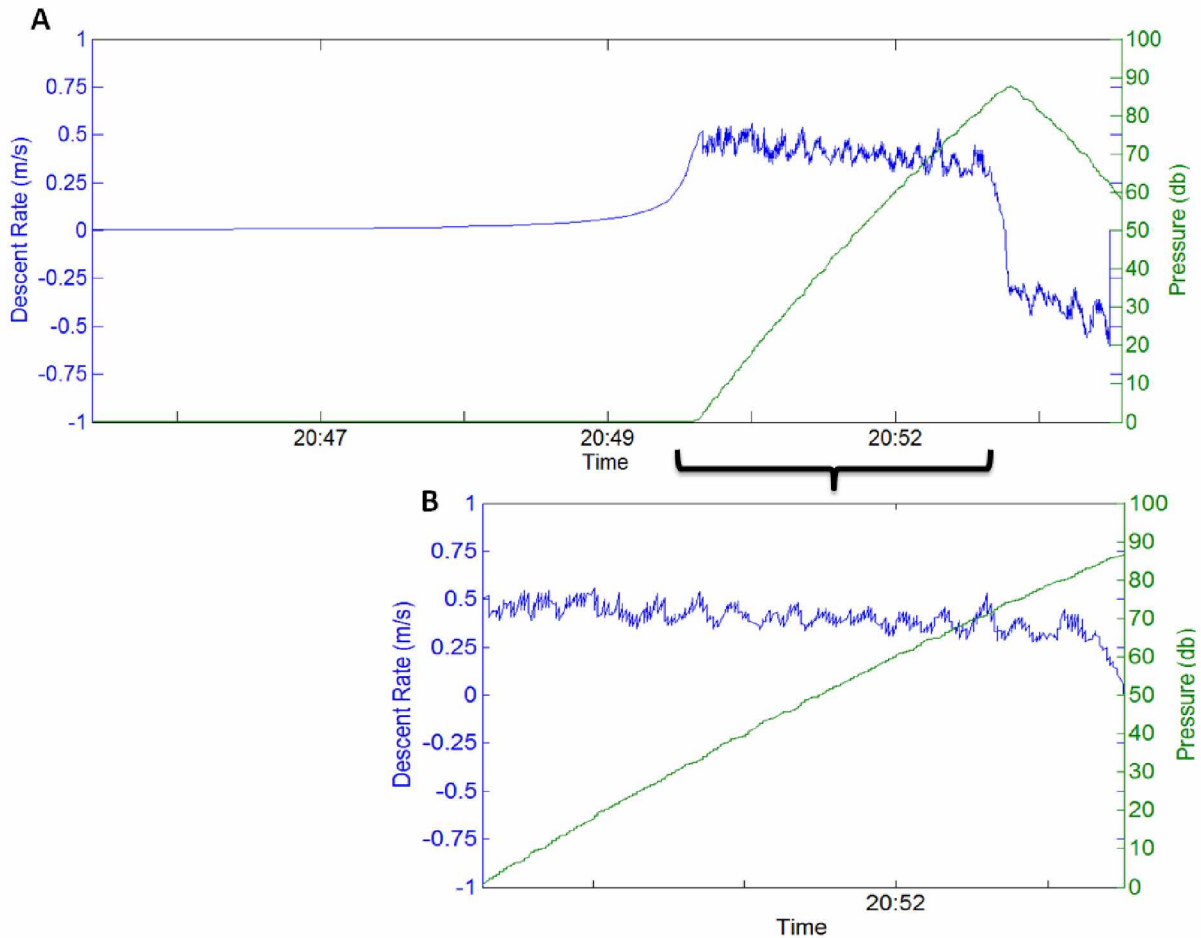
Figure 1.5. Descent rate of the UVP through the water column when operated in I/O mode at station GAK4 on the Seward Line in May 2014. Blue line indicates descent rate (m/s) and green line indicates absolute depth measured by pressure in decibars. A) Full descent rate recorded by the UVP internal pressure sensor, including the deck time before the descent and a small portion of the upcast. Data are eliminated if they fall outside the time frame of B) the downcast, where descent rate is >0.3 m/s. On the downcast, variability in the descent rate is driven by the rocking motion of the ship due to surface waves.

Binning Data by Depth

Depth bins were used to obtain sufficient particle counts, keeping the dataset statistically sound despite changes in the descent rate due to wave action. Depth was binned into increments so that those bins contained approximately the same volume of photographed water. The size of the depth bins was chosen to avoid error in counting statistics while still maintaining a high resolution of data during the downcast. When bin size was too small, statistical noise appeared because of counting error due to insufficient particle counts within each depth bin. For example, using 1-m depth bins resulted in some depth bins with no images while some bins contained more than 20. Thus, the depth bins that accounted for a much larger volume of seawater had larger counts of particles than other depth bins. 5-m depth bins created image counts within each depth bin that were relatively uniform with particle counts great enough to minimize error in the counting statistics (Figure 1.6).
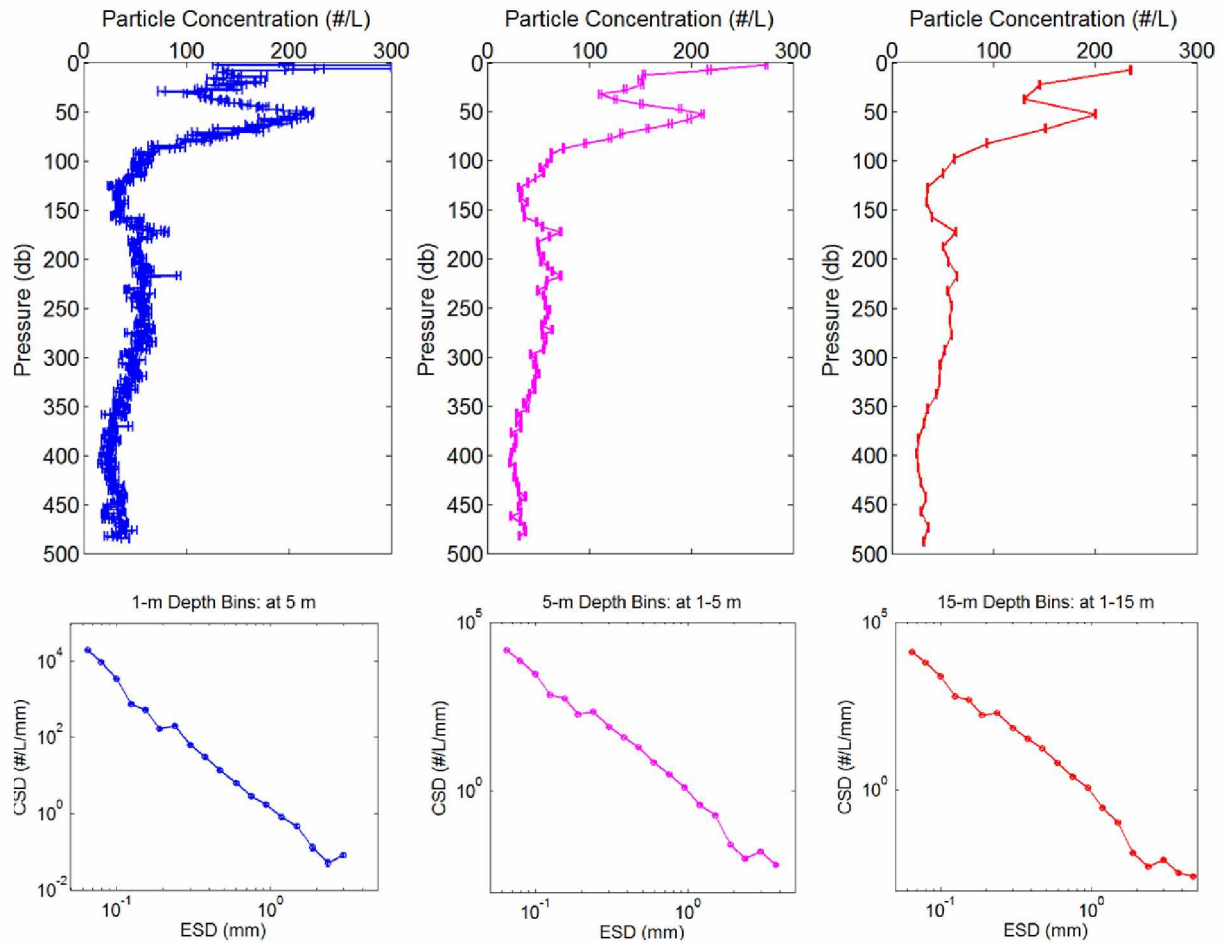
Figure 1.6. Depth profiles of particle concentration (top row) and the resulting surface-depth concentration size distribution (CSD) for particles counted with different depth bin configurations (bottom row). Error bars, although too small to be pictured in bottom row, represent +/- 1 standard error per Poisson counting statistics. Blue figures were calculated from 1-m depth bins, pink from 5-m depth bins, and red from 15-m depth bins. Data were collected at station GAK12 in the offshore portion of the Seward Line in September 2014. Increasing the size of depth bins increases the volume of water photographed in each bin and the subsequent count of particles within each bin, reducing error.

Calculating Size Distributions

Arguably, the most important feature of the UVP is its ability to detect and measure a

wide range of size classes in detail, because particle size as a property is integral to

understanding the functioning of an ecosystem and its carbon export to depth (Fowler and

Knauer, 1986; Guidi et al., 2008b; Parsons, 1969). The UVP is the only instrument with

resolution fine enough to capture the dimensions of small particles (0.06-0.1 mm) while still sampling a large enough volume of water to capture larger objects (>1 mm) (Stemmann et al., 2008). Particle size distributions provide a preliminary idea of the planktonic communities present in a marine system. As such, the UVP size distribution data can be used to obtain an idea of the export potential of a given ecosystem, and the detailed size spectra measurements provide a way to estimate carbon flux to depth.

Small particles (<100 μm) are almost always exponentially more abundant than large particles in the water column (Figure 1.7). Very large particles (>1 mm) sink more rapidly than small particles, but are so rare that their contribution to flux becomes more diminished. Taking into consideration both abundance and size, marine particles in the middle size range (0.2-0.8 mm), which are both relatively abundant and relatively large, contribute the most to mass flux of material from the surface to depth (Ebersbach and Trull, 2008; McDonnell and Buesseler, 2012).

Beyond their sinking rates, differences in particle size spectra can mean drastically different particle behavior and composition, such as the ratio of POC/^{234}Th of particles, which varies between regions, likely due to differences in biological interactions (Burd et al., 2007). Important particle properties like sinking rate and carbon content depend on the accurate measurement of particle size (Burd and Jackson, 2002; Guidi et al., 2008b). These properties are fundamental to many related biogeochemical studies, such as the measurement of macro- and micro-nutrient compositions of particulate matter. For example, in one study in the California Current system, carbon: nitrogen ratios of particles increased with particle size (Alldredge, 1998). The ability of the UVP to process the 1-liter images to yield particle counts as well as individual particle metrics such as size, shape, and greyscale stands this instrument apart from many other optical imaging techniques.

Size bins were logarithmically spaced from the smallest size classes recognized by the UVP to the largest (Figure 1.7). Due to the resolution in pixels and the focus created by the field of view of the camera lens, this instrument can measure the 2-dimensional areas of particles down to 0.06 mm in diameter. However, the large volume of water within each image enables the UVP to detect and image large objects (0.5 mm to 2.7 cm) as well. This range is optimal for studying a large quantity of particulate matter because observations of algal and detrital particles revealed that the greatest mass of those objects in the ocean is found in aggregates 100 μm to several mm in size (Stemmann et al., 2008). From the lower threshold of 60 μm to the upper threshold of 2.7 cm, size bins were logarithmically spaced to account for the fact that there are exponentially more small particles than large particles in any given water parcel. When sorting particles into these size distributions, the counts for each size class were normalized to the width of each size bin, represented by the mm denominator of the unit #/L/mm (Figure 1.7).

An artifact produced when the camera's flash illuminates the particles results in small objects being perceived as larger particles due to a glow created by the flash that distorts the edges of the objects. This glow has a non-linear relationship to the size of the particle, as small objects scatter proportionally more light than large particles do. Before calculating equivalent spherical diameter (ESD), this "glow" was removed when converting the objects' area in the 2-D photograph from pixels to mm^2 with the following power function:

$$A_m = 0.0032 * A_p^{1.36}$$

where A_p is the area of the photographed particle in pixels and A_m the area in mm^2.

Constants 0.0032 and 1.36 in the power function were determined in a testing tank for this particular UVP instrument. The manufacturer calculated the magnitude of the difference

between the known area of objects placed in the tank and the area measured by the UVP. For each separate UVP instrument, they used the function *fminsearch* (Mathworks, Inc.) and a jackknife error estimation on the differences between known area and UVP area to determine the constants that became the multiplier and exponent in the power function above (Picheral et al., 2010).

Once the glow was removed, ESD was calculated based on the area in mm^2 of the 2-dimensional shapes captured in the image:

$$ESD = 2\sqrt{Am/\pi}$$

Included in the assumption that each particle is a sphere was the notion that the camera captures each particle as a 2-dimensional circle within the larger image. This was a simplification, as the UVP can capture the 2-dimensional projections of large objects as they appear on the downcast, which are not perfectly circular and can take any shape, although it is impossible to determine the shape of objects >5 pixels in area. Each particle's 2-dimensional area in pixels was converted to mm^2 based on the pixel resolution of the camera (0.148 mm=1 pixel), from which diameter was calculated based on the area of the assumed circles.
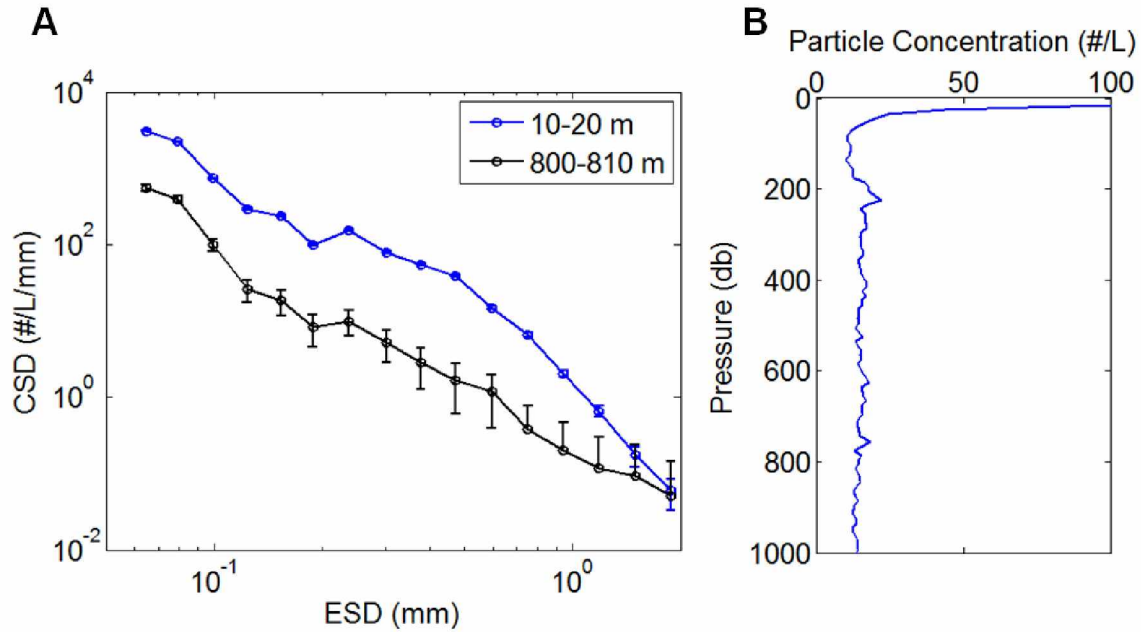
Figure 1.7. A) Concentration size distribution (CSD) of particles from station 194 at 148°W on the P16N Cross-Gyre Line collected in June 2015. Blue line represents surface size distributions (10-20 m) and black line represents size distributions in intermediate waters (800-810 m). Error bars represent +/- one standard error per Poisson distribution counting statistics. As equivalent spherical diameter (ESD) increases, particle counts decrease, which in turn increases the proportional amount of error. While concentration of particles at the two depths pictured are significantly different for small particles < 1 mm, concentrations of the largest size classes >1 mm are not significantly different. B) Depth profile to 1000 m of total particle concentration (#/L) for reference.

An alternative to the number concentration is a volume concentration. In addition to calculating the number of each size class of particles in each liter of seawater, I also calculated the volume of each size class of particles per liter (Figure 1.8). Although this did not bypass the spherical shape assumption, it did compare like units, i.e., a conserved volume of particles per a unit volume of seawater. Models of theoretical particle dynamics also prefer to couch results in terms of conserved particle volume (Burd, 2013; Guidi et al., 2008a). However, in this study, a count concentration was preferred over a volume concentration because of the behavior of the camera, which analyzed water parcels by counting. In previous studies using the UVP

instrument, results were most often reported in terms of count concentrations (Boss et al., 2015; Guidi et al., 2012; Picheral et al., 2010).
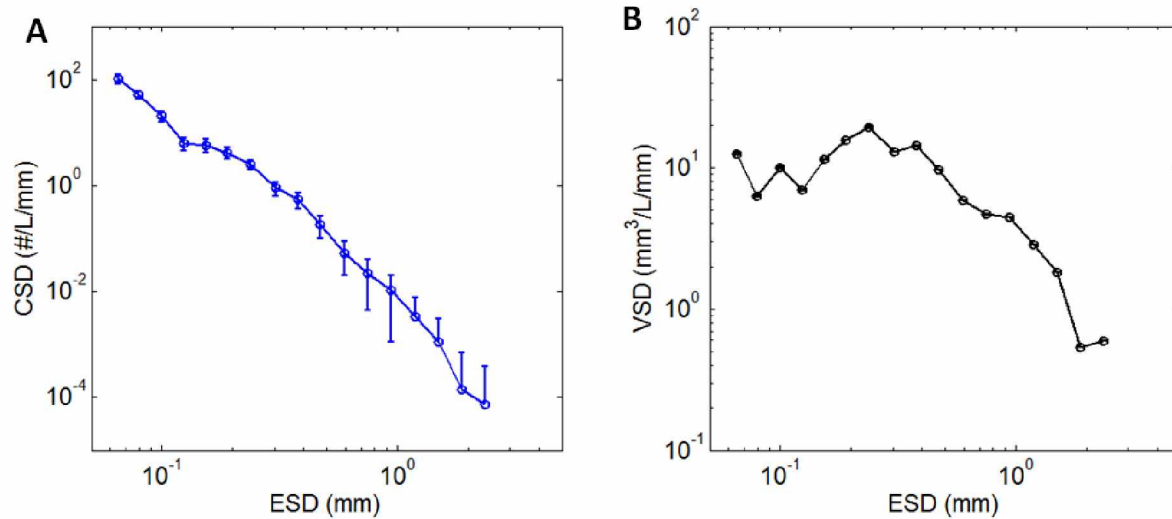
Figure 1.8. Comparing A) concentration size distribution (CSD) and B) volume size distribution (VSD) at surface depths 1-5 m at station GAK 6 on the Seward Line in May 2014. Exponentially more small particles 100-290 µm were present in the water column, yet size classes in the slightly larger 170-480 µm range made up more of the total particle volume. Error bars indicate +/- one standard error per Poisson distribution counting statistics, visible only in the CSD.

Large Object Vignettes and Image Sorting

In addition to concentrations and size distributions, it is of interest to determine the density of particles present in the water column because density affects sinking rates. Density, porosity, drag coefficient, and shape vary so widely between different types of particles of any one size class that diameter alone is not enough to thoroughly compare sinking rates and subsequent carbon flux to depth (Burd, 2013). For example, a large aggregate of siliceous diatoms may have the same diameter as a fragile clump of transparent detritus. While the former is a dense, quickly sinking aggregate, the latter is a low-density, more slowly-sinking or suspended particle of marine snow. The UVP enabled me to solve this problem, by providing

separated images of all particles above a user-defined diameter. I sorted these images using

Plankton Identifier (PID) software in three steps: learning, prediction, and validation. Images

were built into a learning set, which the computer used to predict the types of all large objects

(>500um) photographed at a station or cruise, after which I validated the computer-sorted images

(Gorsky et al., 2010).

First, learning sets were constructed by manually selecting vignette images from all

downcasts within a cruise as examples for each category. Categories were created depending on

what types of particles were present on any given cruise, typically single words or abbreviations

such as "aggregate," calanoid," and "house" (Figure 1.9). The prediction algorithms used by the

Plankton Identifier (PID) software generated the best results from a learning set when it

contained 10 to 15 categories. Also, best results were generated from a large learning set that

captured the variability within each category by using objects from all casts within a cruise. An

ideal learning set contained up to 300 images in each category, including both clear, identifiable

images as well as the more blurry, grey images that were more difficult to identify. Computer

prediction generated the best results when a separate learning set was built for each cruise, to

account for geographic, seasonal, and interannual variability (C. Hopcroft, personal comm.).

Second, based on the created learning set, the computer predicted which images belonged

in which categories based on a Random Forest algorithm programmed into the PID software

(Breiman, 2001). The computer used 66 variables to predict in which category a given object

belonged, such as grey scale, ESD, exterior perimeter, and elongation. Each attempt at

prediction generated a distribution and a confusion matrix for each station. The distribution

listed percentages of total images in each category, and the confusion matrix created a table to

describe the performance of the classification model on the selected data.

Third, the computer-sorted images were validated by a human. Although this was the most time consuming step of the process, it did significantly improve my ability to correctly identify the vignettes. User validation has been proven to significantly reduce error in other zooplankton image analysis methods, such as Zooscan scanning software used to analyze preserved net-tow samples and the Scripps Plankton Camera mounted on a pier to sample autonomously (Gorsky et al., 2010; Roberts et al., 2014).
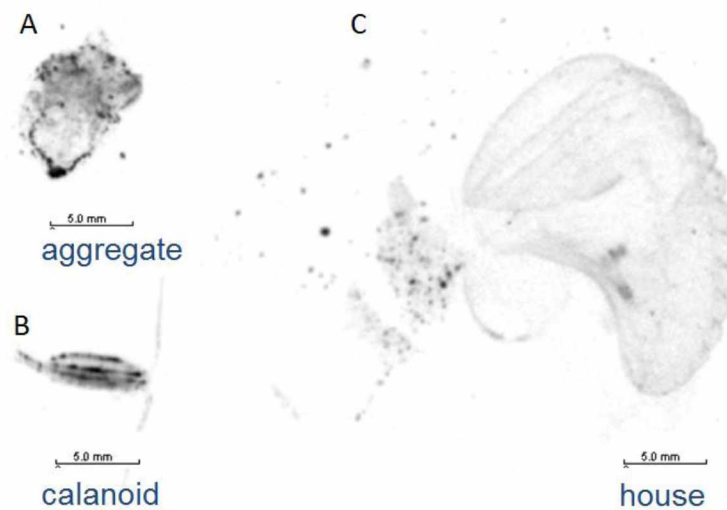
Figure 1.9. Three examples of vignettes sorted into different particle type categories using Zooprocess software. Simple terms were used for categories such as A) "aggregate" represented here as a large marine snow particle collected in the Gulf of Alaska, B) a large "calanoid" copepod collected in the Beaufort Sea, and C) a "house" built by an appendicularian collected in the New York/New Jersey Bight.

Methods Used Alongside the UVP

Several methods were used alongside the UVP in preliminary trials of the instrument. Although the goal was not to quantitatively assess validity or reliability of the camera, these datasets can help to qualitatively understand the manner in which this innovative camera system

goes beyond traditional CTD-mounted optics. The following methods were used to measure *in situ* chlorophyll *a*, size-fractionated chlorophyll *a* from filtrations, and *in situ* beam attenuation.

Chlorophyll *a* was measured *in situ* using a WET Labs ECO-AFL/FL fluorometer mounted on the 16-bottle CTD rosette. Data were viewed in real time using the SeaBird CTD sensor and related software package. Size-fractionated chlorophyll *a* was measured by filtering known volumes of seawater collected in Niskin bottles from a series of 6 surface depths, usually surface to 50 m in 10 m increments. Water was transferred from the Niskin bottles in six 250-ml bottles, which were poured through a tiered filtration system with vacuum suction. The first tier held 20 μm Whatman filters, and the second held 0.7 μm glass microfiber filters (GF/F). Chlorophyll *a* was extracted from filters in diluted HCl for 24 h and then measured using a Turner Designs fluorometer (Holm-Hansen et al., 1965; Parsons et al., 1984).

Beam attenuation was measured *in situ* using a WETLabs C-Star Transmissometer mounted on the CTD rosette. This transmissometer measured the ratio of the amount of light received across the pathlength *in situ* compared to the amount of light received in clear water calibrated in the factory. It propagated a red beam of light (650 nm wavelength) across a 25 cm pathlength to establish how much light was attenuated by scattering and absorption.

Data analysis

After the initial processing using Zooprocess software, MATLAB was used to conduct all other data processing, including cross-sectional transect figures and statistical analyses. Before comparing the other methods used to the UVP, beam attenuation data and all chlorophyll *a* fluorescence data were binned into 5-m depth bins to match UVP data. Datasets were compared using ordinary least squares linear regressions. The null hypothesis was rejected if the

significance level (α value) was less than 0.05 (5%). The coefficient of determination (R^2) measured the strength of the fit between the linear regression and the data being compared.

Results

UVP Particle Data alongside Fluorometry and Transmissometry

Initial data collected in the GOA were compared to other data obtained by traditional methods from the Seward Line long-term monitoring project in May 2014, including chlorophyll *a* fluorescence and transmissometer beam attenuation. Interestingly, total particle concentration from the UVP did not resemble the patterns seen in *in situ* chlorophyll *a* or beam attenuation along the same transect of seawater. While particle concentration was greatest nearshore and decreased with distance offshore, both chlorophyll *a* and beam attenuation were greatest in surface patches over the mid-shelf and very low in concentration along the rest of the transect. Neither chlorophyll *a* nor beam attenuation showed a significant relationship with UVP-derived particle concentration in the upper water column (0-85 m) (Figure 1.10).

Size-fractionated chlorophyll *a* revealed more about the similarities and differences between the data collected by the UVP and the *in situ* fluorometer. The patterns in the small cell sizes (0.7-20 μm) more closely resemble those of the *in situ* fluorometer, with the greatest fluorescence appearing at 0-20 m depths at GAK stations 7 and 8 (Figure 1.10). However, the large cell size (>20 μm) appeared more similar to the total particle concentrations seen by the UVP, with the highest values nearshore and a slight increase mid-shelf (Figure 1.10). Although there were no significant relationships between any of the four variables, the coefficients of determination were slightly greater for the relationships between large cells and UVP particle concentration (R^2 =0.135) and between small cells and CTD-mounted *in situ* fluorescence (R^2 =

36

0.162) compared with the other two relationships (both R^2 <0.025; Figure 1.11). These results

support the idea that the UVP is more efficient at detecting larger objects than those detected by

CTD-mounted fluorometry and transmissometry.
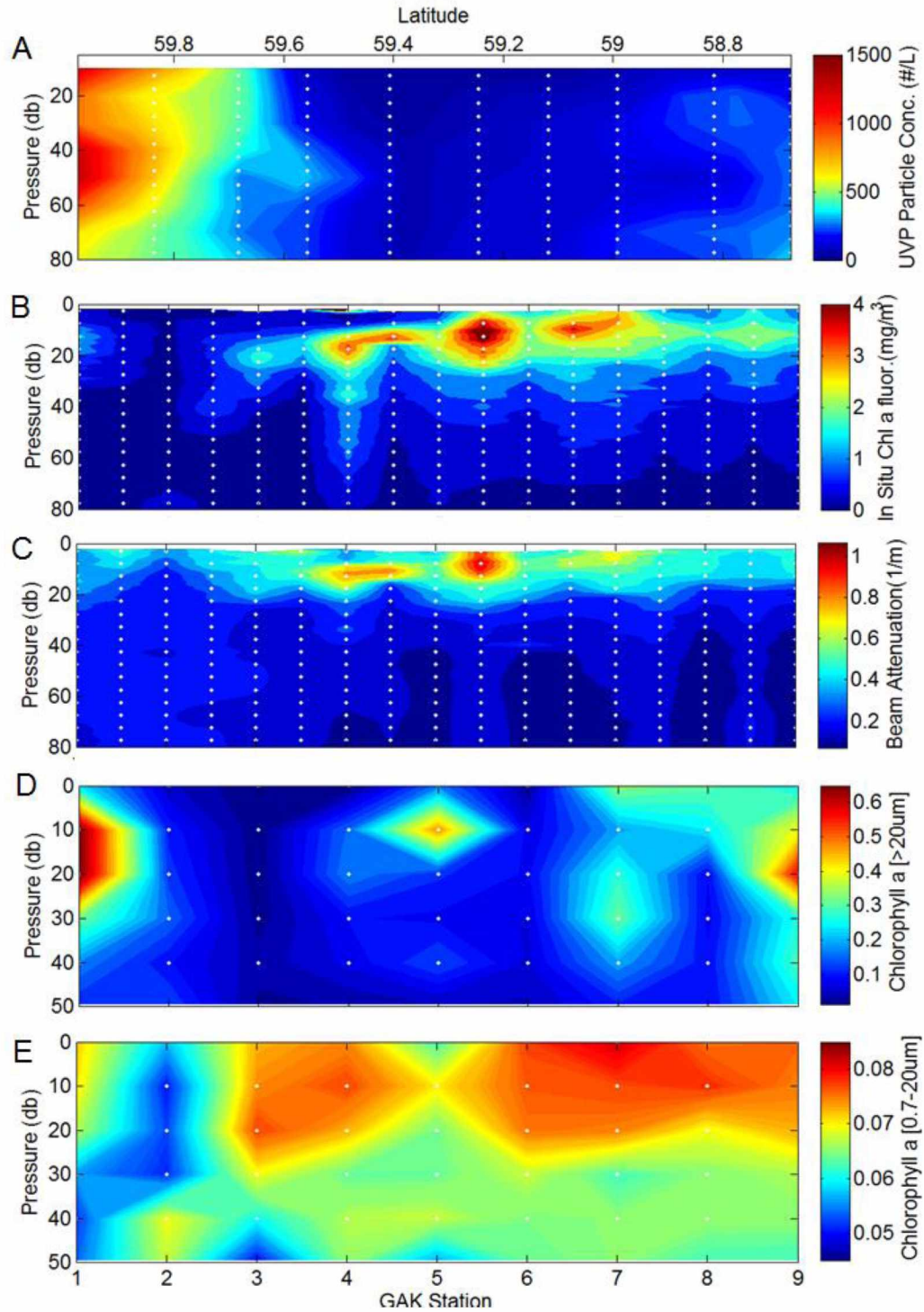
Figure 1.10. Cross-shelf transects from May 2014 comparing A) UVP total particle concentrations to B) *in situ* chlorophyll *a* from the rosette-mounted sensor, C) transmissometer beam attenuation, D) chlorophyll *a* fluorescence extracted from cell sizes >20 μm, and E) chlorophyll *a* fluorescence extracted from cell sizes >0.7 μm and <20 μm. Note: filtrations for size-fractionated chlorophyll *a* were only performed for depths within the photic zone (to 50 m).
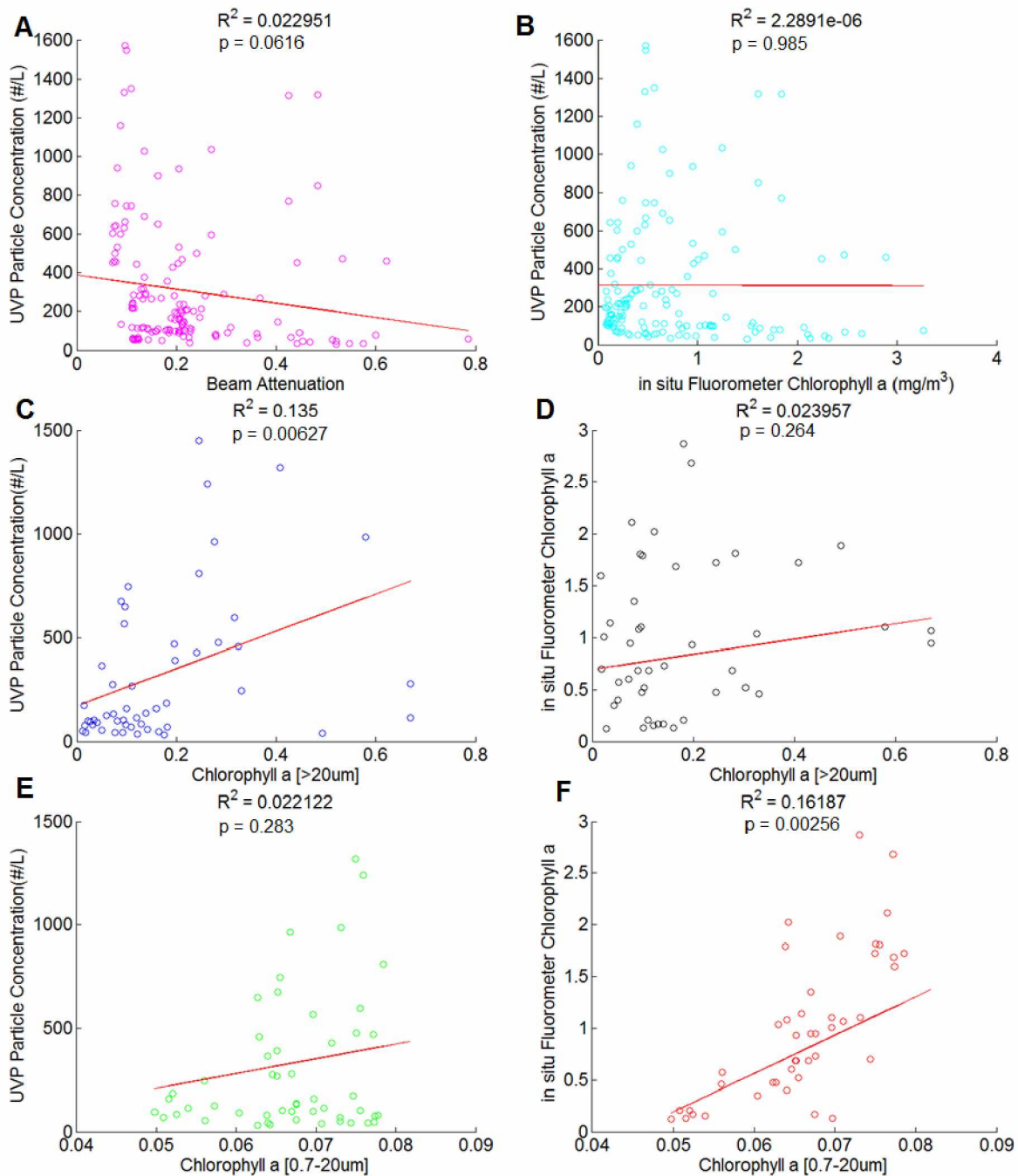
Figure 1.11. Relationships between UVP total particle concentration and other variables, via ordinary least squares regressions. A) UVP and transmissometer beam attenuation, B) UVP and *in situ* chlorophyll *a* fluorescence (mg/m^3), C) UVP and large cell chlorophyll *a* fluorescence (>20μm), D) *in situ* and large cell chlorophyll *a* fluorescence, E) UVP and small cell fluorescence (0.7-20μm), and F) *in situ* and small cell fluorescence. All data are from the May 2014 Seward Line cruise. Weak but significant relationships were found between large cell fluorescence and UVP particle concentration (C; p=0.00627) and between small cells and *in situ* fluorometry (F; p=0.00256). No other significant relationships were found (p>0.05).

39

Large-Object Vignettes

Sorting the vignettes from May 2014 showed that the majority of very large particles (>500 μm) were particles as opposed to identifiable large zooplankton individuals (Figure 1.12). 10.4% of vignettes showed identifiable zooplankton organisms (Figure 1.13), while 89.6% of vignettes depicted nonliving particles (Figure 1.14). Particles <500 μm in ESD that were not processed as separate vignettes included both living plankton organisms and nonliving particles, but at these smaller sizes taxa cannot be identified (Stemmann and Boss, 2012). It is possible that some of the vignettes at the smaller end of the image-generating spectrum (500 μm - 1 mm), such as those in the "small_dot" category, are living zooplankton organisms that cannot be accurately identified (Figure 1.15). Predicted distributions were calculated based on a small learning set created from all of the large-object vignettes imaged on the May 2014 Seward Line cruise. The confusion matrix generated by the learning set, which describes the performance of the classification model used to identify the images, showed very few confusions. This small number of confusions is possibly due to a small number of objects (<100) sorted into each of the learning set categories.

Confusion matrix														
	blur_lightgrey	calanoid	clumpy_chains	dark_head	dark_lumpy	elongated_fecal	fiber	fritillaria	house	large_fluffy	medusa	small_dot	tangled_oval	Sum
blur_lightgrey	39	0	0	0	0	0	0	0	0	0	0	0	0	39
calanoid	0	84	0	0	0	0	0	0	0	0	0	0	0	84
clumpy_chains	0	0	47	0	0	0	0	0	0	0	0	0	0	47
dark_head	0	0	0	70	0	0	0	0	0	0	0	0	0	70
dark_lumpy	0	0	0	0	60	0	0	0	0	0	0	0	0	60
elongated_fecal	0	0	0	0	0	79	0	0	0	0	0	0	0	79
fiber	0	0	0	0	0	0	13	0	0	0	0	0	0	13
fritillaria	0	0	0	0	0	0	0	66	0	0	0	0	0	66
house	0	0	0	0	0	0	0	0	13	0	0	0	0	13
large_fluffy	0	0	0	0	0	0	0	0	0	72	0	0	0	72
medusa	0	0	0	0	0	0	0	0	0	0	8	0	0	8
small_dot	0	0	0	0	0	0	0	0	0	0	0	69	0	69
tangled_oval	0	0	0	0	0	0	0	0	0	0	0	0	26	26
Sum	39	84	47	70	60	79	13	66	13	72	8	69	26	646

Distribution			
Values	Count	Percent	Histogram
blur_lightgrey	28	4.64 %	
clumpy_chains	21	3.48 %	
dark_lumpy	4	0.66 %	
elongated_fecal	170	28.15 %	
fiber	9	1.49 %	
large_fluffy	3	0.50 %	
small_dot	140	23.18 %	
tangled_oval	10	1.66 %	
dark_head	144	23.84 %	
Total particles:	**529**	**89.6%**	

Distribution			
Values	Count	Percent	Histogram
calanoid	57	9.44 %	
fritillaria	17	2.81 %	
house	0	0.00 %	
medusa	1	0.17 %	
Total zooplankton	**74**	**10.4%**	

Figure 1.12. Example of a confusion matrix and category distributions generated by the Plankton Identifier prediction software based on a preliminary learning set for the Seward Line spring cruise 2014. The bagging process for the category distributions was based on a Random Forest algorithm for machine learning. The learning set for the prediction was built using vignettes from all stations on this cruise. Distributions show results from only station GAK 5 over the middle shelf.

41

	Zooplankton Group (Coyle & Pinchuk 2005, Hopcroft et al. 2010)	UVP vignette sorting category
A	*Neocalanus spp.* *Metridia spp.* *Eucalanus spp.* *Calanus spp.*	copepod
B	Sipohonophora	large_rare
C	Salpida	large_rare
D	Ctenophora	large_rare
E	Cnidaria	medusa
F	Euphausiid	crustacean_other
G	*Limacina helinica*	pteropod
H	Chaetognatha	chaetognath
I	Appendicularia	house
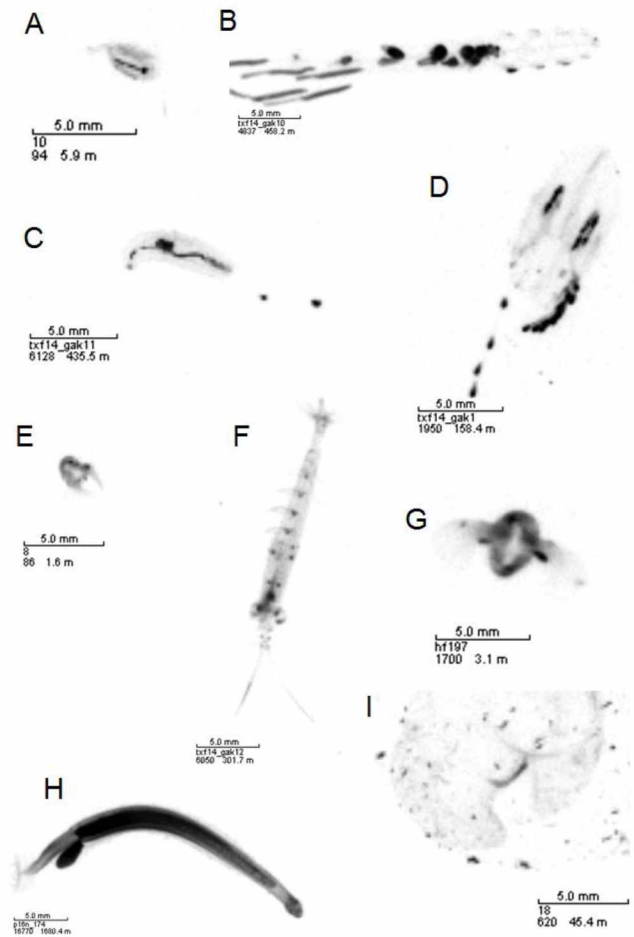
Figure 1.13. A qualitative comparison of zooplankton groups commonly found in the coastal Gulf of Alaska to preliminary categories for sorting UVP-generated images from the Seward Line stations in May 2014, September 2014, and July 2015. Zooplankton groups are examples of common, abundant species and groups collected in Bongo net and Multi-net plankton tows in the Gulf of Alaska over the past 15 years, based on data from the Seward Line LTOP (Coyle and Pinchuk, 2005, 2003; Hopcroft et al., 2010).
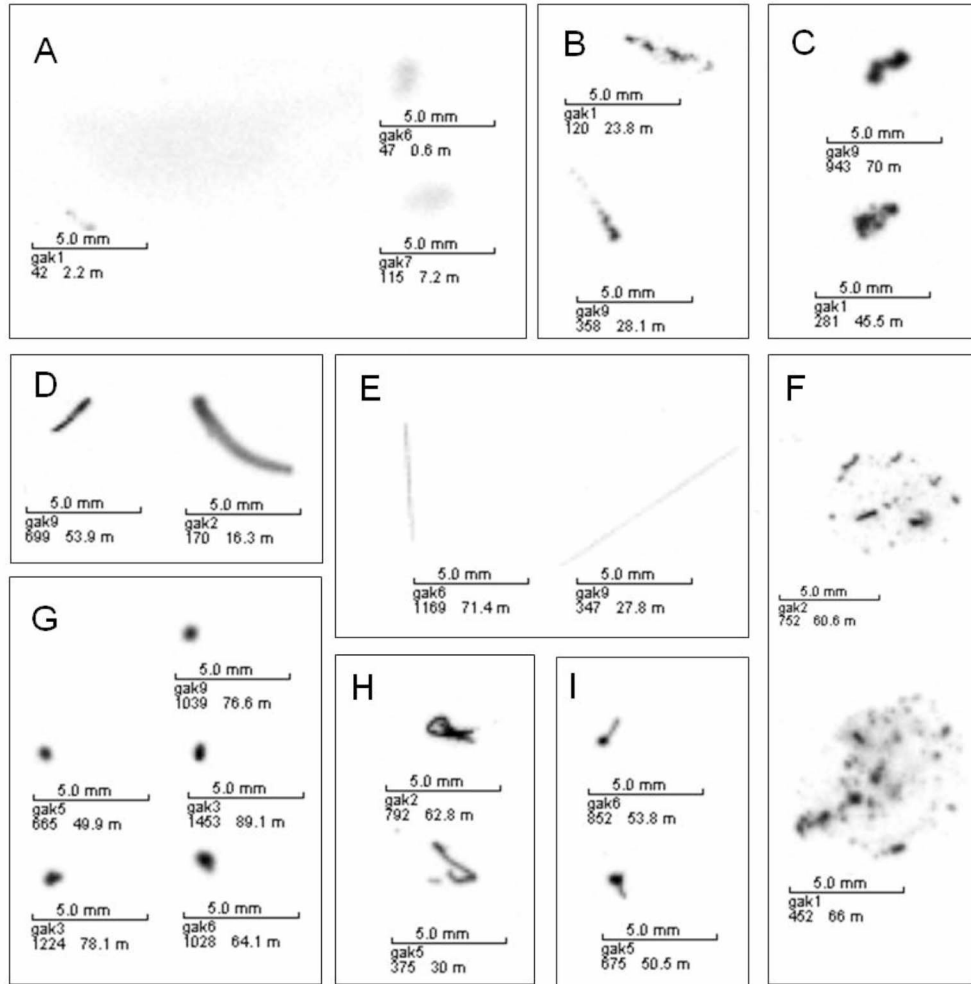
Figure 1.14. Example of the vignette images not identifiable as zooplankton organisms placed in categories for sorting, from the Seward Line in May 2014. A) blur_lightgrey, B) clumpy_chains, C) dark_lumpy, D) elongated_fecal, E) fiber, F) large_fluffy, G) small_dot, H) tangled_oval, and I) dark_head.

Discussion

During preliminary trials on the Seward Line cruises, the UVP has clearly demonstrated its many advantages over traditional particle collection methods. These first trials illustrate the UVP's size class analysis capabilities and photographic application. The UVP excels at detecting a wide range of particle sizes while also capturing images of fragile zooplankton and elusive marine snow particles.

Optics

The absence of a relationship to chlorophyll *a* confirmed that the particles detected by the UVP differ from those that are detected by the other optical methods, which makes sense based on the optical designs of each instrument. Each of these different tools samples different subsets of the full range of particle sizes in the water column. *In situ* fluorometry targets living phytoplankton cells whose pigments actively fluoresce. These fluorescing phytoplankton cells of many taxa, such as cyanobacteria, dinoflagellates, and diatoms, range in mean cell size from 1 μm to 65 μm in cell diameter (Alpine and Cloern, 1985; Proctor and Roesler, 2010), reaching sizes to 200 μm with a large range of error (Sieburth and Lenz, 1978). Of this range of sizes, the UVP detects only the very largest cell sizes and aggregates of cells. However, it goes beyond the capabilities of fluorometry in creating large-object vignette images of multi-cellular phytoplankton colonies, aggregates, and chains, such as *Volvox spp.* and *Trichodesmium spp.* (Figure 1.15).
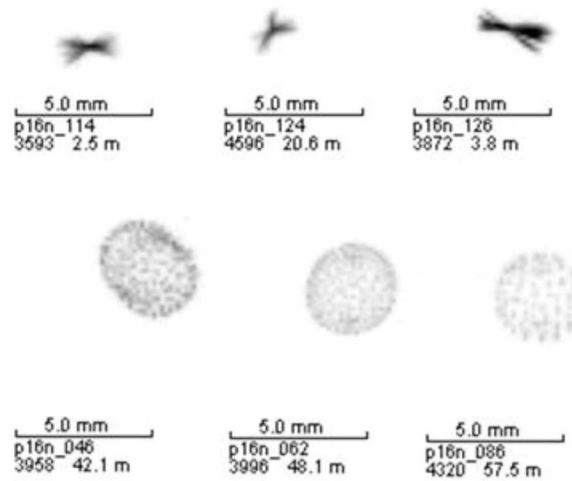
Figure 1.15. Vignette images of colonial and chain forming phytoplankton *Trichodesmium spp.* (top row) and *Volvox spp.* (bottom row), photographed on the P16N cruise in the North Pacific. *Trichodesmium* clumps pictured here were found between 23-30° N latitudes, while *Volvox* colonies were found between 0-8° N latitudes.

Patterns seen by the transmissometer in May 2014 did not resemble the UVP particle concentrations any more closely than the *in situ* fluorometer, likely due to the difference in the optical designs of the instruments. The transmissometer used on the Seward Line has an optical acceptance angle of 1.2°, making it more suitable for measuring the optical scattering caused by very small objects less than 10 μm in diameter. Transmissometers with this acceptance angle measure less than half of the total scattering caused by particles larger than 10 μm (Boss et al., 2009). Since this transmissometer detects very small objects, it is unsurprising that patterns in beam attenuation did not resemble patterns of total particle concentration measured by the UVP.

Other *in situ* optical devices that are non-Seabird-compatible are often used to detect particulate organic matter, but most instruments detect smaller size ranges. For instance, the Laser *In situ* Scattering and Transmissometer (LISST) estimates the size of particles 2.5-500 μm based on how intensely they scatter light from a laser beam as they pass through a small opening

45

(5 cm pathlength) in the instrument. Moreover, its small sampling volume decreases the accuracy of measurements for particles greater than 100 μm in diameter (Boss et al., 2015; Karp-Boss et al., 2007). Another example, the Laser Optical Plankton Counter (LOPC), analyzes the shapes and opacity of objects crossing an array of lasers and detectors, but the resolution of the sensor is not precise enough to see objects smaller than 500 μm (Herman, 2004).

Other digital cameras even more similar to the UVP are used to sample larger particles and zooplankton, but they are limited by factors such as low volume of seawater analyzed, low temporal or vertical resolution, or having stationary locations (Boss et al., 2015). For example, the Video Plankton Recorder (VPR) samples the water column not unlike the UVP, except that it only photographs 1/100 as great a volume. A smaller sampling volume decreases total particle counts, raising counting uncertainty via Poisson distribution counting statistics. The *In situ* Icthyoplankton Imaging System (ISIIS), Zooplankton Visualization System (ZOOVIS), and Shadowed Image Particle Profiler (SIPPER) were designed to photograph fish, zooplankton, and large particles, respectively. However, all three camera systems create a large number of out-of-focus images that are time-consuming to process, and all three require more specialized interfacing such as their own cables for descent in addition to the CTD cable (Boss et al., 2015; Picheral et al., 2010). In contrast, the UVP overcomes these limitations by sampling large volumes of water while still maintaining high resolution.

Image Analysis

Several advantages and limitations were identified when sorting the vignette images. For one, sorting the vignettes is an excellent semi-quantitative check of the plankton communities and particle types present at a given station or region. Knowing the proportion of marine snow

as compared to zooplankton as well as the types of zooplankton present greatly aids our understanding of the ecosystem structure and biogeochemical functioning of the system. Quantitative zooplankton analysis is limited due to human error in selecting image analysis categories, low taxonomic resolution and possible avoidance mechanisms. However, this camera is extraordinary in its abilities to capture fragile gelatinous zooplankton and marine snow particles.

One limitation is that sorting the .jpeg vignettes can only be done at very low taxonomic resolution. For instance, it was possible to sort very large calanoid copepods from small calanoid copepods, but was nearly impossible to be species-specific within those two groups. Another possibility exists that the larger, more mobile zooplankton organisms such as euphausiids have avoidance mechanisms, causing them to flee from the lights of the camera as it descends.

During sorting, image category prediction can be easily swayed by the size of the categories in the learning set and the selection of the categories. For example, adding far more example vignettes in the "snow" categories in the dataset for the P16N cruise yielded results that might actually over-represent marine snow with respect to zooplankton. There are often so few vignettes of certain zooplankton groups, such as pteropods and chaetognaths, that error remains high and does not lend itself to quantitative statistical analysis of those groups.

Vignette-sorting results from May 2014 could be skewed by the selection of categories, which only covered three of the zooplankton groups commonly collected with net tows on the semi-annual Seward Line cruise. Calanoid copepods usually dominate zooplankton abundances on the Seward Line cruise in the GOA (Coyle and Pinchuk, 2005, 2003; Hopcroft et al., 2010),

so it is unsurprising that they also dominated the identifiable zooplankton vignettes generated by the UVP.

A significant advantage of the UVP over net tows is that this camera can capture images of zooplankton that would be destroyed by traditional sampling methods. If the research goal is to quantify living organisms, a combination of methods would be an ideal strategy to capture more accurate abundances of all zooplankton groups. Zooplankton net tows have been used on the Seward Line long-term monitoring project for nearly 20 years (Coyle and Pinchuk, 2003). This method is reliable and provides a long time-series, yet it favors the collection of crustaceans and other hard-shelled organisms, often destroying gelatinous organisms during the sampling process (Raskoff et al., 2005). In contrast, the UVP is a non-destructive sampling method, allowing the objects within the photographed water parcels to remain whole and almost undisturbed as it descends. Unlike a net, the UVP can measure small gelatinous organisms without destroying them (Figure 1.16).

5.0 mm
p16n_167
13975 1154.6 m

5.0 mm
p16n_149
19243 1896.5 m

5.0 mm
gak13
4702 467.7 m

5.0 mm
8
8654 608 m

5.0 mm
gak4
2812 136.3 m

5.0 mm
p16n_139
9648 659.6 m

5.0 mm
ci4
2318 135.7 m
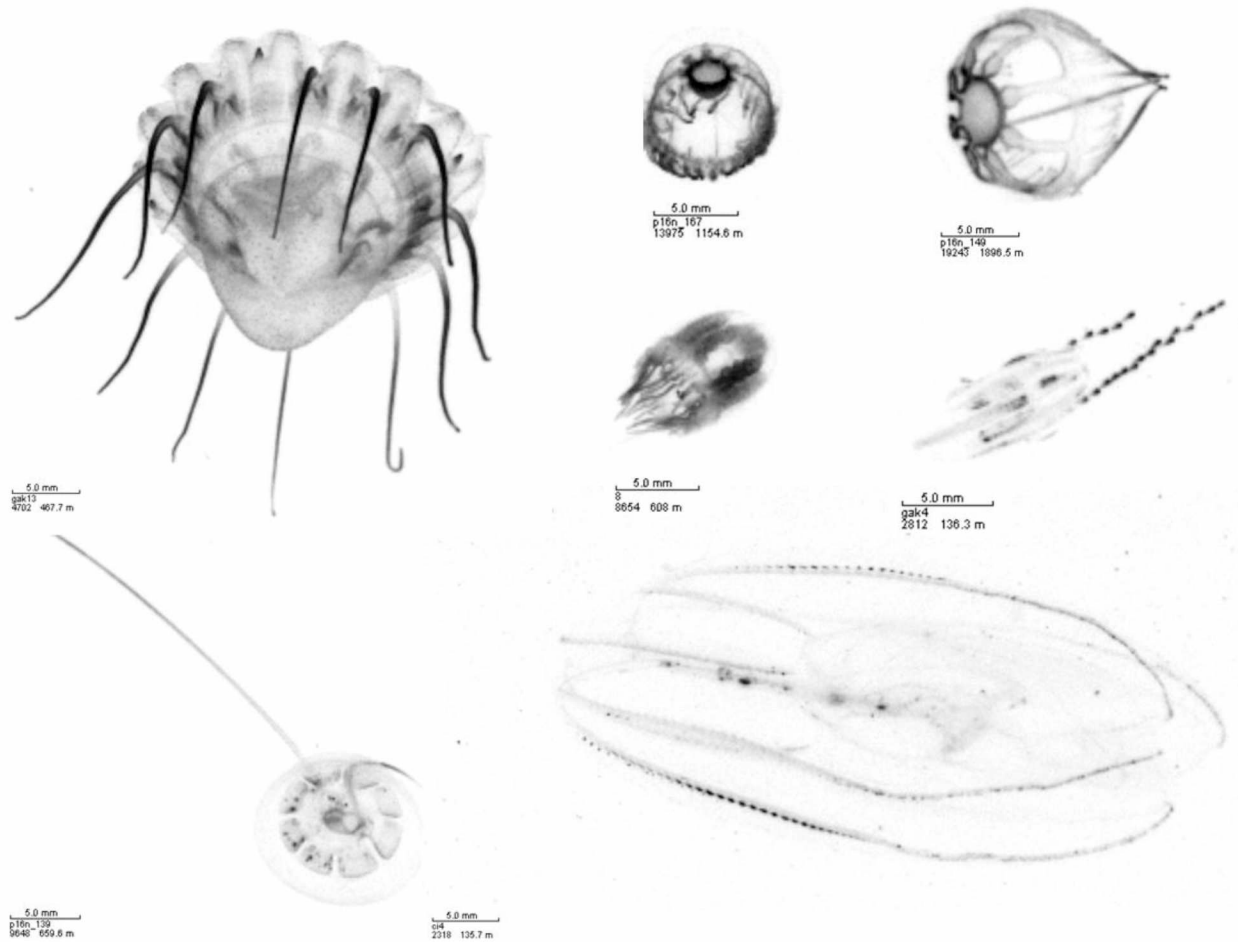
Figure 1.16. UVP vignettes of gelatinous zooplankton groups, which are often underrepresented or destroyed by zooplankton net tows. Images were captured in the New York / New Jersey Bight 2014, the Pacific Ocean on the P16N line 2015, and the coastal Gulf of Alaska 2015.

Furthermore, the UVP excels at sampling marine snow particles and large aggregates of detritus. These suspended or partially-suspended particles can be fragile due to their mucus-like structures, which are glued together with transparent exopolymeric substances (TEP) (Turner, 2002; Verdugo et al., 2004). Often called the "dust bunnies of the sea," marine snow particles are notoriously hard to capture, due to their slow sinking rates, fragile structure, and tendency to stick to the insides of Niskin bottles (McDonnell et al., 2015). Suspended marine snow particles are underrepresented in sediment traps because their slow sinking rates inhibit them from falling

into the traps during short (12-24 hours) deployments in representative numbers. *In situ* pumps are a more comparable method to the UVP than sediment traps, as traps collect only sinking matter while pumps can also collect suspended matter. These pumps collect large volumes of water on filters and are often used to collect particles used in trace metal studies. Pump data, unlike UVP data, are able to provide information on the elemental content of particles. Although size fractionation is an option with the pump method, fast filtration speeds (>1cm/s) can cause some of the large particles to be lost and the more fragile marine snow particles to be fragmented (McDonnell et al., 2015). As a non-destructive *in situ* camera, the UVP can photograph these large objects in their naturally occurring shapes (Figure 1.17).
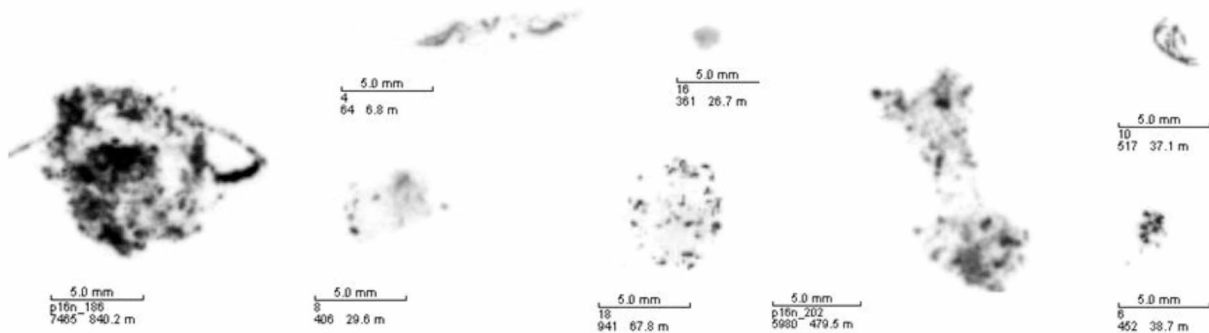
Figure 1.17. Marine snow particles photographed by the UVP in the Gulf of Alaska in May 2014 and June 2015. This type of particle is the most abundant type of particle in vignettes of all objects >500 μm in size on all cruises. Size, shape, and density (visible as greyscale) all vary widely among individual marine snow particles.

The unique abilities to capture particles of a large size range including fragile marine snow particles makes the UVP a novel method for carbon flux estimates. Flux depends on the number, mass, settling rate, and diameter of each size class of particle. However, the UVP provides *in situ* data for only two of those four parameters, the number count and size

distributions of the particles. Particle properties that determine mass and settling rate, such as density, porosity, shape and composition, must be verified using sediment traps. Verification of those tangible properties can be used to establish methods for calculating flux based solely on particle counts and size distributions obtained with the UVP. For example, Guidi et al. (2008b) used derived power relationships to estimate carbon flux on a global scale. Derived equations were based off the empirical relationship fit between measured flux from sediment traps and the corresponding UVP size distributions at those locations. Given a particle size distribution, the Guidi et al. (2008b) empirical relationship can be applied to obtain an estimate of flux. In this way, having photographed the particles rather than collecting them, the flux of sinking particulate matter from surface waters to depth can still be approximated.

Conclusions

Overall, the UVP proved to be an excellent tool for analyzing the concentration and size distribution of 60 μm to 2.7 cm sized particles in seawater, including aggregates, marine snow particles, and many planktonic organisms. Its most innovative feature is the ability to be integrated with oceanographic profiling applications associated with CTD rosette casts, while generating size distributions and images of particles and plankton throughout the water column. Though size limitations exclude small phytoplankton cells and very fine particles <0.06 mm, the UVP creates much more detailed counts and sizes of every one of the individual objects 0.06- 26 mm captured in the photographs than any other optical method. It also captures images of gelatinous organisms and fragile marine snow particles that are often overlooked by traditional particle and zooplankton collection methods. Overall, the UVP would best be used in combination with a technique that captures smaller cells of phytoplankton more effectively, such

as fluorescence or an optical device like the LISST. This study also included the development of new documentation to provide users with step-by-step instructions for the use of the UVP alongside Zooprocess software. Future directions include the improvement of image sorting techniques for non-living marine particles in addition to zooplankton.

References

Alldredge, A., 1998. The carbon, nitrogen and mass content of marine snow as a function of aggregate size. Deep. Res. Part I Oceanogr. Res. Pap. 45, 529–541. doi:10.1016/S0967-0637(97)00048-4

Alpine, A.E., Cloern, J.E., 1985. Differences in in vivo fluorescence yield between three phytoplankton size classes. J. Plankton Res. 7, 381–390. doi:10.1093/plankt/7.3.381

Boss, E., Guidi, L., Richardson, M.J., Stemmann, L., Gardner, W., Bishop, J.K.B., Anderson, R.F., Sherrell, R.M., 2015. Optical techniques for remote and *in situ* characterization of particles pertinent to GEOTRACES. Prog. Oceanogr. 133, 43–54. doi:10.1016/j.pocean.2014.09.007

Boss, E., Slade, W.H., Behrenfeld, M., Dall'Olmo, G., 2009. Acceptance angle effects on the beam attenuation in the ocean. Opt. Express 17, 1535–1550.

Breiman, L., 2001. Random forests. Mach. Learn. 45, 5–32. doi:10.1023/A:1010933404324

Burd, A., Jackson, G., 2002. Shining a light on the ocean's twilight zone. EOS, Trans. Am. Geophys. Union 83, 579–580. doi:10.1029/2002EO000392

Burd, A.B., 2013. Modeling particle aggregation using size class and size spectrum approaches. J. Geophys. Res. Ocean. 118, 3431–3443. doi:10.1002/jgrc.20255

Burd, A.B., Jackson, G., Moran, S.B., 2007. The role of the particle size spectrum in estimating POC fluxes from disequilibrium. Deep Sea Res. Part I Oceanogr. Res. Pap. 54, 897–918. doi:10.1016/j.dsr.2007.03.006

Coyle, K.O., Pinchuk, A.I., 2005. Seasonal cross-shelf distribution of major zooplankton taxa on the northern Gulf of Alaska shelf relative to water mass properties, species depth preferences and vertical migration behavior. Deep Sea Res. Part II Top. Stud. Oceanogr. 52, 217–245. doi:10.1016/j.dsr2.2004.09.025

Coyle, K.O., Pinchuk, A.I., 2003. Annual cycle of zooplankton abundance, biomass and production on the northern Gulf of Alaska shelf, October 1997 through October 2000. Fish. Oceanogr. 12, 327–338. doi:10.1046/j.1365-2419.2003.00256.x

Ebersbach, F., Trull, T.W., 2008. Sinking particle properties from polyacrylamide gels during the Kerguelen Ocean and Plateau compared Study (KEOPS): Zooplankton control of carbon export in an area of persistent natural iron inputs in the Southern Ocean. Limnol. Oceanogr. 53, 212–224. doi:10.4319/lo.2008.53.1.0212

Fowler, S.W., Knauer, G., 1986. Role of large particles in the transport of elements and organic compounds through the oceanic water column. Prog. Oceanogr. 16, 147–194. doi:10.1016/0079-6611(86)90032-7

Gorsky, G., Ohman, M.D., Picheral, M., Gasparini, S., Stemmann, L., Romagnan, J., Cawood, A., 2010. Digital zooplankton image analysis using the ZooScan integrated system. J. Plankton Res. 32, 285–303. doi:10.1093/plankt/fbp124

Guidi, L., Calil, P.H.R., Duhamel, S., Björkman, K.M., Doney, S.C., Jackson, G., Li, B., Church, M.J., Tozzi, S., Kolber, Z.S., Richards, K.J., Fong, A., Letelier, R.M., Gorsky, G., Stemmann, L., Karl, D.M., 2012. Does eddy-eddy interaction control surface phytoplankton distribution and carbon export in the North Pacific Subtropical Gyre? J. Geophys. Res. 117, G02024. doi:10.1029/2012JG001984

Guidi, L., Gorsky, G., Claustre, H., Miquel, J.C., Picheral, M., Stemmann, L., 2008a. Distribution and fluxes of aggregates >100 μm in the upper kilometer of the South-Eastern Pacific. Biogeosciences 5, 1361–1372. doi:10.5194/bg-5-1361-2008

Guidi, L., Jackson, G., Stemmann, L., Miquel, J.C., Picheral, M., Gorsky, G., 2008b. Relationship between particle size distribution and flux in the mesopelagic zone. Deep Sea Res. Part I Oceanogr. Res. Pap. 55, 1364–1374. doi:10.1016/j.dsr.2008.05.014

Herman, W., 2004. The next generation of Optical Plankton Counter: the Laser-OPC. J. Plankton Res. 26, 1135–1145. doi:10.1093/plankt/fbh095

Holm-Hansen, O., Lorenzen, C.J., Holmes, R.W., Strickland, J.D.H., 1965. Fluorometric Determination of Chlorophyll. J. du Cons. / Cons. Perm. Int. pour l'Exploration la Mer 30, 3–15. doi:10.1093/icesjms/30.1.3

Hopcroft, R.R., Coyle, K.O., Weingartner, T.J., Whitledge, T.E., 2010. Gulf of Alaska Long-term Observations: the Seward Line 2008 / 9, NPRB Project Final Report. Fairbanks, Alaska.

Karp-Boss, L., Azavedo, L., Boss, E., 2007. LISST-100 measurements of phytoplankton size distribution: evaluation of the effects of cell shape. Limnol. Oceanogr. Methods 5, 396–406. doi:10.4319/lom.2007.5.396

McDonnell, A.M.P., Buesseler, K.O., 2012. A new method for the estimation of sinking particle fluxes from measurements of the particle size distribution, average sinking velocity, and carbon content. Limnol. Oceanogr. Methods 10, 329–346. doi:10.4319/lom.2012.10.329

McDonnell, A.M.P., Lam, P.J., Lamborg, C.H., Buesseler, K.O., Sanders, R., Riley, J.S.,

    Marsay, C., Smith, H.E.K., Sargent, E.C., Lampitt, R.S., Bishop, J.K.B., 2015. The

    oceanographic toolbox for the collection of sinking and suspended marine particles. Prog.

    Oceanogr. 133, 17–31. doi:10.1016/j.pocean.2015.01.007

Parsons, T.R., 1969. The use of particle size spectra in determining the structure of a plankton

    community. J. Oceanogr. Soc. Japan 25, 172–188.

Parsons, T.R., Maita, Y., Lalli, C.M., 1984. A Manual of Chemical and Biological Methods for

    Seawater Analysis. Pergamon Press, Oxford, England.

Picheral, M., Guidi, L., Stemmann, L., Karl, D.M., Iddaoud, G., Gorsky, G., 2010. The

    Underwater Vision Profiler 5: An advanced instrument for high spatial resolution studies of

    particle size spectra and zooplankton. Limnol. Oceanogr. Methods 8, 462–473.

    doi:10.4319/lom.2010.8.462

Proctor, C.W., Roesler, C.S., 2010. New insights on obtaining phytoplankton concentration and

    composition from *in situ* multispectral chlorophyll fluorescence. Limnol. Oceanogr.

    Methods 8, 695–708. doi:10.4319/lom.2010.8.695

Raskoff, K., Purcell, J.E., Hopcroft, R.R., 2005. Gelatinous zooplankton of the Arctic Ocean: *in*

    situ observations under the ice. Polar Biol. 28, 207–217. doi:10.1007/s00300-004-0677-2

Roberts, P.L.D., Jaffe, J.S., Orenstein, E.C., Laxton, B., Franks, P.J.S., Briseno, C., Carter, M.,

    Hilbern, M., 2014. Pier Recognition: An *in situ* Plankton Web Camera (Scripps Plankton

    Camera), in: Ocean Optics Meeting. Portland, Maine.

Sieburth, J.M., Lenz, J., 1978. Pelagic ecosystem structure : heterotrophic compartments of the

    plankton and their relationship to plankton size fractions. Limnol. Oceanogr. 23, 1256–

    1263.

Stemmann, L., Boss, E., 2012. Plankton and particle size and packaging: from determining

    optical properties to driving the biological pump. Ann. Rev. Mar. Sci. 4, 263–290.

    doi:10.1146/annurev-marine-120710-100853

Stemmann, L., Eloire, D., Sciandra, A., Jackson, G., Guidi, L., Picheral, M., Gorsky, G., 2008.

    Volume distribution for particles between 3.5 to 2000 μm in the upper 200 m region of the

    South Pacific Gyre. Biogeosciences Discuss. 5, 299–310. doi:10.5194/bgd-4-3377-2007

Turner, J.T., 2002. Zooplankton fecal pellets, marine snow and sinking phytoplankton blooms.

    Aquat. Microb. Ecol. 27, 57–102. doi:10.3354/ame027057

Verdugo, P., Alldredge, A.L., Azam, F., Kirchman, D.L., Passow, U., Santschi, P.H., 2004. The

    oceanic gel phase: a bridge in the DOM–POM continuum. Mar. Chem. 92, 67–85.

    doi:10.1016/j.marchem.2004.06.017

Young, H.D., 1962. Statistical Treatment of Experimental Data. McGraw-Hill Book Company,

    Inc., San Francisco, CA.

Chapter 2   Processes driving the spatial distributions of optically-imaged particles in the Gulf

of Alaska[1]

Abstract

The Gulf of Alaska is a biologically productive ocean region surrounded by coastal mountains

with high seasonal runoff from rivers and glaciers. In this complex environment, we measured

the concentrations and size distributions of large marine particles (0.06-27 mm) using the

Underwater Vision Profiler (UVP) during 4 cruises in 2014 and 2015. We analyzed the spatial

distribution of particles of different size classes to determine the probable drivers. Total

concentration of particles increased with proximity to glacial and fluvial inputs. We found a

major contrast between shelf and offshore particle concentrations. Over the shelf, concentrations

on the order of 1000-10,000/L were 1-2 orders of magnitude greater than offshore concentrations

on the order of 100/L. Driving processes over the shelf included terrigenous inputs from land,

resuspension of bottom sediments, and advective transport of those inputs along the shelf break.

Offshore, biological processes were drivers of variability in particle concentration and size with

depth. High quantities of terrigenous sediments could have implications for increased aggregate

flux via lithogenic ballast and the transport of particulate phase iron to the offshore iron-limited

gyre. The dominance of resuspended material in shelf processes will inform the location of

future studies of biogenic particle dynamics in the coastal Gulf of Alaska.

---

[1] Turner, J.T., Pretty, J.L, and McDonnell, A.M.P. Processes driving the spatial distributions of optically-imaged
particles in the Gulf of Alaska. Prepared for submission in Continental Shelf Research.

Introduction

Marine particles sequester atmospheric carbon dioxide and thus help to regulate global climate, transporting organic carbon to ocean depths at which it can be stored on longer time scales. This phenomenon is called the biological carbon pump (Broecker, 1982; Siegenthaler and Wenk, 1984; Volk and Hoffert, 1985). In coastal and shelf systems, sinking particles are an important food source for benthic organisms (Grebmeier et al., 1988), and in oceanic environments, deep-sea microbial and zooplankton communities rely on sinking organic matter as a habitat and a food source (Lampitt et al., 1993; Silver, 1978).

Although small particles <60 μm are argued to be important contributors to carbon flux (Dall'Olmo and Mork, 2014; Durkin et al., 2015; Richardson and Jackson, 2007), most studies agree that the greatest contribution to flux overall comes from relatively large (>100 μm) particle sizes (Fowler and Knauer, 1986; McCave, 1975; Riley et al., 2012; Stemmann et al., 2008). In particular, a middle size range of particles – which are both relatively large (~ 0.2-0.8 mm) and more abundant than the very large rare particles – make up the greatest portion of particle flux to depth (Ebersbach and Trull, 2008; McDonnell and Buesseler, 2012; Stemmann et al., 2004). However, our knowledge of this important particle size range is incomplete because many 100 μm – 1 mm scale particles are suspended or neutrally buoyant rather than quickly-sinking. Suspended particles can be as large as several cm and can outnumber sinking particles by two orders of magnitude (Baltar et al., 2010; Verdugo et al., 2004). Globally, suspended particles remain mostly unquantified (Arístegui et al., 2009; Baltar et al., 2009; Burd and Jackson, 2009). Constraining the composition of suspended or slowly settling particles could help close the gaps in many regional carbon budgets (Burd et al., 2010).

Traditional methods of measuring sinking and suspended sediments, though well developed, are imperfect for quantifying large particles from both pools (Bishop et al., 2012; Buesseler et al., 2007, 1992; McDonnell et al., 2015). Optical imaging tools provide alternate methods for quantifying both sinking and suspended pools *in situ* (Boss et al., 2015). *In situ* transmissometry, for example, is widely used in combination with CTD rosette packages, but even the most advanced transmissometers are not accurate for the measurement of particles >100 μm (Boss et al., 2009; Karp-Boss et al., 2007). Many photographic imaging systems have been designed to target larger objects; however, most lack either a reliable focus or a large enough sampling volume (Picheral et al., 2010). The large particles that contribute most to flux are relatively rare, so large volumes of water need to be sampled to count these objects in representative numbers (Burd et al., 2007; McCave, 1975; Walsh and Gardner, 1992). The Underwater Vision Profiler (UVP; Hydroptic, Inc.) has both a fine enough resolution to detect small particles and a large enough image volume and sampling frequency to count larger objects with statistical confidence (Picheral et al., 2010; Stemmann et al., 2008).

The UVP has been used to study particle dynamics in the South Pacific (Guidi et al., 2008a; Stemmann et al., 2008), the subtropical North Pacific (Guidi et al., 2012), the California current system (Ohman et al., 2012), the Southern Ocean (Jouandet et al., 2014), the Arabian Sea (Roullier et al., 2014), the Canadian Beaufort Sea (Forest et al., 2013, 2012), the North Atlantic and the Mediterranean Sea (Guidi et al., 2009, 2008b). These studies have used UVP concentrations and size distributions to estimate carbon flux on a global scale, using sediment traps and empirical equations to model flux in each region. Many regions of the global ocean remain unmapped by this new instrument; the subarctic North Pacific is one such place.

The Gulf of Alaska (GOA), including the eastern subarctic Pacific gyre north of ~54°N, is a high-latitude ocean region surrounded by glaciated coastal mountains, whose waters support high seasonal primary production (Napp, 1996; Sambrotto and Lorenzen, 1987). This region is characterized by iron limitation in the offshore environment contrasting with nitrate limitation over the shelf (Martin and Gordon, 1988). Most of the reactive iron, the fraction considered potentially available to biology, is ultimately sourced from glacial streams (Schroth et al., 2014, 2011). The particulate fraction of this micronutrient, along with the dissolved fraction, is an important component of the iron available to phytoplankton in the GOA, and the particulate fraction is especially important in the summer season (Aguilar-Islas et al., 2015; Lippiatt et al., 2010; Wu et al., 2009). Understanding the cross-shelf transport of this micronutrient via eddies is critical to the patterns of phytoplankton production in the central gyre (Ladd et al., 2005), a region of known iron limitation (Martin et al., 1989). Primary production over the shelf and in the offshore environment supports a large biomass of zooplankton (Coyle and Pinchuk, 2005, 2003), although the extent to which zooplankton organisms enhance or mitigate the flux of particulate organic carbon to depth is not well known. Particle dynamics are central to the functioning of the GOA ecosystem, through the physical transport of iron-rich terrigenous material and the phytoplankton and zooplankton interactions in the water column.

Research Objectives

The objectives of this study are to: 1) describe spatial variability in particle concentrations and size distributions, and 2) use that variability to identify driving processes and examine how the driving processes differ by region within the GOA. This study will explain the patterns observed and explore the physical and biological processes driving these patterns.

Methods

Sampling and Data Collection

Particle concentrations and size distributions were collected with the UVP on four cruises during two years (Table 2.1). In 2014, data were collected through collaboration with the Seward Line long-term observation program (LTOP) on the annual May and September cruises. In May-June 2015, data were collected on the CLIVAR repeat hydrography cruise P16N in the Pacific Ocean along the 152°W line of longitude and across the Alaska subpolar gyre from 149°W to the eastern shelf. Only the northernmost stations of the 152°W line will be discussed here (>54°N). In July-August 2015, data were collected throughout the coastal GOA on the NOAA Ocean Acidification (GOA-OA) cruise (Figure 2.1). This included Seward Line stations (Figure 2.2), eight other cross-shelf transects, and five entrances to sounds, straits and protected bays.

Cruise	*Date*	*Mounting Configuration*	*Acquisition Mode*
Seward Line	May 2-10, 2014	Separate Frame	I/O
Seward Line	September 16-21, 2014	CTD Rosette	I/O
P16N	May-June 2015	CTD Rosette	Depth
GOA-OA	July-August 2015	CTD Rosette	Depth and I/O

Table 2.1. Cruises included in Chapter 2, including sampling dates, mounting configuration used for UVP deployment, and acquisition mode used to collect data. Input-output (I/O) mode, or manually switching the UVP into acquisition mode before deployment, was used for shallow stations.
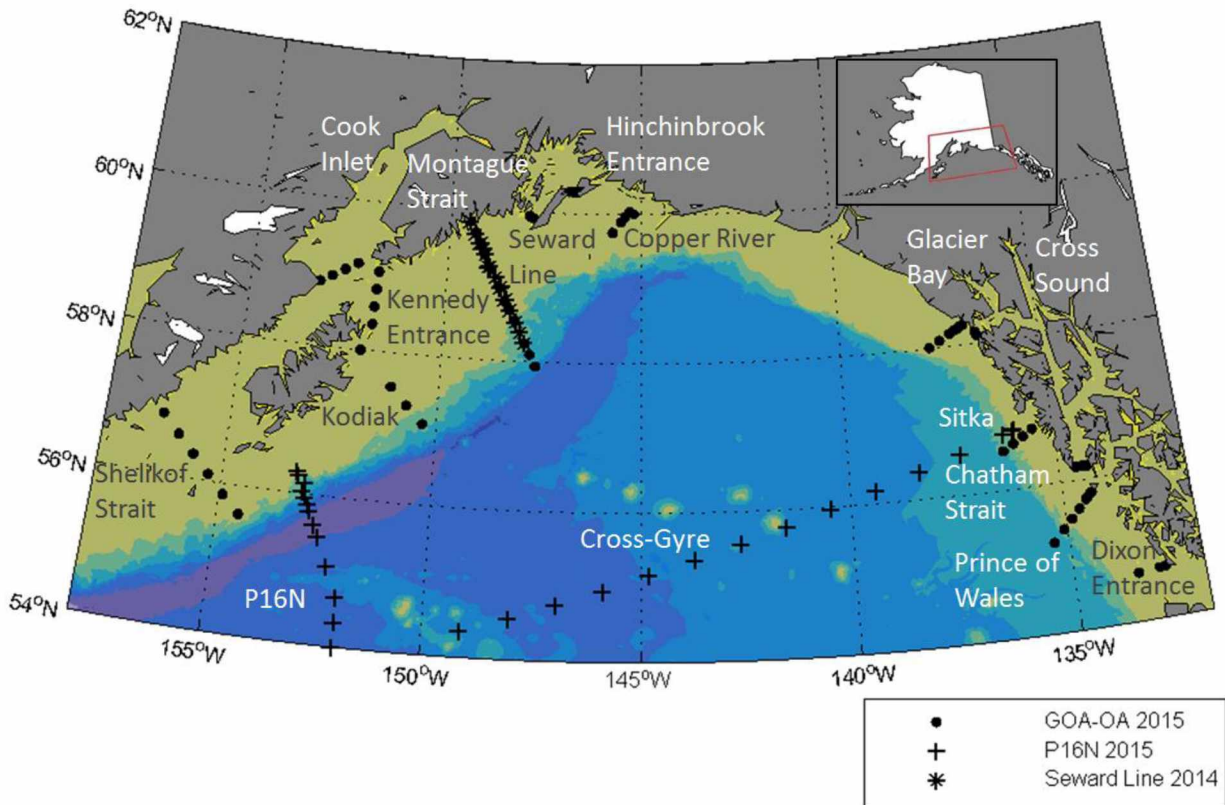
Figure 2.1. All stations sampled with the UVP in 2014-2015 in the Gulf of Alaska. Crosses indicate the northernmost stations of the P16N 152ºW line and the P16N Cross-Gyre line sampled in June 2015. Stars indicate the Seward Line stations sampled in May and September 2014. Circles indicate the GOA-OA cruise stations from July 2015. Names given to groups of stations will be used throughout the text to refer to those regions.
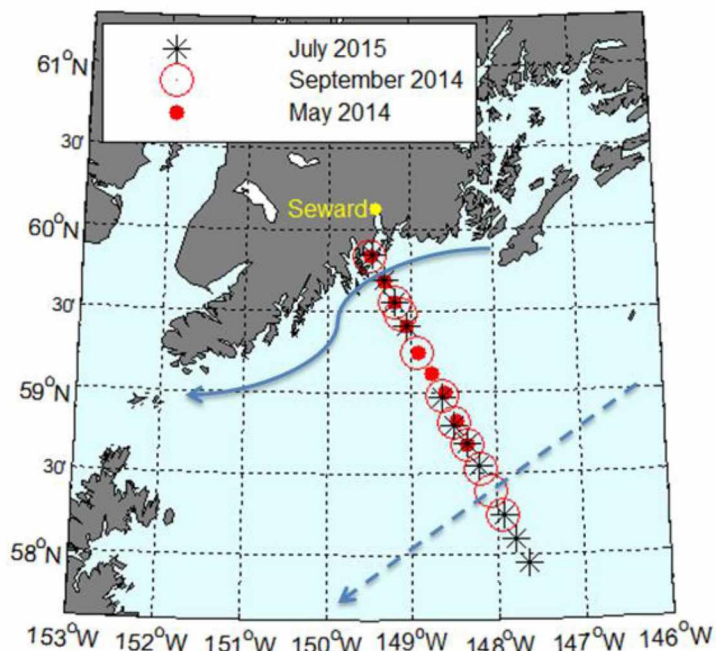
Figure 2.2. Seward Line stations sampled May 2014, September 2014 and July 2015. Solid dots indicate May stations, open circles indicate September stations, and asterisks indicate July stations. Nine to ten of the 13 stations were sampled in each season. Dashed and solid lines indicate idealized locations of the Alaskan Stream and Alaska Coastal Current, respectively.

The UVP was deployed using different mounting configurations and acquisition mode settings on each cruise (Table 2.1). In May 2014, the instrument was deployed in its own rectangular frame using a separate winch that reached 90 m depths, while in September 2014, May-June 2015, and July-Aug 2015, it was incorporated into the respective CTD rosette packages, recording full depth profiles of the water column. On both of the 2014 Seward Line cruises and at shallow stations on the GOA-OA cruise, the UVP was manually switched into acquisition mode on deck before deployments using the input-output (I/O) method. On the P16N cruise and the deep stations on the GOA-OA cruise, the instrument was instead programmed to automatically begin and end acquisition at certain descent and ascent cues recognized by the instrument's internal pressure sensor. On the P16N cruise, sampling depths on the northernmost stations of the 152 °W line were shallower (~2000 m) than the full-depth profiles on the Cross-

Gyre line due to battery malfunctions, which were repaired during the transit between the two lines.

The UVP photographed rectangular 1-liter parcels (0.93 L, will be referred to as 1-liter throughout) of water as it descended through the water column, with each image capturing all the particles 0.06-27 mm in equivalent spherical diameter (ESD) within each parcel. All cruises used mixed processing mode, which is designed to count and size particles while also saving .jpeg images of particles >0.5 mm ESD (Picheral et al., 2010). After downloading raw data from the UVP, only data from the downcast were used and numerical particle data were binned into 5-m depth bins.

Bottle Collection of Particulate Organic Carbon

On the September 2014 Seward Line cruise, particulate organic carbon (POC) measurements were collected using bottle collection and filtration at stations 1-13, numbered in order increasing with distance from shore (Figure 2.2). Six depths were chosen at each station, spaced as evenly as possible to include the surface, the chlorophyll maximum, and three other depths in addition to the bottom depth. 500 ml of seawater from each depth was filtered, a volume chosen based on both the 50 nmol C/L detection limit and the POC concentrations found in the North Pacific gyre in the JGOFS experiments (Bishop et al., 1999). Water was collected as quickly as possible (<10 min) after retrieval of the rosette and swirled before filtration to minimize particle settling. Each 500-ml sample was filtered through a 25 mm diameter, 0.2 μm silver membrane filter using vacuum suction. Filters were desiccated in individual petri dishes at 55° C for 12 hours, and then were packaged in tin disks and run through the CHN auto-analyzer at the Woods Hole Oceanographic Institution Nutrient Center for total carbon content.

Results

Overall spatial variability in the GOA in June-August 2015 showed a nearshore to offshore gradient in both particle concentration and size, with benthic boundary layers occurring throughout the entire region. On the Seward Line, a nearshore surface feature of elevated particle concentration was found in spring and summer while a shelf resuspension feature was found in summer and fall. Upon comparison with POC measurements, high particle concentrations measured by the UVP did not correlate with carbon-rich particulate matter, suggesting that the particles in high-concentration regions were inorganic.

Overall Gradients in Particle Concentration and Size

Overall, particle concentrations were highest at stations closest to large inputs of freshwater and glacial discharge, intermediate over the rest of the shelf, and lowest in the offshore regions (Figure 2.3). Spatial variability in particle sizes was marked by a similar gradient in particle size (Figure 2.4). Small particles 0.06-0.21 mm were proportionally more abundant in the northern GOA over the shelf, while large particles 0.21-2.6 mm were proportionally more abundant in the offshore GOA. Particle concentrations and size distributions with depth will be explained in three sections keeping these overall gradients in mind.
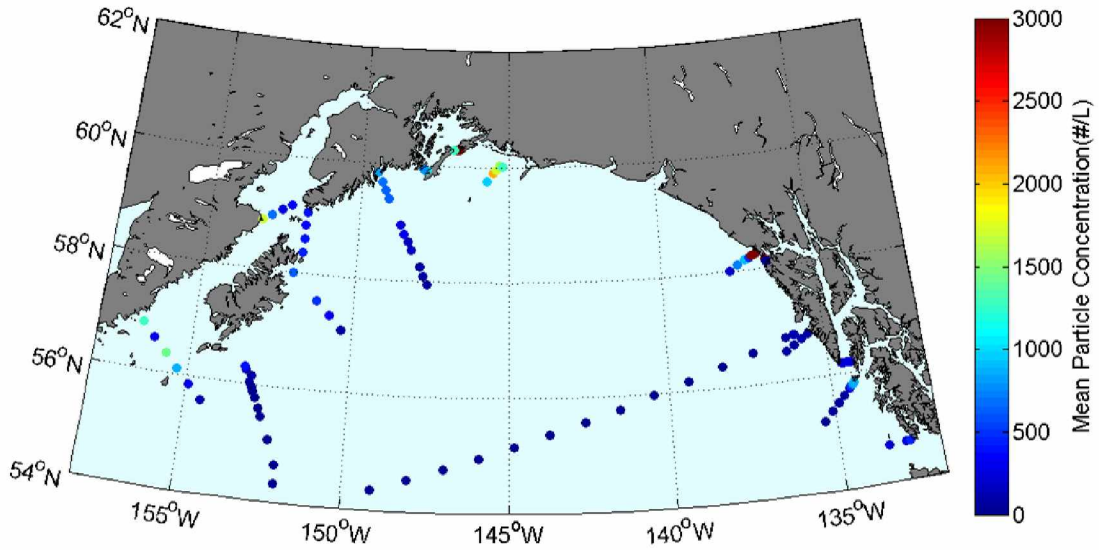
Figure 2.3. Map of the mean concentration of particles detected over the entire depth of the water column by the UVP (#/L) at each station in the Gulf of Alaska collected on P16N and GOA-OA cruises in June-August 2015.
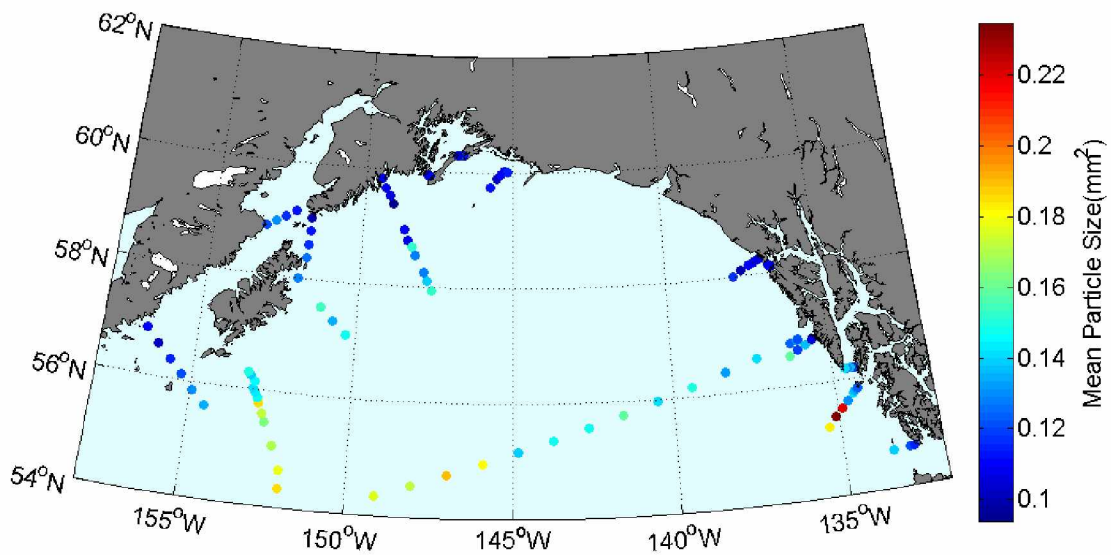
Figure 2.4. Map of the mean particle size (mm^2) in the top 100 m sampled at each station in 2015. Mean particle size increased with distance from shore. Nearshore, fine inorganic particles indicated lithogenic sediments, while offshore larger sizes were driven by biological particle dynamics.

Concentrations and Sizes: the Northeastern Region

Particle concentrations were highest in Cross Sound and just offshore of Glacier Bay in Southeast Alaska, and in the Copper River plume and the Hinchinbrook Entrance in the northern gulf (Figure 2.5). Cross Sound particle concentrations reached a maximum of 45000/L, an order of magnitude greater than the concentrations in the rest of the gulf (Figure 2.5 D). These high concentrations were found in the middle of the water column (20 to 150 m). Offshore of Glacier Bay, maximum particle concentrations of 4000/L were also found in the middle of the water column (40-120 m) close to shore (Figure 2.5 C). Along the Copper River line and in Hinchinbrook Entrance, maximum concentrations of 3500/L were found in a surface plume (<40 m) (Figure 2.5 B, A).

In the northeastern gulf region, a small average particle size was found in the top 100 m compared with the rest of the gulf (Figure 2.6). However, particle size patterns with depth were not always coupled with patterns in concentration. Along the Copper River line only, particles were smaller near the surface, mirroring the region of high concentration (Figure 2.6 B). In contrast, Cross Sound, Glacier Bay, and Hinchinbrook Entrance particle sizes did not necessarily mirror patterns in concentration. Instead, particle size was smaller at the surface in Cross Sound, at middle depths in Glacier Bay, and at bottom depths in Hinchinbrook Entrance (Figure 2.6 D, C, A).
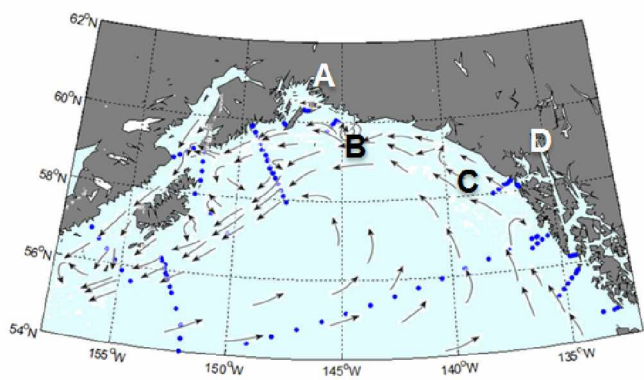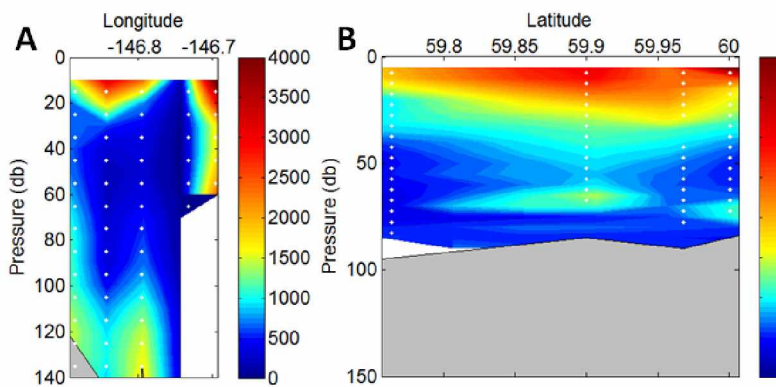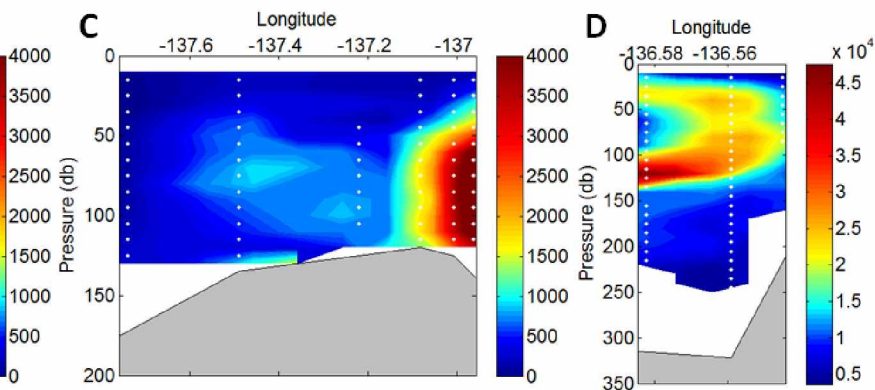
Figure 2.5. Particle concentrations (#/L) in the northeast region in 2015, A) in Hinchinbrook Entrance, B) offshore of the Copper River, C) offshore of Glacier Bay, and D) in Cross Sound. Note different color scale for Cross Sound, one order of magnitude greater than other locations. White dots indicate locations of data collection. Map indicates locations of subfigures with respect to current vectors from Muench & Schumacher (1980).
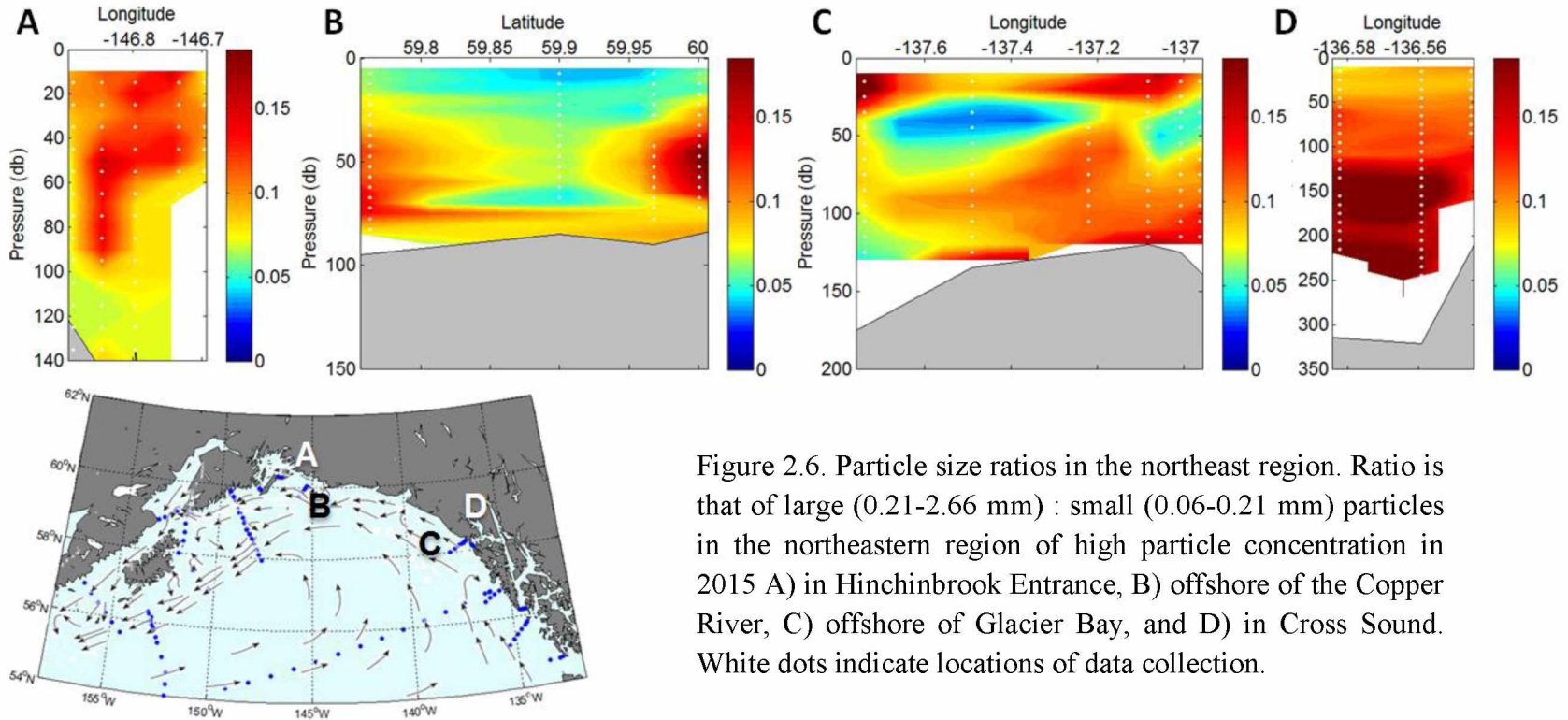
Figure 2.6. Particle size ratios in the northeast region. Ratio is that of large (0.21-2.66 mm) : small (0.06-0.21 mm) particles in the northeastern region of high particle concentration in 2015 A) in Hinchinbrook Entrance, B) offshore of the Copper River, C) offshore of Glacier Bay, and D) in Cross Sound. White dots indicate locations of data collection.

Fine particulate matter driving the elevated concentrations in the northeastern gulf was seen in the background of some of the large-object images (>0.5 mm) generated by the UVP. In September 2014 and July 2015, the images from nearshore stations at depths of maximum particle concentration had very blurry backgrounds full of small dots, showing the extreme turbidity of these waters (Figure 2.7).
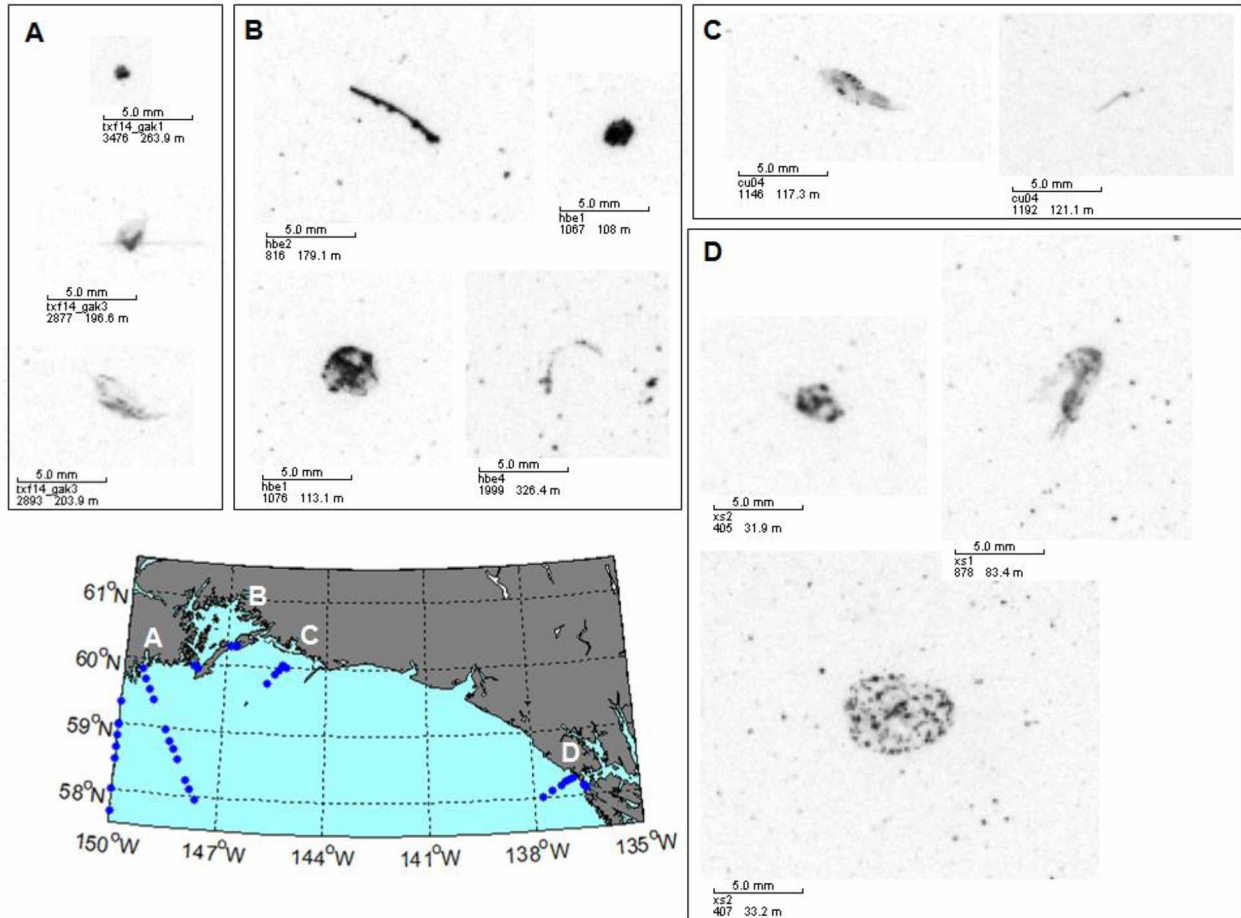
Figure 2.7. UVP large object "vignette" images with blurry backgrounds photographed by the UVP A) at nearshore Seward line stations in September 2014, as well as B) in Hinchinbrook Entrance, C) in the Copper River outflow, and D) in Cross Sound in July 2015. Scale bar indicates 5 mm, including station name, image number, and depth at which the image was photographed.

Concentrations and Sizes: the Intermediate Regions

Intermediate concentrations of particles (mean 1000-1800 /L) were found at nearshore stations outside of the northeastern region, including Dixon Entrance, Chatham Strait, Montague Strait, the Seward Line, Cook Inlet, Kennedy Entrance, Kodiak Island, and Shelikof Strait (Figure 2.8). Particle sizes were closely coupled with concentrations in these areas, with high concentrations coinciding with smaller particles (Figures 2.9). In all channels and entrances as well as off the northern end of Kodiak Island, maximum particle concentrations were found at bottom depths (Figure 2.8). These bottom depths were also regions of smaller particle size (Figure 2.9). High concentrations of 700/L were also found at the surface nearshore in Dixon Entrance (<30 m) and on the sides Chatham Strait at 100-250 m depths (Figure 2.8 A, B), and these features were also features of smaller particle size (Figure 2.9 A, B). Cook Inlet maximum particle concentrations of 2000/L were found along the western edge of the inlet at all depths (Figure 2.8 E), although the smallest particles were found only at bottom depths (Figure 2.9 E). Across Shelikof Strait, in addition to the benthic boundary layer signal, maximum particle concentrations of 2000/L were also found extending off the shelf at 50 and 200 m depths (Figure 2.8 G), and smaller particles were found in those high-concentration shelf break features (Figure 2.9 G).
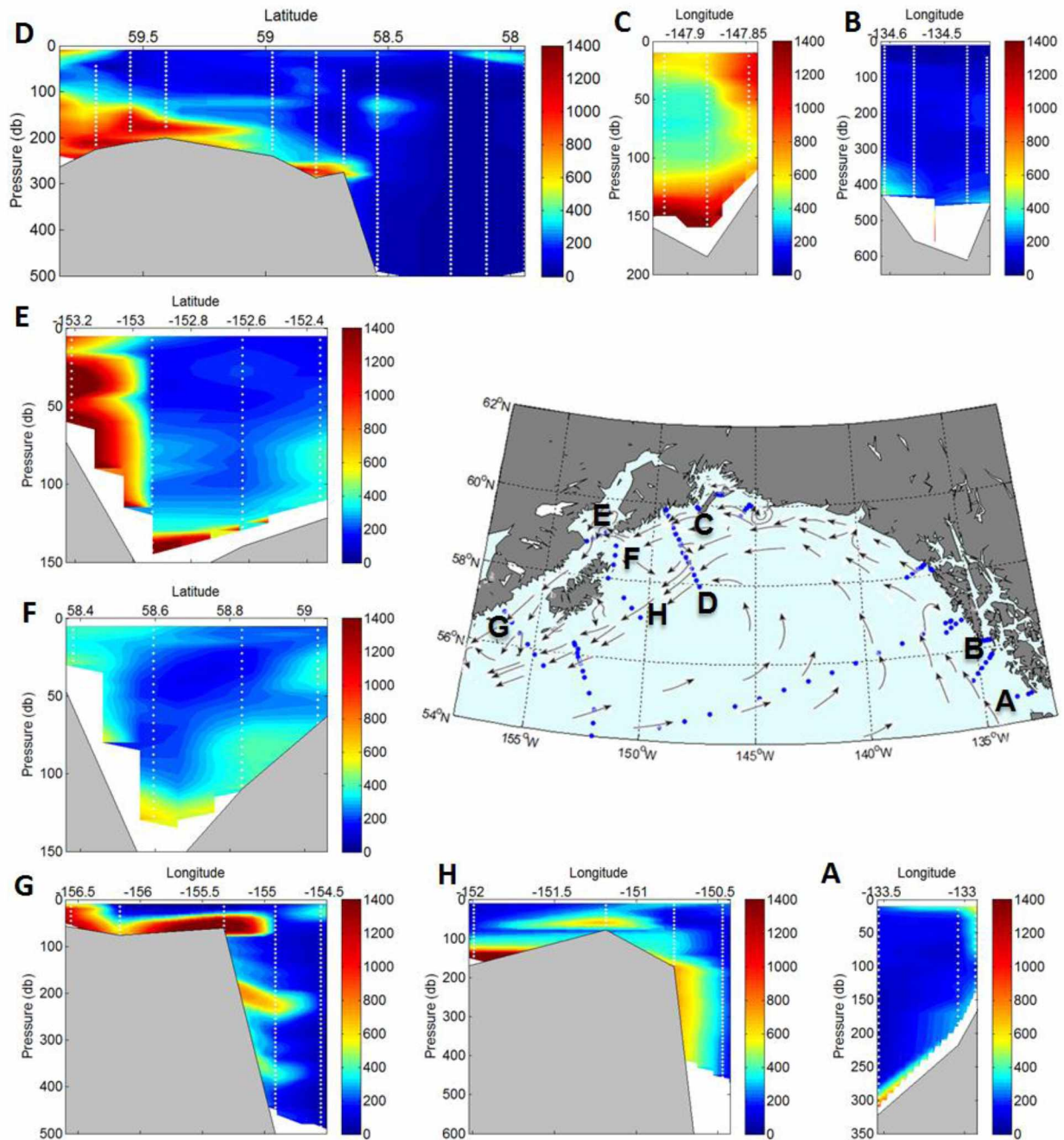
Figure 2.8. Particle concentrations (#/L) in the intermediate concentration regions in 2015, at locations over the shelf in the western and eastern Gulf in A) Dixon Entrance, B) Chatham Strait, C) Montague Strait, D) the Seward Line, E) Cook Inlet, F) Kennedy Entrance, G) Shelikof Strait, and H) off the northern end of Kodiak Island. White dots indicate locations of data collection. Map indicates locations of subfigures with reference to prevailing currents from Muench & Schumacher 1980.
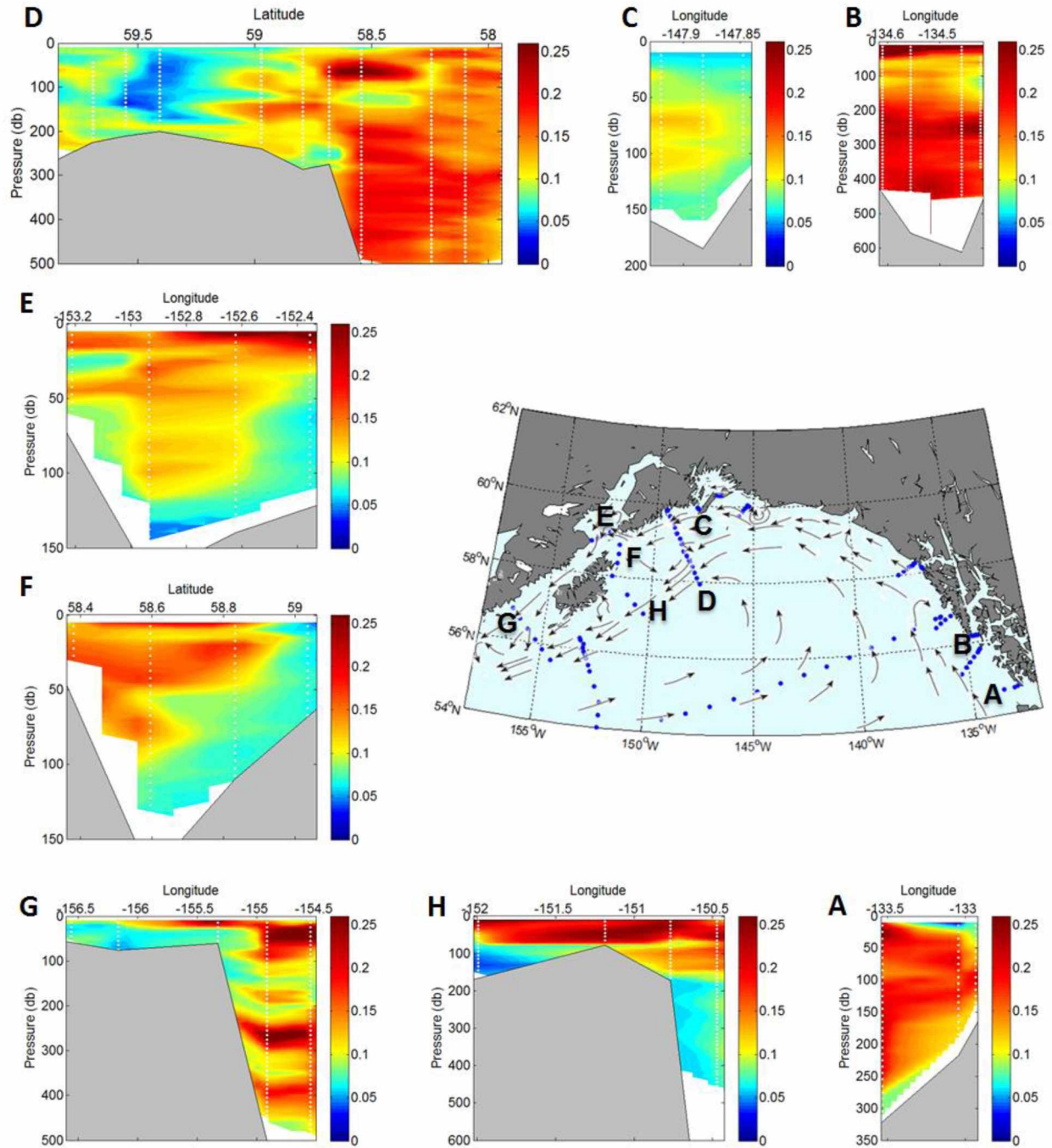
Figure 2.9. Particle size ratios in the intermediate concentration regions. Ratio is that of large (0.21-2.66 mm) : small (0.06-0.21 mm) particles at stations of intermediate concentrations in 2015 in A) Dixon Entrance, B) Chatham Strait, C) Montague Strait, D) the Seward Line, E) Cook Inlet, F) Kennedy Entrance, G) Shelikof Strait, and H) off the northern end of Kodiak Island. White dots indicate locations of data collection.

Concentrations and Sizes: the Offshore Region

The lowest concentrations of particles in the GOA were found at offshore stations, including the P16N line, the Cross-Gyre line, the transect leading to Sitka, and the Prince of Wales transect (Figure 2.10). Here, a greater mean size of particles (Figure 2.4) and a higher ratio of large: small particles (Figure 2.11) were observed. Along the P16N transect as well as the Cross-Gyre line, maximum concentrations were found at the surface (<50 m) at all stations and nearshore at all depths. On these two lines, particle size was larger just below the surface (20-100 m) offshore of the shelf and slope. The P16N line also had a feature of high particle concentration extending out from the slope at 800-1000 m depths near 56°N (Figure 2.10 B), which was marked by distinctly smaller particles (Figure 2.11 B). The Cross-Gyre line also had features of high particle concentration in subsurface (100-500 m) waters from 146°W to 139°W and in near-bottom nepheloid layers at most stations (Figure 2.10 A). Offshore of Sitka, maximum concentrations were found nearshore at 100-200 m depths (Figure 2.10 C). Particles were also smaller in these deep waters nearshore and extending off the shelf break (Figure 2.11 C). Along the Prince of Wales line, the highest concentrations were seen at bottom depths over the shelf and at the surface (<40 m) offshore south of 55.5°N (Figure 2.10 D). At bottom depths, high concentrations of 150-200/L were driven by smaller particles, while elevated concentrations of 100-150/L at the surface offshore were driven by larger particles (Figure 2.11 D).
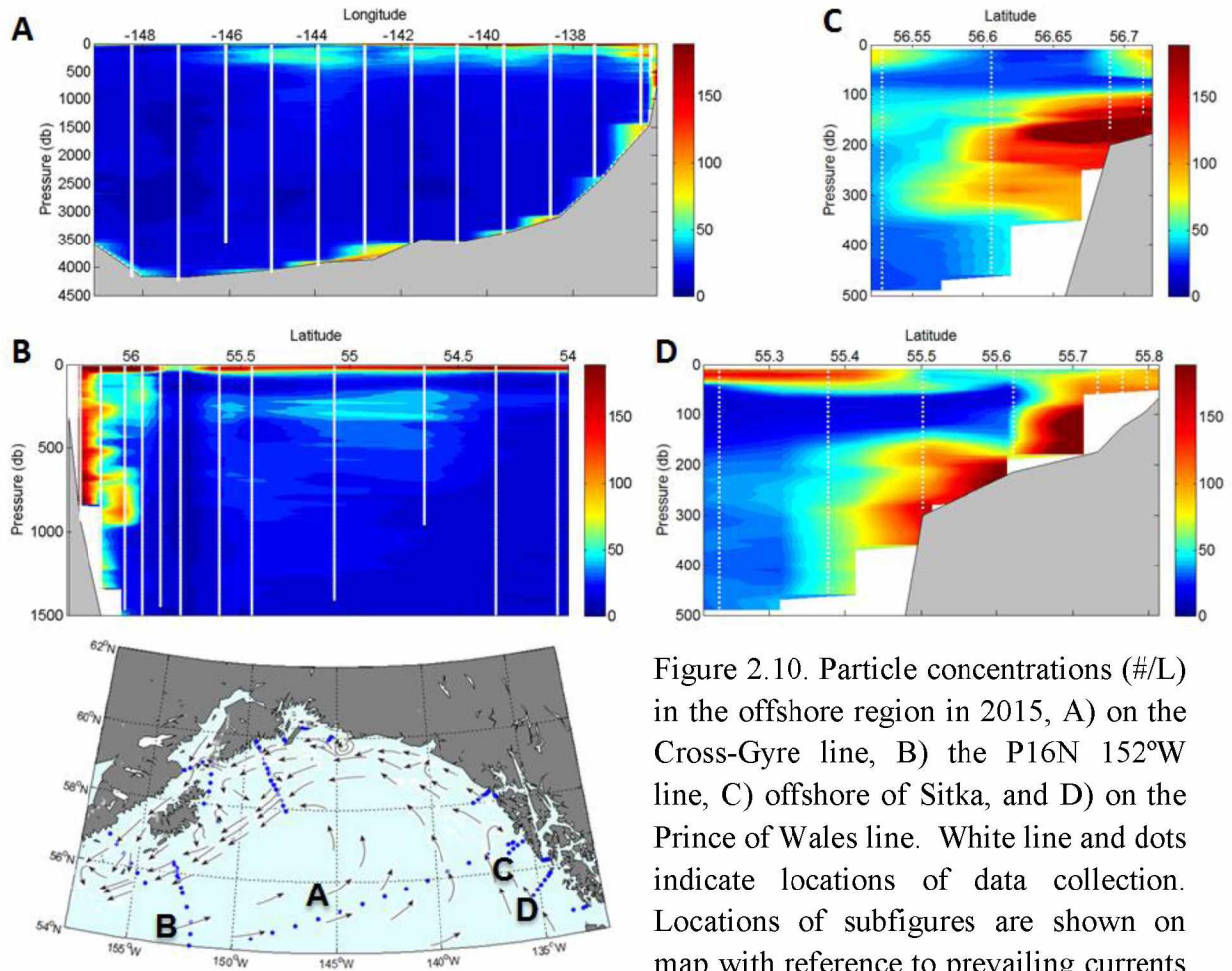
Figure 2.10. Particle concentrations (#/L) in the offshore region in 2015, A) on the Cross-Gyre line, B) the P16N 152°W line, C) offshore of Sitka, and D) on the Prince of Wales line. White line and dots indicate locations of data collection. Locations of subfigures are shown on map with reference to prevailing currents from Muench & Schumacher 1980.
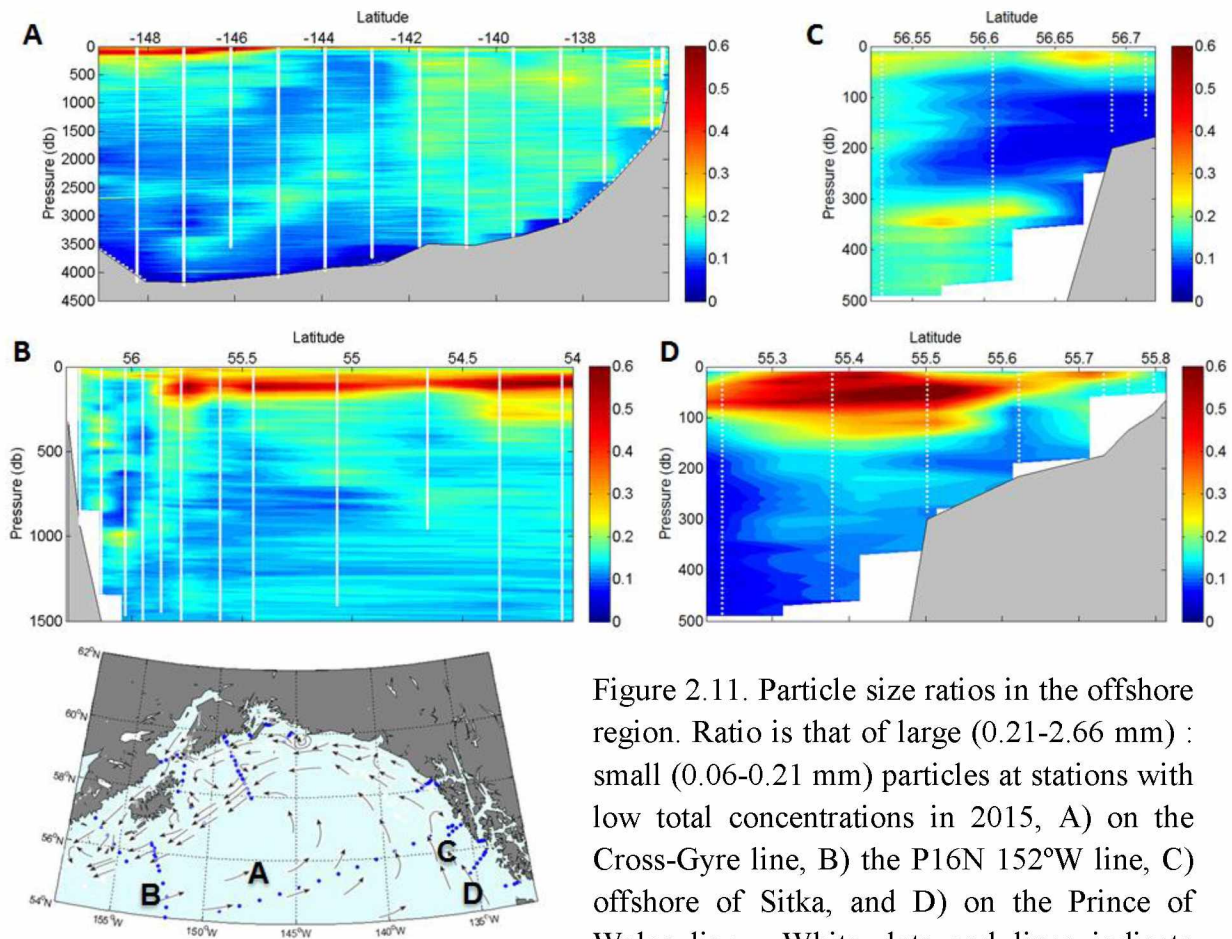
Figure 2.11. Particle size ratios in the offshore region. Ratio is that of large (0.21-2.66 mm) : small (0.06-0.21 mm) particles at stations with low total concentrations in 2015, A) on the Cross-Gyre line, B) the P16N 152°W line, C) offshore of Sitka, and D) on the Prince of Wales line. White dots and lines indicate locations of data collection.

In the center of the subpolar gyre, from 149°W to 145°W in the Cross-Gyre line, the mean vertical profiles of particle concentration, size, and greyscale revealed more about the dynamics of this offshore region (Figure 2.12). From the surface to depth, particle concentration was high at the surface, decreased to a subsurface minimum at 50-150 m, then increased again to a subsurface maximum above 500 m before decreasing exponentially. This concentration depth profile is directly opposite of depth profiles of mean particle size and mean particle greyscale. That is, where concentrations were highest, mean size and greyscale were decreased, indicating smaller, less dense particles at depths with high concentrations. These depth profiles, when

78

interpreted using the particle coagulation models presented by Burd & Jackson (2009), told a story of the change in drivers with depth. At the surface, phytoplankton production and zooplankton grazing activity caused the high concentration there, creating many small, light-colored objects such as individual phytoplankton cells, zooplankton fecal pellets, and detritus from zooplankton sloppy feeding. As these small, light-colored particles sank, they coagulated to form fewer, larger, darker-colored particles, indicated by a subsurface minimum in concentration. Then, as these aggregated particles were broken apart by zooplankton interactions in the deeper water column, particle concentration increased while mean size and greyscale decreased (Figure 2.12).
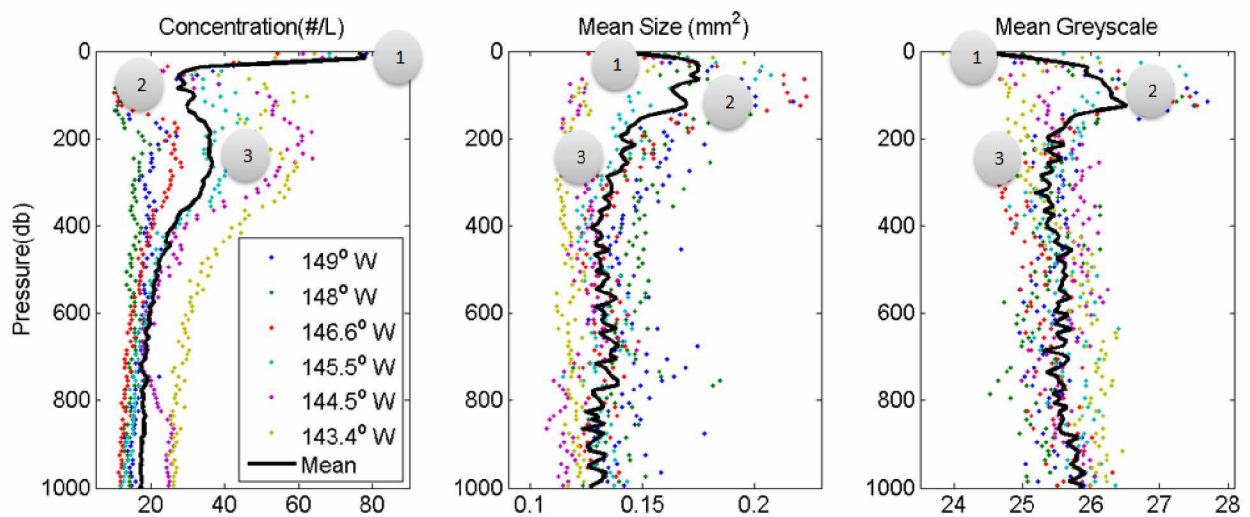
Figure 2.12. Offshore particle dynamics in the center of the subpolar gyre. Black line indicates mean concentration, mean size, and mean greyscale, and colored points indicate these values for all particles within each 10-m depth bin for six central-gyre stations from 149°-143.3°W. 1) Surface (<50 m) maximum concentration coincides with small mean size and light-colored greyscale. 2) Subsurface (50-150 m) minimum concentration coincides with larger mean size and darker greyscale. 3) Deeper (150-400 m) slight increase in concentration coincides with smaller mean size and lighter greyscale.

Although results for mean size in the top 100 m of the water column (Figure 2.4) and size ratios at depth (Figures 2.6, 2.9., 2.11) showed a nearshore to offshore gradient in small to large sizes, this overall trend did not explain all size classes at all depths. Concentration size distributions (CSD) from three shelf stations and two offshore stations showed that increased particle concentrations at depth nearshore were driven by small particles over the shelf, but driven by larger particles in narrow entrances (Figure 2.13 A,B,C). Increased particle concentrations at the surface offshore were driven by all particle sizes, especially those in the 0.2-0.8 mm range (Figure 2.13 D, E).
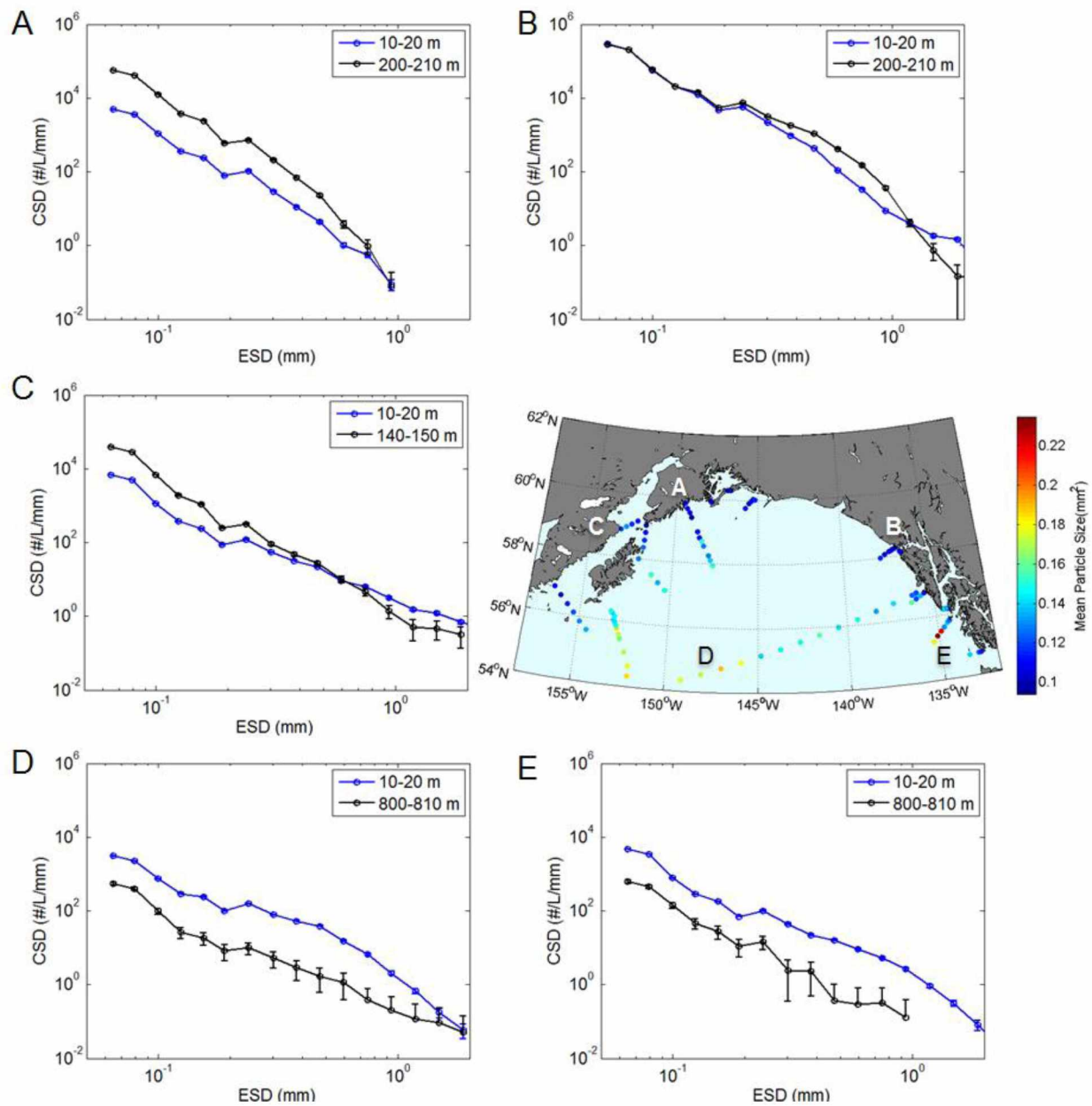
Figure 2.13. Concentration size distributions (CSD) in five representative locations for particles at the surface and at depth, A) Station GAK7 on the Seward Line over the mid-shelf, B) Station XS2 in Cross Sound at the center of the channel, C) Station CI4 on the western side of Cook Inlet, D) Station 194 on the Cross Gyre line at ~148°W, and E) Station POW8 as the most offshore station in the Prince of Wales line. Greater particle concentrations at depth nearshore were driven by smaller particles on the Seward Line and in Cook Inlet (A, C) but driven by larger particles in Cross Sound (B). Particle concentrations offshore were greater at the surface for all size classes, particularly 0.2-0.8 mm sizes (D, E).

Along the Seward Line, May and July both exhibited a nearshore, near-surface feature of high concentration dominated by small particle size classes. July and September were both characterized by high-concentration, small-size regions in benthic boundary layers over the shelf, although in September this shelf signal was more pronounced.

In May 2014, maximum particle concentrations were seen close to shore and decreased with distance from shore (Figure 2.14 A). Small particles were most abundant nearshore at surface depths (<60 m), as a smaller mean size and a lower ratio of large: small particles were present in these nearshore surface waters occupied by the ACC (Figure 2.14 D).

In July 2015, maximum particle concentrations were found at the surface nearshore, similar to the patterns seen in May. Very high concentrations were also found in bottom waters over the shelf, similar to the elevated shelf concentrations in September (Figure 2.14 B). Small particles were proportionally more abundant over the shelf at all depths, particularly between 100-200 m nearshore and at 50-150 m near the shelf break (Figure 2.14 E).

In September 2014, maximum particle concentrations were seen below the surface over the shelf at depths of 75 to 250 m, and concentrations were especially high nearshore. High concentrations extended out from the shelf break at ~250 m depths from GAK 8-9 and were found in a prominent high-concentration feature in the subsurface waters (75-150 m) just before the shelf break at GAK 7 (Figure 2.14 C). Small particles were proportionally most abundant over the shelf, as well as in the features above the shelf break and extending out from the shelf break at depth (Figure 2.14 F).
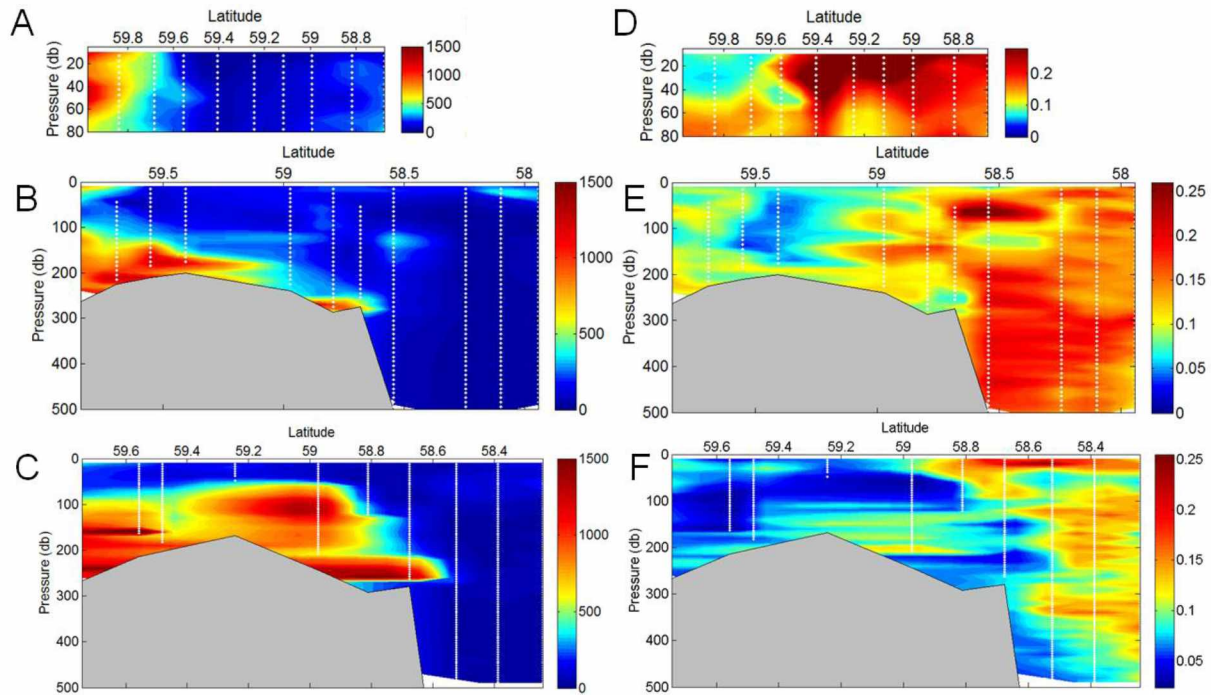
Figure 2.14. Seward Line temporal variability in total particle concentration (#/L) (A, B, C) and particle size ratios (0.21-2.6 mm: 0.06-0.21 mm) (D, E, F). Data were collected in May 2014 (A, D), July 2015 (B, E), and September 2014 (C, F). White dots and lines indicate locations of data collection.

On the Seward Line in May 2014, a nearshore surface plume of elevated particle concentration was dominated by small size classes and negatively correlated with salinity. As salinity increased, particle concentration decreased, particularly at the two stations closest to shore (Figure 2.15). This relationship supports the hypothesis that elevated particle concentrations nearshore were driven by inputs from rivers, particularly rivers that include glacial runoff.
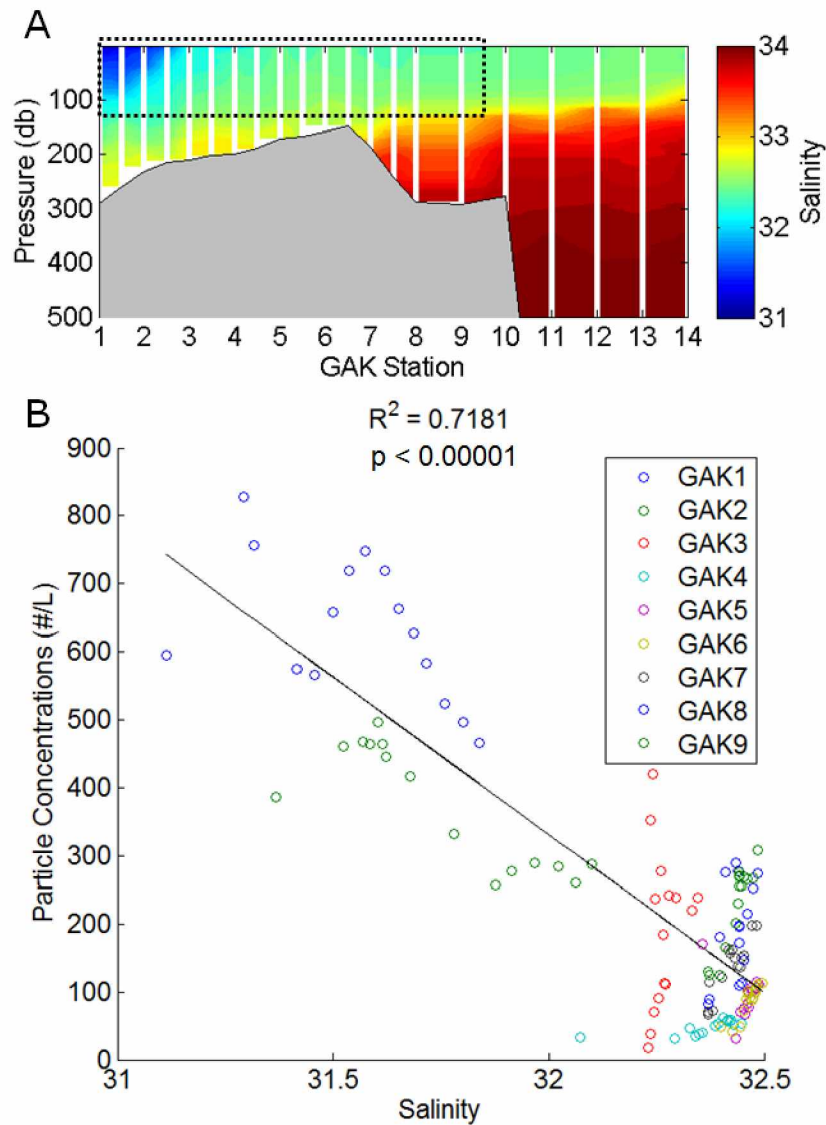
Figure 2.15. A) Salinity on the Seward Line in May 2014. White lines indicate locations of CTD rosette casts. Dashed box indicates where the UVP also collected data. B) Ordinary least squares regression for salinity and UVP total particle concentration (#/L), binned in 5-m depth intervals and using only data from the depths and stations where both the UVP and CTD collected data (N=135). Particle concentration decreases as salinity increases (R^2=0.7181, p <0.00001). Point colors indicate different stations, with GAK1 and GAK2 located closest to shore.

84

Comparison with Bottle-Collected POC on the Seward Line

In September 2014 on the Seward Line, high particle concentration was not correlated with high carbon composition of particles (R^2=0.0119, p=0.433) (Figure 2.16). Spatial patterns in particle concentration did not resemble patterns in POC. Regions of high carbon content hosted some of the lowest particle concentrations, such as the surface waters over the shelf. Likewise, regions of high particle concentration showed low carbon values, such as bottom depths over the shelf. This suggests that the areas of high particle concentration and small size classes were dominated by inorganic particles.
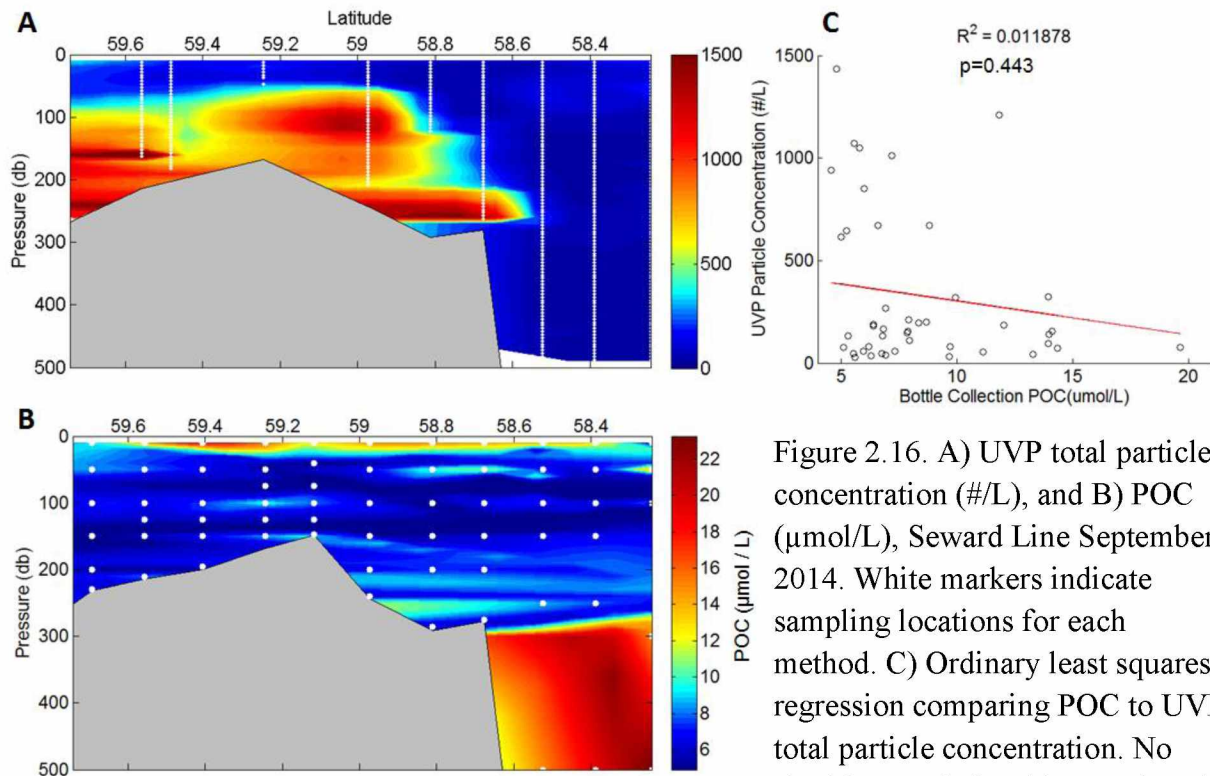
Figure 2.16. A) UVP total particle concentration (#/L), and B) POC (μmol/L), Seward Line September 2014. White markers indicate sampling locations for each method. C) Ordinary least squares regression comparing POC to UVP total particle concentration. No significant relationship was found (R^2=0.011878, p=0.433).

To further investigate the differences between POC from bottle collection and particles detected by the UVP, we looked at the relationships between POC and each UVP particle size class at the depths and stations where POC was measured. Although relationships were

statistically weak (R^2<0.1), linear regressions revealed a significant negative relationship between POC and small size classes 0.065-0.99 mm (p=0.047), and a significant positive relationship between POC and larger size classes 0.94-1.49 mm (p=0.0016; Figure 2.17). These results suggest that millimeter-scale particles are more carbon-rich than the finer micron-scale particles.
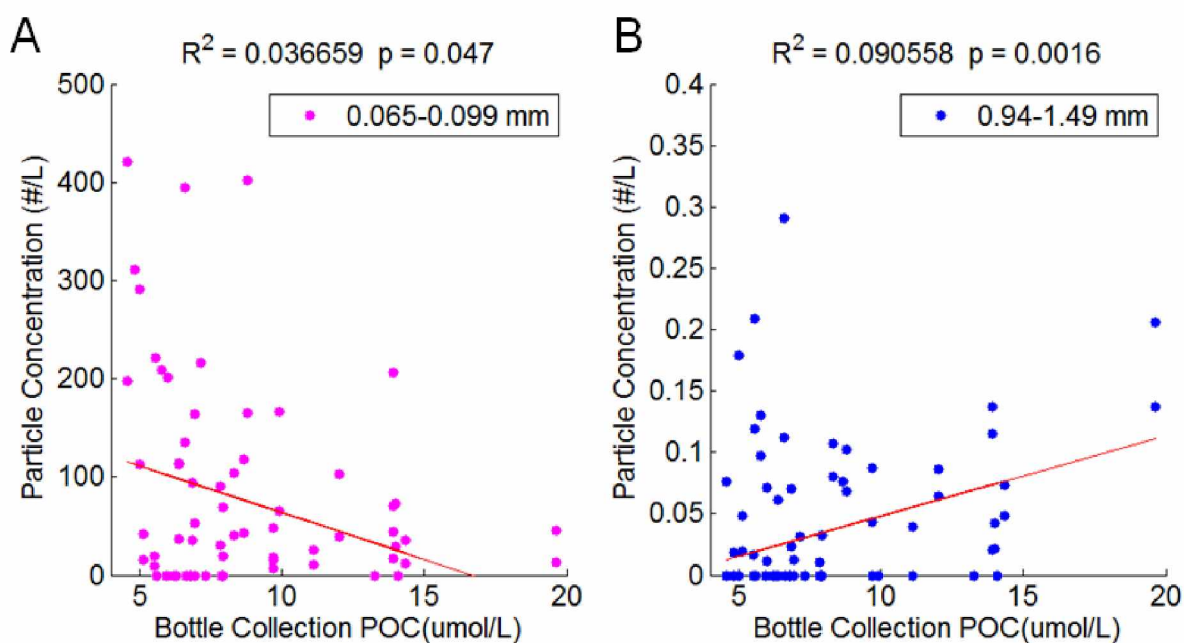
Figure 2.17. Ordinary least squares regressions for POC and UVP size classes, A) small particles 0.065-0.099 mm and B) larger particles 0.94-1.49 mm. Weak but significant relationships were found for both size groups with POC; small particle concentrations decreased as POC increased (p=0.047) while larger particle concentrations increased as POC increased (p=0.0016).

Discussion

Over the shelf, spatial variability in particle concentration and size was driven by physical processes. These physical drivers included runoff from rivers and glaciers, as well as mixing forces, which resuspended bottom sediments and transported the inorganic particles both

along and across the shelf. In the offshore GOA, low particle concentrations and more abundant large size classes indicated that biological particle dynamics controlled spatial variability.

Nearshore Riverine and Glacial Discharge

The highest concentrations of particles overall were found closest to the most glaciated coastlines and the largest river inputs. For example, in Cross Sound and offshore of Glacier Bay, we found some the highest concentrations of particles in this study (Figures 2.3, 2.5). Cross Sound is the principal exit for waters that drain the numerous glaciers feeding into Glacier Bay (Weingartner et al., 2009), including the Brady icefield and the diffuse glaciers of the Takhinsha Mountains and the St. Elias Mountains (Molnia, 2008; Neal et al., 2010). Glacial scouring leads to fine grained sediment input from both inland and tidewater glaciers (Burbank, 1974; Powell and Molnia, 1989).

Another example of high inputs of lithogenic particles from land was the northernmost section of the GOA, including offshore of the Copper River, in Hinchinbrook Entrance, and in Montague Strait. The Copper River drains a large, mountainous watershed area of 62,678 km^2, producing a discharge of 56 km^3 annually, 69% of which comes from glacial sources (Neal et al., 2010). The ACC then advects this outflow west and north with some entering Prince William Sound (PWS) through Hinchinbrook Entrance (Burbank, 1974; Stabeno et al., 2004). Water flows out of PWS through Montague Strait to the west, after encountering the outflow from the Columbia glacier and other diffuse glaciers and coastal rivers surrounding the Sound (Neal et al., 2010; Royer, 1982). Inputs from land drive the high concentrations of particles seen over the shelf adjacent to the Copper River. Hinchinbrook Entrance and Montague Strait are

progressively downstream of that outflow, so particle concentrations in these areas were similarly elevated, enhanced by the intense mixing forces in the narrow channels.

In nearshore surface plumes, high particle concentrations seen by the UVP were indicative of lithogenic material sourced from coastal rivers and glaciers. The strong relationship between salinity and particle concentration on the Seward Line in May 2014 supports this idea (Figure 2.15). Other studies' findings from the last few decades also support this hypothesis. Aside from the Copper River, the GOA has few large point source inputs of freshwater and terrigenous sediments, which are instead supplied via diffuse small mountain streams (Royer, 1982). These types of inputs are less predictable in the timing of their discharge than large river inputs due to the small buffering capacities of the steep, mountainous watersheds (Milliman and Syvitski, 1992; Wheatcroft et al., 2010). Iron concentrations also decrease with distance from shore in the northern central GOA. For example, on the Seward Line in May and July 2004, particulate and colloidal iron concentrations were quickly removed from surface waters and effectively trapped near the coast within nearshore ACC waters (Wu et al., 2009). This provides further support for the hypothesis that the high concentration of particles seen by the UVP is driven by lithogenic material in nearshore surface waters (Aguilar-Islas, personal comm.). In another past study, shallow Secchi depths were correlated with lower salinities in nearshore environments in Southeast Alaska. This pattern was attributed to glacial silt-laden river runoff nearshore and the subsequent sinking of that silt offshore as it coagulated (Pickard, 1967). A later study found that aluminosilicates were at a much higher concentration than carbon in suspended particulate matter in the north-central part of the gulf, indicating coastal rivers as the source (Feely et al., 1981, 1979). This fresh, sediment laden water is characteristic of the ACC, which stays very close to the coast when driven by inputs of freshwater (Royer, 1982). This

pattern is most pronounced in the summer during times of high freshwater discharge, as seen in the extreme decreasing nearshore to offshore gradient in dissolved aluminum (Brown et al., 2010). Physically, this coastal-trapped river plume with distinctly low salinities and high particle concentrations is characteristic of what one study calls the Riverine Coastal Domain, a feature of shelf circulation that unifies the coastal GOA with the Bering, Chukchi, and Beaufort seas downstream (Carmack et al., 2015).

Resuspension of Bottom Sediments

The most widespread physical driver of particle concentration over the shelf was the vertical resuspension of bottom sediments. Every cross-section except for Cross Sound showed some kind of benthic boundary layer at bottom depths (Figures 2.5, 2.8 and 2.10). In some places, such as the Cross-Gyre line, the benthic boundary layers extended up tens of meters to even hundreds of meters in places (Figure 2.10 A). These particles, like those in the nepheloid layers over the shelf, were small in size, indicated by a large: small particle ratio very close to zero. Over continental shelves globally, 15-50% of particulate material initially deposited is resuspended and redeposited over the shelf (Hedges and Keil, 1995). In past studies in the GOA, turbid plumes were found at bottom depths over the shelf, caused by resuspension (Feely et al., 1979; Hampton et al., 1987). Trace element distributions of the suspended matter matched those in bottom sediments, indicating that resuspension was indeed the source of the material (Feely et al., 1981, 1979). These past studies support the idea that the high particle concentrations seen at bottom depths are mostly inorganic.

Because even the smallest particles detected by the UVP were relatively large and therefore had faster sinking rates in terms of Stokes' Law, vertical resuspension was most likely

the dominant mechanism for the large amounts of small particles present over the shelf (Table 2.2). However, along- and cross-shelf transport were still possible mechanisms for particles that were less dense or more porous than the hypothetical lithogenic particles used to calculate the scales of transport in Table 2.2.

Height of resuspension (m)	Settling time (hr)	Advection length (km)
10	0.8	0.57
20	1.6	1.15
30	2.4	1.73
40	3.2	2.30
50	4.0	2.88
100	8.0	5.76

Table 2.2. Calculated advection length (km) that a 62.5 μm particle would be transported in a 20 cm/s horizontal current before settling to the seafloor, as a function of the height of resuspension above the shelf, based on Stokes' Law and a lithogenic particle density of 2.292 g/cm^3.

Cross-Shelf Transport

Over the continental shelf, transport of suspended sediments could be seen near the shelf break in the offshore direction. For example, on the Seward Line in September 2014, high concentrations of particles small in size extended out one station (~18 km) past the shelf break (Figure 2.14). In July 2015 at Shelikof Strait, maximum particle concentrations were found not only at the very edge of the shelf break, but also extending out from the shelf break at three depth intervals (Figure 2.5 G). Over the P16N line, a high-concentration feature could be seen at 800-1000 m of small sized particles extending out from the continental slope (Figure 2.10 B). This could be evidence of the downwelling process set up by wind and current regimes in the GOA. Though more pronounced in winter, the downwelling of cold, dense water masses can bring

along sediments as they flow from the shelf to the deep basin (Feely et al., 1979; Ladd et al., 2005; Royer, 1975).

The shelf is broader in the western GOA than in Southeast Alaska, broadening from less than 50 km near Sitka to ~200 km near Cook Inlet and Kodiak Island (Stabeno et al., 2004). The observed contrast in particle concentration between the western region, on the order of 2000/L, and the southeastern region, on the order of 200/L, could be a product of the differences in shelf topography. The broadening, shallowing shelf provides more area over which shelf sediments can be resuspended. Broader shelf area, combined with the presence of submarine canyons, provides more conduits for cross-shelf sediment transport over the western shelf than over the southeastern shelf.

Tidal mixing could also be a contributing mechanism to the high particle concentrations seen in channels and stations with distinct submarine canyons in the shelf. Tidal mixing has been calculated to be a primary driver for transport of nearshore sediments in the GOA (Burbank, 1974). For example, tidal mixing enhances the transport of particles in the outflowing side of Cook Inlet. Data collected with the UVP showed elevated particle concentrations on the west side of the inlet where water exits to rejoin the ACC (Figure 2.8 E). Cook Inlet is home to some of the largest tide ranges in the world, reaching up to 11.4 m fluctuations at spring tide (Bartsch-Winkler and Ovenshine, 1984), providing high energy to mix and resuspend sediments as they are exported to rejoin the ACC flowing to the southwest. To the southwest, the shelf offshore of Kodiak Island is riddled with submarine canyons (Carlson et al., 1982), in which tidal mixing is especially strong due to their bathymetric shape (Ladd et al., 2005). Data collected with the UVP showed elevated particle concentrations at bottom depths in these areas (Figure 2.8 F, G, H). To the east, the order-of-magnitude higher particle concentrations in Cross Sound

could be enhanced by tidal mixing as well, because Cross Sound experiences the highest tidal velocities in Southeast Alaska at 2 m/s (Weingartner et al., 2009).

Along-Shelf Transport

Transport by currents could also be seen in the connectivity of particle distributions between transects, as well as in a feature over the Seward Line shelf in September 2014. Particle transport was inferred from one transect to the next following the direction of predominant currents. Based on the qualitative trends in spatial patterns of particle concentration, we hypothesize that due to the counterclockwise direction of the ACC and Alaskan Stream, the highest concentrations of particles sourced from glacial areas in the northeastern Gulf would be expected to be transported downstream and gradually decrease in concentration with distance from those glacial and fluvial inputs. This gradual decrease is expected as the suspended sediments carried from river mouths settle out with distance from the source (Table 2.2). Cross Sound particles are transported out into the gulf offshore of Glacier Bay, and can be seen in the high-low gradient in particle concentration from the nearshore stations to the offshore stations (Figures 2.3, 2.5). Farther downstream in this current system, the Copper River particles are transported into Prince William Sound through Hinchinbrook Entrance, after which they exit through Montague Strait. Even farther downstream, Cook Inlet sediments flow into Shelikof Strait. High concentrations on the western side of Cook Inlet are being transported out of the inlet and down into Shelikof Strait via the ACC, and elevated particle concentrations can be seen at these locations in the UVP data (Figure 2.8). This along-shelf transport of suspended particles was seen in past studies (Burbank, 1974; Carlson and Molnia, 1978) and fits with the schematic model of the Riverine Coastal Domain described by Carmack et al. (2015), in which circulation

is constrained by both a nearshore coastal current at the surface as well as a parallel subsurface current at the shelf break.

In September 2014, the high particle concentration feature at GAK7 (Figure 2.14 C), though not in contact with the shelf, could be explained by physical process as well. The idealized Alaskan Stream usually flows through the Seward Line stations just past the shelf break (Wu et al., 2009) but it has been known to vary in position depending on the wind stress and other physical drivers of the subarctic gyre as a whole (Reed, 1984), so it is not unreasonable for it to veer slightly north as it passes the Kenai Peninsula, especially in fall and winter. The Alaskan Stream is located at about 100-150 m depths (Feely et al., 1981) and reaches its fastest velocities near the shelf break (Hampton et al., 1987). Based on its features, this current could explain the feature of high particle concentration that was centered in the middle of the water column (Figure 2.14 C).

Scale of Particle Transport

Since this dataset was composed of several cross-shelf transects, making it difficult to separate the effects of resuspension and lateral transport, it was necessary to estimate whether the scale of the hypothesized physical transport was reasonable. To estimate the relative contribution of these mechanisms, an advective length scale for the transport of a 62.5 μm lithogenic particle suspended in a 20 cm/s horizontal current was calculated as a function of height above the seafloor. This particle size falls within the lowest size class that can be detected with the UVP, and is the upper limit for the geological definition of silt (Krumbein and Aberdeen, 1937). A 20 cm/s current speed is a reasonable intermediate velocity of either the ACC or Alaskan Stream (Ladd et al., 2005; Stabeno et al., 2004). In short, even if a particle of

this size were resuspended 100 m above the shelf, the length scale of advection for that particle would be less than 6 km (Table 2.2). This relatively short horizontal distance implies that the dominant mechanism for increased particle concentrations over the shelf is vertical resuspension rather than horizontal advection.

This calculation assumed spherical particles with smooth textures as per Stokes' Law (Krumbein and Pettijohn, 1938). It also assumed a lithogenic particle density of 2.292 g/cm^3, which is denser than most unballasted organic matter (~1.060 g/cm^3) but not as dense as calcium carbonate (~2.710 g/cm^3) (Klaas and Archer, 2002). Less dense particles, as well as faster current speeds, would result in greater distances of horizontal transport than our calculation. Therefore, horizontal advection may still be a mechanism for particle transport, even if resuspension is the dominant mechanism in most cases.

Offshore Particle Dynamics

Offshore stations had different particle dynamics because they were farther away from glaciers and large river drainages. Prince of Wales, Chatham Strait, Cross-Gyre, and P16N all had particle concentrations on a scale an order of magnitude lower than the stations to the north (Figures 2.3, 2.10). These lower particle concentrations coincide with lack of major fluvial and glacial input, since no major rivers drain Kodiak Island in the western gulf (Hampton et al., 1987) and P16N stations reflect this lack of riverine particle input. The rivers flowing into the southeastern gulf near Sitka have smaller total discharge and drain fewer, smaller glaciers than their northern counterparts (Neal et al., 2010). In one study of southeast Alaska's inlets, the most southern entrances at Prince of Wales and Chatham Strait had deeper Secchi depths and higher salinities than the northern entrances near Glacier Bay and Cross Sound, which they called

"iceberg inlets" (Pickard, 1967). Areas in close proximity to glacial and fluvial inputs were dominated by smaller particle size classes in 2015. However, offshore, where particle size is larger, particularly within the uppermost 1000 m, biological processes drive particle concentrations and size patterns instead of being overwhelmed by resuspended shelf sediments and terrigenous inputs. Production and grazing at the surface, coagulation, and zooplankton interactions in deeper water drive particle dynamics in these offshore environments (Figure 2.12).

Biogeochemical Implications

Organic carbon flux is known to be quantitatively associated with the flux of inorganic ballast minerals. Unballasted particles are more quickly remineralized at shallower depths (Armstrong et al., 2001). Calcium carbonate is the most dense ballast mineral and most widespread in the global oceans, but lithogenic particles are still more dense than the silicate skeletons of diatoms (Klaas and Archer, 2002), thus can increase the density of organic particles upon aggregation where lithogenic inputs are abundant (Ittekkot, 1993). The aggregation of clays with phytoplankton cells may either increase or decrease sinking rates (Passow, 2004), but it has been shown that marine snow particles collect small lithogenic particles as they sink through the water column, which increases their density overall (Hamm, 2002). Although many studies have approached the phenomenon of atmospherically-deposited dust as lithogenic ballast for marine particles (Bressac et al., 2014; Ginoux et al., 2001; Moore and Braucher, 2008), very few have studied the impact of riverine lithogenic ballast on marine particles. One study in the Arabian Sea found that the timing of maximum particle concentrations coincided with the timing of both the maximum atmospheric dust deposition and the maximum river discharge from the

Ganges and Brahmaputra (Ittekkot et al., 1992). Dunne et al. (2007) argued that excluding the role of lithogenics in global models underestimated POC flux to the deep seafloor by up to 51%, and that riverine and erosional sources accounted for the majority of the lithogenic particle flux. Based on their sheer quantities, the glacial till particles and other suspended lithogenic particles detected by the UVP enhance sinking rates of organic matter in the GOA.

The spatial distribution of inorganic particles sourced from land and the continental margin also has serious implications for the transport of particulate iron offshore. Past studies in the subarctic Pacific have summarized sources of particulate iron from land, including resuspended shelf sediments of continental origin (Lam and Bishop, 2008; Lam et al., 2006), eddies transporting nearshore waters into the offshore (Lippiatt et al., 2010), and dust plumes from large uncovered braided rivers (Crusius et al., 2011). Ultimately, the source of much of the reactive iron in the GOA is glacial flour and glacially-derived sediments (Schroth et al., 2014, 2011), particularly in the summer season (Aguilar-Islas et al., 2015). Because the particulate fraction is an important contributor to reactive iron in this region, understanding the mechanisms and magnitude of particle transport is crucial to our knowledge of iron availability to primary producers. Data collected with the UVP suggest that although particles associated with river discharge are major inputs, resuspended shelf sediments and advection of sediments from the shelf break may be a larger contributor to offshore transport than the coastal-trapped river plumes (Table 2.2). In addition to shelf benthic boundary layers, slope and deep sea nepheloid layers could also impact iron transport. Horner et al. (2015) found that most of the iron in sediment cores in the Pacific is sourced from deep sea sediments and hydrothermal vents. The nepheloid layers found at deep, offshore stations in this study (Figure 2.11 A) could be one example mechanism for that deep-sea transport.

Finally, these results highlight the important role of continental margins in ocean carbon cycling. Carbon flux on the continental shelf and slope has been observed to be ten times that in the deep sea at similar depths (Walsh, 1991), and it is estimated that over 40% of all ocean carbon sequestration occurs in the waters over shelves and slopes (<2000 m depths) (Muller-Karger et al., 2005). Enhanced primary production in coastal areas, combined with shallower depths that provide less time for remineralization during export, causes the majority of organic carbon burial to occur on continental shelves and slopes (Premuzic et al., 1982). More specifically, Wollast (1998) estimated that over the shelf, carbon export and burial together equal 40% of the carbon created by primary production, while over the slope and open ocean this portion decreases to 20% and 15%, respectively. In addition to storage within sediments, particulate carbon from the shelf can be transported offshore to deep waters in what has been termed the "continental shelf pump" (Tsunogai et al., 1999). In the GOA, a known carbon sink of 14-34 Tg carbon per year (Evans and Mathis, 2013), our study shows that the large quantities of suspended material over the shelf could enhance the storage of carbon through the ballasting effects of lithogenic particles and through the transport of suspended material from the shelf break offshore.

Conclusions

Higher particle concentrations were found closer to shore and closer to fluvial and glacial inputs, decreasing with distance from rivers, glaciers, and land. Rivers carrying runoff from land and glaciers influence the northern central GOA coast much more than the southeastern and western areas, which lack the major rivers and glaciated icefields of the northern regions. Offshore stations showed lower total particle concentrations and large particles were

proportionally more abundant than over the shelf. Nearshore, drivers of high particle

concentration include fluvial and glacial inputs from land, resuspension and transport of bottom

sediments. This dominance of inorganic material nearshore has implications for the ballasting of

sinking particles, and has the potential to increase the flux of sinking particles in this region.

Furthermore, the magnitude of the physical transport of the predominantly lithogenic material

has implications for the availability of reactive iron to primary producers in the iron-limited

offshore environment.

Future directions should include particle collection methods such as drifting or moored

sediment traps, to determine particulate matter carbon content and to compare with UVP-

collected particle data for a better constrained estimate of carbon fluxes. This information can

inform other studies of the biological pump in high-latitude, glaciated regions. Studies interested

in purely biological particle dynamics should deploy sediment traps offshore of the shelf break in

the GOA, where the particles of interest are not overwhelmed in concentration by glacial runoff

and resuspended shelf sediments.

References

Aguilar-Islas, A.M., Séguret, M.J.M., Rember, R., Buck, K.N., Proctor, P., Mordy, C.W., Kachel, N.B., 2015. Temporal variability of reactive iron over the Gulf of Alaska shelf. Deep Sea Res. Part II Top. Stud. Oceanogr. 1–17. doi:10.1016/j.dsr2.2015.05.004

Arístegui, J., Gasol, J.M., Duarte, C.M., Herndl, G.J., 2009. Microbial oceanography of the dark ocean's pelagic realm. Limnol. Oceanogr. 54, 1501–1529. doi:10.4319/lo.2009.54.5.1501

Armstrong, R., Lee, C., Hedges, J.I., Honjo, S., Wakeham, S.G., 2001. A new, mechanistic model for organic carbon fluxes in the ocean based on the quantitative association of POC with ballast minerals. Deep Sea Res. Part II Top. Stud. Oceanogr. 49, 219–236. doi:10.1016/S0967-0645(01)00101-1

Baltar, F., Arístegui, J., Gasol, J.M., Sintes, E., Herndl, G.J., 2009. Evidence for dependence of prokaryotic metabolism on suspended particulate organic matter in the dark waters of the subtropical North Atlantic. Limnol. Oceanogr. 54, 182–193.

Baltar, F., Arístegui, J., Sintes, E., Gasol, J.M., Reinthaler, T., Herndl, G.J., 2010. Significance of non-sinking particulate organic carbon and dark CO_2 fixation to heterotrophic carbon demand in the mesopelagic northeast Atlantic. Geophys. Res. Lett. 37. doi:10.1029/2010GL043105

Bartsch-Winkler, S., Ovenshine, A.T., 1984. Macrotidal Subarctic Environment of Turnagain and Knik Arms, Upper Cook Inlet, Alaska: Sedimentology of the Intertidal Zone. J. Sediment. Petrol. 54, 1221–1238.

Bishop, J.K.B., Lam, P.J., Wood, T.J., 2012. Getting good particles: Accurate sampling of particles by large volume *in situ* filtration. Limnol. Oceanogr. Methods 10, 681–710. doi:10.4319/lom.2012.10.681

Bishop, K.B., James, J., Calvert, E., Steven, S., Soon, M., 1999. Spatial and temporal variability of POC in the northeast subarctic Pacific. Deep. Res. Part II Top. Stud. Oceanogr. 46, 2699–2733. doi:10.1016/S0967-0645(99)00081-8

Boss, E., Guidi, L., Richardson, M.J., Stemmann, L., Gardner, W., Bishop, J.K.B., Anderson, R.F., Sherrell, R.M., 2015. Optical techniques for remote and *in situ* characterization of particles pertinent to GEOTRACES. Prog. Oceanogr. 133, 43–54. doi:10.1016/j.pocean.2014.09.007

Boss, E., Slade, W.H., Behrenfeld, M., Dall'Olmo, G., 2009. Acceptance angle effects on the beam attenuation in the ocean. Opt. Express 17, 1535–1550.

Bressac, M., Guieu, C., Doxaran, D., Bourrin, F., Desboeufs, K., Leblond, N., Ridame, C., 2014. Quantification of the lithogenic carbon pump following a simulated dust-deposition event in large mesocosms. Biogeosciences 11, 1007–1020. doi:10.5194/bg-11-1007-2014

Broecker, W.S., 1982. Ocean chemistry during glacial time. Geochim. Cosmochim. Acta 47, 1539–1540. doi:10.1016/0016-7037(83)90315-0

Brown, M.T., Lippiatt, S.M., Bruland, K.W., 2010. Dissolved aluminum, particulate aluminum, and silicic acid in northern Gulf of Alaska coastal waters: Glacial/riverine inputs and extreme reactivity. Mar. Chem. 122, 160–175. doi:10.1016/j.marchem.2010.04.002

Buesseler, K.O., Antia, A.N., Chen, M., Fowler, S.W., Gardner, W.D., Gustafsson, O., Harada, K., Michaels, A.F., Rutgers van der Loeff, M., Sarin, M., Steinberg, D.K., Trull, T., 2007. An assessment of the use of sediment traps for estimating upper ocean particle fluxes. J. Mar. Res. 65, 345–416. doi:10.1357/002224007781567621

Buesseler, K.O., Bacon, M.P., Kirk Cochran, J., Livingston, H.D., 1992. Carbon and nitrogen export during the JGOFS North Atlantic Bloom experiment estimated from ^{234}Th: ^{238}U disequilibria. Deep Sea Res. Part A. Oceanogr. Res. Pap. 39, 1115–1137. doi:10.1016/0198-0149(92)90060-7

Burbank, D.C., 1974. Suspended Sediment Transport and Deposition in Alaskan Coastal Waters. University of Alaska Fairbanks. M.S. Thesis.

Burd, A.B., Hansell, D.A., Steinberg, D.K., Anderson, T.R., Arístegui, J., Baltar, F., Beaupré, S.R., Buesseler, K.O., DeHairs, F., Jackson, G.A., Kadko, D.C., Koppelmann, R., Lampitt, R.S., Nagata, T., Reinthaler, T., Robinson, C., Robison, B.H., Tamburini, C., Tanaka, T., 2010. Assessing the apparent imbalance between geochemical and biochemical indicators of meso- and bathypelagic biological activity: What the @$#! is wrong with present calculations of carbon budgets? Deep Sea Res. Part II Top. Stud. Oceanogr. 57, 1557–1571. doi:10.1016/j.dsr2.2010.02.022

Burd, A.B., Jackson, G., 2009. Particle Aggregation. Ann. Rev. Mar. Sci. 1, 65–90. doi:10.1146/annurev.marine.010908.163904

Burd, A.B., Jackson, G., Moran, S.B., 2007. The role of the particle size spectrum in estimating POC fluxes from disequilibrium. Deep Sea Res. Part I Oceanogr. Res. Pap. 54, 897–918. doi:10.1016/j.dsr.2007.03.006

Carlson, P.R., Bruns, T.R., Molnia, B.F., Schwab, W.C., 1982. Submarine valleys in the Northeastern Gulf of Alaska: Characteristics and Probable Origin. Mar. Geol. 47, 217–242.

Carlson, P.R., Molnia, B.F., 1978. Minisparker profiles and sedimentological data from RV Acona cruise in the Gulf of Alaska and Prince William Sound. USGS Open File Rep. 78-381. 32 pp.

Carmack, E., Winsor, P., Williams, W., 2015. The contiguous panarctic Riverine Coastal Domain: A unifying concept. Prog. Oceanogr. doi:10.1016/j.pocean.2015.07.014

Coyle, K.O., Pinchuk, A.I., 2005. Seasonal cross-shelf distribution of major zooplankton taxa on the northern Gulf of Alaska shelf relative to water mass properties, species depth preferences and vertical migration behavior. Deep Sea Res. Part II Top. Stud. Oceanogr. 52, 217–245. doi:10.1016/j.dsr2.2004.09.025

Coyle, K.O., Pinchuk, A.I., 2003. Annual cycle of zooplankton abundance, biomass and production on the northern Gulf of Alaska shelf, October 1997 through October 2000. Fish. Oceanogr. 12, 327–338. doi:10.1046/j.1365-2419.2003.00256.x

Crusius, J., Schroth, A.W., Gassó, S., Moy, C.M., Levy, R.C., Gatica, M., 2011. Glacial flour dust storms in the Gulf of Alaska: Hydrologic and meteorological controls and their importance as a source of bioavailable iron. Geophys. Res. Lett. 38, 1–5. doi:10.1029/2010GL046573

Dall'Olmo, G., Mork, K.A., 2014. Carbon export by small particles in the Norwegian Sea. Geophys. Res. Lett. 41, 2921–2927. doi:10.1002/2014GL059244

Dunne, J.P., Sarmiento, J.L., Gnanadesikan, A., 2007. A synthesis of global particle export from the surface ocean and cycling through the ocean interior and on the seafloor. Global Biogeochem. Cycles 21, 1–16. doi:10.1029/2006GB002907

Durkin, C.A., Estapa, M.L., Buesseler, K.O., 2015. Observations of carbon export by small sinking particles in the upper mesopelagic. Mar. Chem. 175, 72–81. doi:10.1016/j.marchem.2015.02.011

Ebersbach, F., Trull, T.W., 2008. Sinking particle properties from polyacrylamide gels during the Kerguelen Ocean and Plateau compared Study (KEOPS): Zooplankton control of carbon export in an area of persistent natural iron inputs in the Southern Ocean. Limnol. Oceanogr. 53, 212–224. doi:10.4319/lo.2008.53.1.0212

Evans, W., Mathis, J.T., 2013. The Gulf of Alaska coastal ocean as an atmospheric CO_2 sink. Cont. Shelf Res. 65, 52–63. doi:10.1016/j.csr.2013.06.013

Feely, R., Baker, E.T., Schumacher, J.D., Massoth, G.J., Landing, W.M., 1979. Processes affecting the distribution and transport of suspended matter in the northeast Gulf of Alaska. Deep Sea Res. 26, 445–464.

Feely, R., Massoth, G.J., Landing, W.M., 1981. Major- and trace-element composition of suspended matter in the north-east Gulf of Alaska: Relationships with major sources. Mar. Chem. 10, 431–453. doi:10.1016/0304-4203(81)90020-7

Forest, A., Babin, M., Stemmann, L., Picheral, M., Sampei, M., Fortier, L., Gratton, Y., Bélanger, S., Devred, E., Sahlin, J., Doxaran, D., Joux, F., Ortega-Retuerta, E., Martín, J., Jeffrey, W.H., Gasser, B., Carlos Miquel, J., 2013. Ecosystem function and particle flux dynamics across the Mackenzie Shelf (Beaufort Sea, Arctic Ocean): an integrative analysis of spatial variability and biophysical forcings. Biogeosciences 10, 2833–2866. doi:10.5194/bg-10-2833-2013

Forest, A., Stemmann, L., Picheral, M., Burdorf, L., Robert, D., Fortier, L., Babin, M., 2012. Size distribution of particles and zooplankton across the shelf-basin system in southeast Beaufort Sea: combined results from an Underwater Vision Profiler and vertical net tows. Biogeosciences 9, 1301–1320. doi:10.5194/bg-9-1301-2012

Fowler, S.W., Knauer, G., 1986. Role of large particles in the transport of elements and organic compounds through the oceanic water column. Prog. Oceanogr. 16, 147–194. doi:10.1016/0079-6611(86)90032-7

Ginoux, P., Chin, M., Tegen, I., Prospero, J.M., Holben, B., Dubovik, O., Lin, S.-J., 2001. Sources and distributions of dust aerosols simulated with the GOCART model. J. Geophys. Res. 106, 20255–20273. doi:10.1029/2000JD000053

Grebmeier, J., McRoy, C., Feder, H., 1988. Pelagic-benthic coupling on the shelf of the northern Bering and Chukchi Seas. I. Food supply source and benthic bio-mass. Mar. Ecol. Prog. Ser. 48, 57–67. doi:10.3354/meps048057

Guidi, L., Calil, P.H.R., Duhamel, S., Björkman, K.M., Doney, S.C., Jackson, G., Li, B., Church, M.J., Tozzi, S., Kolber, Z.S., Richards, K.J., Fong, A., Letelier, R.M., Gorsky, G., Stemmann, L., Karl, D.M., 2012. Does eddy-eddy interaction control surface phytoplankton distribution and carbon export in the North Pacific Subtropical Gyre? J. Geophys. Res. 117, G02024. doi:10.1029/2012JG001984

Guidi, L., Gorsky, G., Claustre, H., Miquel, J.C., Picheral, M., Stemmann, L., 2008a. Distribution and fluxes of aggregates >100 μm in the upper kilometer of the South-Eastern Pacific. Biogeosciences 5, 1361–1372. doi:10.5194/bg-5-1361-2008

Guidi, L., Jackson, G., Stemmann, L., Miquel, J.C., Picheral, M., Gorsky, G., 2008b. Relationship between particle size distribution and flux in the mesopelagic zone. Deep Sea Res. Part I Oceanogr. Res. Pap. 55, 1364–1374. doi:10.1016/j.dsr.2008.05.014

Guidi, L., Stemmann, L., Jackson, G., Ibanez, F., Claustre, H., Legendre, L., Picheral, M., Gorsky, G., 2009. Effects of phytoplankton community on production, size, and export of large aggregates: A world-ocean analysis. Limnol. Oceanogr. 54, 1951–1963. doi:10.4319/lo.2009.54.6.1951

Hamm, C.E., 2002. Interactive aggregation and sedimentation of diatoms and clay-sized lithogenic material. Limnol. Oceanogr. 47, 1790–1795. doi:10.4319/lo.2002.47.6.1790

Hampton, M., Carlson, P., Lee, H., Feely, R., 1987. Geomorphology, sediment, and sedimentary processes, in: Hood, D.W., Zimmerman, S. (Eds.), The Gulf of Alaska, Physical Environment and Biological Resources. US Department of Commerce. US Government Printing Office, Washington, DC, pp. 93–144.

Hedges, J.I., Keil, R.G., 1995. Sedimentary organic matter preservation: an assessment and speculative synthesis. Mar. Chem. 49, 137–139. doi:10.1016/0304-4203(95)00013-H

Horner, T.J., Williams, H.M., Hein, J.R., Saito, M.A., Burton, K.W., Halliday, A.N., Nielsen, S.G., 2015. Persistence of deeply sourced iron in the Pacific Ocean. Proc. Natl. Acad. Sci. 112, 1292–1297. doi:10.1073/pnas.1420188112

Ittekkot, V., 1993. The abiotically driven biological pump in the ocean and short-term fluctuations in atmospheric CO_2 contents. Glob. Planet. Change 8, 17–25. doi:10.1016/0921-8181(93)90060-2

Ittekkot, V., Haake, B., Bartsch, M., Nair, R.R., Ramaswamy, V., 1992. Organic carbon removal in the sea: the continental connection, in: Summerhays, C.P., Prell, W.L., Emeis, K.C. (Eds.), Upwelling Systems: Evolution Since the Early Miocene. pp. 167–176.

Jouandet, M.-P., Jackson, G., Carlotti, F., Picheral, M., Stemmann, L., Blain, S., 2014. Rapid formation of large aggregates during the spring bloom of Kerguelen Island: observations and model comparisons. Biogeosciences 11, 4393–4406. doi:10.5194/bg-11-4393-2014

Karp-Boss, L., Azavedo, L., Boss, E., 2007. LISST-100 measurements of phytoplankton size distribution: evaluation of the effects of cell shape. Limnol. Oceanogr. Methods 5, 396–406. doi:10.4319/lom.2007.5.396

Klaas, C., Archer, D.E., 2002. Association of sinking organic matter with various types of mineral ballast in the deep sea: Implications for the rain ratio. Global Biogeochem. Cycles 16, 1–14. doi:10.1029/2001GB001765

Krumbein, W., Aberdeen, E., 1937. The sediments of Barataria Bay. J. Sediment. Petrol. 7, 3–17.

Krumbein, W.C., Pettijohn, F.J., 1938. Manual of sedimentary petrography. Appleton-Century-Crofts, New York.

Ladd, C., Stabeno, P., Cokelet, E.D., 2005. A note on cross-shelf exchange in the northern Gulf of Alaska. Deep Sea Res. Part II Top. Stud. Oceanogr. 52, 667–679. doi:10.1016/j.dsr2.2004.12.022

Lam, P.J., Bishop, J.K.B., 2008. The continental margin is a key source of iron to the HNLC North Pacific Ocean. Geophys. Res. Lett. 35, 1–5. doi:10.1029/2008GL033294

Lam, P.J., Bishop, J.K.B., Henning, C.C., Marcus, M.A., Waychunas, G.A., Fung, I.Y., 2006. Wintertime phytoplankton bloom in the subarctic Pacific supported by continental margin iron. Global Biogeochem. Cycles 20, 1–12. doi:10.1029/2005GB002557

Lampitt, R.S., Wishner, K.F., Turley, C.M., Angel, M.V., 1993. Marine snow studies in the Northeast Atlantic Ocean: distribution, composition and role as a food source for migrating plankton. Mar. Biol. 116, 689–702. doi:10.1007/BF00355486

Lippiatt, S.M., Lohan, M.C., Bruland, K.W., 2010. The distribution of reactive iron in northern

    Gulf of Alaska coastal waters. Mar. Chem. 121, 187–199.

    doi:10.1016/j.marchem.2010.04.007

Martin, J.H., Gordon, R.M., 1988. Northeast Pacific iron distributions in relation to

    phytoplankton productivity. Deep Sea Res. 35, 177–196.

Martin, J.H., Gordon, R.M., Fitzwater, S., Broenkow, W.W., 1989. Vertex: phytoplankton/iron

    studies in the Gulf of Alaska. Deep Sea Res. Part A. Oceanogr. Res. Pap. 36, 649–680.

    doi:10.1016/0198-0149(89)90144-1

McCave, I.N., 1975. Vertical flux of particles in the ocean. Deep Sea Res. Oceanogr. Abstr. 22,

    491–502. doi:10.1016/0011-7471(75)90022-4

McDonnell, A.M.P., Buesseler, K.O., 2012. A new method for the estimation of sinking particle

    fluxes from measurements of the particle size distribution, average sinking velocity, and

    carbon content. Limnol. Oceanogr. Methods 10, 329–346. doi:10.4319/lom.2012.10.329

McDonnell, A.M.P., Lam, P.J., Lamborg, C.H., Buesseler, K.O., Sanders, R., Riley, J.S.,

    Marsay, C., Smith, H.E.K., Sargent, E.C., Lampitt, R.S., Bishop, J.K.B., 2015. The

    oceanographic toolbox for the collection of sinking and suspended marine particles. Prog.

    Oceanogr. 133, 17–31. doi:10.1016/j.pocean.2015.01.007

Milliman, J.D., Syvitski, J.P.M., 1992. Geomorphic/tectonic control of sediment discharge to the

    ocean: the importance of small mountainous rivers. J. Geol. 100, 525–544.

    doi:10.1086/629606

Molnia, B.F., 2008. Glaciers of North America - Glaciers of Alaska, in: Williams, R.S., Ferrigno,

    J.G. (Eds.), Satellite Image Atlas of Glaciers of the World. USGS Professional Paper 1386-

    K, p. 525.

Moore, J.K., Braucher, O., 2008. Sedimentary and mineral dust sources of dissolved iron to the world ocean. Biogeosciences 5, 631–656.

Muench, R., Schumacher, J., 1980. Physical oceanographic and meteorological conditions in the northwest Gulf of Alaska. NOA Technical Memorandum ERL PMEL-22, Seattle, WA.

Muller-Karger, F.E., Varela, R., Thunell, R., Luerssen, R., Hu, C., Walsh, J.J., 2005. The importance of continental margins in the global carbon cycle. Geophys. Res. Lett. 32, 1–4. doi:10.1029/2004GL021346

Napp, J.M., 1996. The plankton of Shelikof Strait, Alaska: Standing stock, production, mesoscale variability and their relevance to larval fish survival. Fish. Oceanogr. 5, 19–38. doi:10.1111/j.1365-2419.1996.tb00080.x

Neal, E.G., Hood, E., Smikrud, K., 2010. Contribution of glacier runoff to freshwater discharge into the Gulf of Alaska. Geophys. Res. Lett. 37, 1–5. doi:10.1029/2010GL042385

Ohman, M.D., Powell, J.R., Picheral, M., Jensen, D.W., 2012. Mesozooplankton and particulate matter responses to a deep-water frontal system in the southern California Current System. J. Plankton Res. 34, 815–827. doi:10.1093/plankt/fbs028

Passow, U., 2004. Switching perspectives: Do mineral fluxes determine particulate organic carbon fluxes or vice versa? Geochemistry, Geophys. Geosystems 5, n/a–n/a. doi:10.1029/2003GC000670

Picheral, M., Guidi, L., Stemmann, L., Karl, D.M., Iddaoud, G., Gorsky, G., 2010. The Underwater Vision Profiler 5: An advanced instrument for high spatial resolution studies of particle size spectra and zooplankton. Limnol. Oceanogr. Methods 8, 462–473. doi:10.4319/lom.2010.8.462

Pickard, G., 1967. Some oceanographic characteristics of the larger inlets of Southeast Alaska. J. Fish. Board Canada 24, 1475–1506. doi:10.1139/f67-123

Powell, R.D., Molnia, B.F., 1989. Glacimarine sedimentary processes, facies and morphology of the south-southeast Alaska shelf and fjords. Mar. Geol. 85, 359–390. doi:10.1016/0025-3227(89)90160-6

Premuzic, E.T., Benkovitz, C.M., Gaffney, J.S., Walsh, J.J., 1982. The nature and distribution of organic matter in the surface sediments of world oceans and seas. Org. Geochem. 4, 63–77. doi:10.1016/0146-6380(82)90009-2

Reed, R., 1984. Flow of the Alaskan Stream and its variations. Deep Sea Res. Part A. Oceanogr. Res. Pap. 31, 369–386. doi:10.1016/0198-0149(84)90090-6

Richardson, T.L., Jackson, G.A., 2007. Small phytoplankton and carbon export from the surface ocean. Science 315, 838–840. doi:10.1126/science.1133471

Riley, J.S., Sanders, R., Marsay, C., Le Moigne, F.C., Achterberg, E.P., Poulton, J., 2012. The relative contribution of fast and slow sinking particles to ocean carbon export. Global Biogeochem. Cycles 26, 1–10. doi:10.1029/2011GB004085

Roullier, F., Berline, L., Guidi, L., Durrieu De Madron, X., Picheral, M., Sciandra, A., Pesant, S., Stemmann, L., 2014. Particle size distribution and estimated carbon flux across the Arabian Sea oxygen minimum zone. Biogeosciences 11, 4541–4557. doi:10.5194/bg-11-4541-2014

Royer, T.C., 1982. Coastal fresh water discharge in the northeast Pacific. J. Geophys. Res. 87, 2017–2021.

Royer, T.C., 1975. Seasonal variations of waters in the northern Gulf of Alaska. Deep Sea Res. 22, 403–416.

Sambrotto, R.N., Lorenzen, C., 1987. Phytoplankton and primary production, in: Hood, D.W.,

    Zimmerman, S.T. (Eds.), The Gulf of Alaska, Physical Environment and Biological

    Resources. NOAA, US Government Printing Office, Washington, DC, pp. 249–282.

Schroth, A.W., Crusius, J., Chever, F., Bostick, B.C., Rouxel, O.J., 2011. Glacial influence on

    the geochemistry of riverine iron fluxes to the Gulf of Alaska and effects of deglaciation.

    Geophys. Res. Lett. 38. doi:10.1029/2011GL048367

Schroth, A.W., Crusius, J., Hoyer, I., Campbell, R., 2014. Estuarine removal of glacial iron and

    implications for iron fluxes to the ocean. Geophys. Res. Lett. 41, 3951–3958.

    doi:10.1002/2013GL058772

Siegenthaler, U., Wenk, T., 1984. Rapid atmospheric CO_2 variations and ocean circulation.

    Nature 308, 624–626. doi:10.1038/308624a0

Silver, M.W., 1978. Marine snow: microplankton habitat and source of small-scale patchiness in

    pelagic populations. Science 201, 371–373.

Stabeno, P.., Bond, N.., Hermann, A.., Kachel, N.., Mordy, C.., Overland, J.., 2004. Meteorology

    and oceanography of the Northern Gulf of Alaska. Cont. Shelf Res. 24, 859–897.

    doi:10.1016/j.csr.2004.02.007

Stemmann, L., Eloire, D., Sciandra, A., Jackson, G., Guidi, L., Picheral, M., Gorsky, G., 2008.

    Volume distribution for particles between 3.5 to 2000 μm in the upper 200 m region of the

    South Pacific Gyre. Biogeosciences Discuss. 5, 299–310. doi:10.5194/bgd-4-3377-2007

Stemmann, L., Jackson, G.A., Gorsky, G., 2004. A vertical model of particle size distributions

    and fluxes in the midwater column that includes biological and physical processes—Part II:

    application to a three year survey in the NW Mediterranean Sea. Deep Sea Res. Part I

    Oceanogr. Res. Pap. 51, 885–908. doi:10.1016/j.dsr.2004.03.002

Tsunogai, S., Watanabe, S., Sato, T., 1999. Is there a "continental shelf pump" for the absorption of atmospheric CO_2? Tellus 51, 701–712. doi:10.1034/j.1600-0889.1999.t01-2-00010.x

Verdugo, P., Alldredge, A.L., Azam, F., Kirchman, D.L., Passow, U., Santschi, P.H., 2004. The oceanic gel phase: a bridge in the DOM–POM continuum. Mar. Chem. 92, 67–85. doi:10.1016/j.marchem.2004.06.017

Volk, T., Hoffert, M.I., 1985. Ocean carbon pumps: analysis of relative strengths and efficiencies in ocean-drive atmospheric CO_2 changes. Geophys. Monogr. Ser. 32, 99–110.

Walsh, I.D., Gardner, W.D., 1992. A comparison of aggregate profiles with sediment trap fluxes. Deep Sea Res. Part A. Oceanogr. Res. Pap. 39, 1817–1834. doi:10.1016/0198-0149(92)90001-A

Walsh, J.J., 1991. Importance of continental margins in the marine biogeochemical cycling of carbon and nitrogen. Nature 350, 53–55. doi:10.1038/350053a0

Weingartner, T., Eisner, L., Eckert, G.L., Danielson, S., 2009. Southeast Alaska: oceanographic habitats and linkages. J. Biogeogr. 36, 387–400. doi:10.1111/j.1365-2699.2008.01994.x

Wheatcroft, R., Goñi, M., Hatten, J., Pasternack, G.B., Warrick, J., 2010. The role of effective discharge in the ocean delivery of particulate organic carbon by small, mountainous river systems. Limnol. Oceanogr. 55, 161–171. doi:10.4319/lo.2010.55.1.0161

Wollast, R., 1998. Evaluation and comparison of the global carbon cycle in the coastal zone and in the open ocean, in: Brink, K.H., Robinson, A.R. (Eds.), The Sea. John Wiley & Sons, Inc., pp. 213–252.

Wu, J., Aguilar-Islas, A., Rember, R., Weingartner, T., Danielson, S., Whitledge, T., 2009. Size-fractionated iron distribution on the northern Gulf of Alaska. Geophys. Res. Lett. 36, L11606. doi:10.1029/2009GL038304

Conclusions

The UVP as an oceanographic tool has many advantages and disadvantages, and leaves some research questions yet unanswered in the Gulf of Alaska. The UVP has the innovative ability to count and size a wide range of size classes *in situ* while recording the depth at which each particle was found, and as an added feature can create photographs of the largest objects for identification and sorting. The UVP can image detrital particles and gelatinous zooplankton whose fragile structures do not allow for physical collection with traditional methods. The combination of a fine resolution and a large sampling volume sets this instrument apart from other optical imaging devices (Boss et al., 2015; Picheral et al., 2010). However, this instrument lacks the ability to physically collect particles and determine their composition. It does not allow for identification of particle types or zooplankton organisms smaller than 500 μm. In the Gulf of Alaska, this made it difficult to distinguish the small (60-500 μm) phytoplankton and zooplankton from the inorganic, lithogenic particles in nearshore regions of elevated particle concentration.

In 2014 and 2015, the Gulf of Alaska was characterized by high particle concentrations dominated by small size classes over the shelf, especially close to inputs of freshwater and glacial runoff, and low particle concentrations with a greater presence of large particles in the offshore environments. Results suggest that resuspension of shelf sediments in benthic boundary layers is a major driver of the spatial distribution of particles. These finding have major implications for enhanced carbon flux to depth due to the ballasting effect of lithogenic particles, offshore transport of particulate phase iron, and the role of continental margin particle fluxes in global carbon cycling.

This study is only the first step of many possibilities for the research of particle dynamics in the Gulf of Alaska. The particle concentrations mapped in this study have already helped to plan the most advantageous location for a sediment trap mooring near the shelf break on the Seward Line, which was deployed in September 2015. A logical next step is to deploy sediment traps or *in situ* pumps alongside the UVP, to measure the composition of the particles counted and sized by the UVP. With a combination of sediment trap, *in situ* pump, and UVP data, an empirical relationship could be fit between UVP particle size distributions and sediment trap size distributions to create a model for the Gulf of Alaska. This model could then be used to estimate particle flux from UVP data alone (as per Guidi et al., 2008b). Furthermore, the extreme inputs of sediments from riverine and glacial runoff would make the Gulf of Alaska an ideal location for a more elaborate physical model for the transport of suspended particles. In light of global climate change, the melting of Alaskan glaciers could impact the magnitude of sediment inputs and the compositions of lithogenic particles entering the marine system. This high-latitude, iron-limited, biologically productive region is a complicated system, in which it is crucial to study the sources, distributions, and drivers of marine particles in the future.

References

Abramson, L., Lee, C., Liu, Z., Wakeham, S., Szlosek, J., 2010. Exchange between suspended and sinking particles in the northwest Mediterranean as inferred from the organic composition of *in situ* pump and sediment trap samples. Limnol. Oceanogr. 55, 725–739. doi:10.4319/lo.2009.55.2.0725

Alldredge, A.L., Gotschalk, C., 1988. *In situ* settling behavior of marine snow. Limnol. Oceanogr. 33, 339–351. doi:10.4319/lo.1988.33.3.0339

Alldredge, A.L., Granata, T.C., Gotschalk, C.C., Dickey, T.D., 1990. The physical strength of marine snow and its implications for particle disaggregation in the ocean. Limnol. Oceanogr. 35, 1415–1428. doi:10.4319/lo.1990.35.7.1415

Alpine, A.E., Cloern, J.E., 1985. Differences in in vivo fluorescence yield between three phytoplankton size classes. J. Plankton Res. 7, 381–390. doi:10.1093/plankt/7.3.381

Arístegui, J., Gasol, J.M., Duarte, C.M., Herndl, G.J., 2009. Microbial oceanography of the dark ocean's pelagic realm. Limnol. Oceanogr. 54, 1501–1529. doi:10.4319/lo.2009.54.5.1501

Armstrong, R., Lee, C., Hedges, J.I., Honjo, S., Wakeham, S.G., 2001. A new, mechanistic model for organic carbon fluxes in the ocean based on the quantitative association of POC with ballast minerals. Deep Sea Res. Part II Top. Stud. Oceanogr. 49, 219–236. doi:10.1016/S0967-0645(01)00101-1

Baltar, F., Arístegui, J., Gasol, J.M., Sintes, E., Herndl, G.J., 2009. Evidence for dependence of prokaryotic metabolism on suspended particulate organic matter in the dark waters of the subtropical North Atlantic. Limnol. Oceanogr. 54, 182–193.

Baltar, F., Arístegui, J., Sintes, E., Gasol, J.M., Reinthaler, T., Herndl, G.J., 2010. Significance of non-sinking particulate organic carbon and dark CO_2 fixation to heterotrophic carbon demand in the mesopelagic northeast Atlantic. Geophys. Res. Lett. 37. doi:10.1029/2010GL043105

Bishop, J.K.B., Lam, P.J., Wood, T.J., 2012. Getting good particles: Accurate sampling of particles by large volume *in situ* filtration. Limnol. Oceanogr. Methods 10, 681–710. doi:10.4319/lom.2012.10.681

Bishop, J.K.B., Stepien, J.C., Wiebe, P.H., 1986. Particulate matter distributions, chemistry and flux in the Panama Basin: response to environment forcing. Prog. Oceanogr. 17, 1–59. doi:http://dx.doi.org/10.1016/0079-6611(86)90024-8

Boss, E., Guidi, L., Richardson, M.J., Stemmann, L., Gardner, W., Bishop, J.K.B., Anderson, R.F., Sherrell, R.M., 2015. Optical techniques for remote and *in situ* characterization of particles pertinent to GEOTRACES. Prog. Oceanogr. 133, 43–54. doi:10.1016/j.pocean.2014.09.007

Boss, E., Slade, W.H., Behrenfeld, M., Dall'Olmo, G., 2009. Acceptance angle effects on the beam attenuation in the ocean. Opt. Express 17, 1535–1550.

Boyd, P.W., Strzepek, R., Takeda, S., Jackson, G., Wong, C.S., McKay, R.M., Law, C., Kiyosawa, H., Saito, H., Sherry, N., 2005. The evolution and termination of an iron-induced mesoscale bloom in the northeast subarctic Pacific. Limnol. Oceanogr. 50, 1872–1886. doi:10.4319/lo.2005.50.6.1872

Broecker, W.S., 1982. Ocean chemistry during glacial time. Geochim. Cosmochim. Acta 47, 1539–1540. doi:10.1016/0016-7037(83)90315-0

Buesseler, K.O., Antia, A.N., Chen, M., Fowler, S.W., Gardner, W.D., Gustafsson, O., Harada, K., Michaels, A.F., Rutgers van der Loeff, M., Sarin, M., Steinberg, D.K., Trull, T., 2007. An assessment of the use of sediment traps for estimating upper ocean particle fluxes. J. Mar. Res. 65, 345–416. doi:10.1357/002224007781567621

Buesseler, K.O., Bacon, M.P., Kirk Cochran, J., Livingston, H.D., 1992. Carbon and nitrogen export during the JGOFS North Atlantic Bloom experiment estimated from ^{234}Th: ^{238}U disequilibria. Deep Sea Res. Part A. Oceanogr. Res. Pap. 39, 1115–1137. doi:10.1016/0198-0149(92)90060-7

Burbank, D.C., 1974. Suspended Sediment Transport and Deposition in Alaskan Coastal Waters. University of Alaska Fairbanks. M.S. Thesis.

Burd, A., Jackson, G., 2002. Shining a light on the ocean's twilight zone. EOS, Trans. Am. Geophys. Union 83, 579–580. doi:10.1029/2002EO000392

Burd, A.B., Hansell, D.A., Steinberg, D.K., Anderson, T.R., Arístegui, J., Baltar, F., Beaupré, S.R., Buesseler, K.O., DeHairs, F., Jackson, G.A., Kadko, D.C., Koppelmann, R., Lampitt, R.S., Nagata, T., Reinthaler, T., Robinson, C., Robison, B.H., Tamburini, C., Tanaka, T., 2010. Assessing the apparent imbalance between geochemical and biochemical indicators of meso- and bathypelagic biological activity: What the @$#! is wrong with present calculations of carbon budgets? Deep Sea Res. Part II Top. Stud. Oceanogr. 57, 1557–1571. doi:10.1016/j.dsr2.2010.02.022

Burd, A.B., Jackson, G., 2009. Particle Aggregation. Ann. Rev. Mar. Sci. 1, 65–90. doi:10.1146/annurev.marine.010908.163904

Burd, A.B., Jackson, G., Moran, S.B., 2007. The role of the particle size spectrum in estimating

    POC fluxes from disequilibrium. Deep Sea Res. Part I Oceanogr. Res. Pap. 54, 897–918.

    doi:10.1016/j.dsr.2007.03.006

Carmack, E., Winsor, P., Williams, W., 2015. The contiguous panarctic Riverine Coastal

    Domain: A unifying concept. Prog. Oceanogr. doi:10.1016/j.pocean.2015.07.014

Coyle, K.O., Pinchuk, A.I., 2005. Seasonal cross-shelf distribution of major zooplankton taxa on

    the northern Gulf of Alaska shelf relative to water mass properties, species depth

    preferences and vertical migration behavior. Deep Sea Res. Part II Top. Stud. Oceanogr. 52,

    217–245. doi:10.1016/j.dsr2.2004.09.025

Coyle, K.O., Pinchuk, A.I., 2003. Annual cycle of zooplankton abundance, biomass and

    production on the northern Gulf of Alaska shelf, October 1997 through October 2000. Fish.

    Oceanogr. 12, 327–338. doi:10.1046/j.1365-2419.2003.00256.x

Crawford, W.R., Brickley, P.J., Thomas, A.C., 2007. Mesoscale eddies dominate surface

    phytoplankton in northern Gulf of Alaska. Prog. Oceanogr. 75, 287–303.

    doi:10.1016/j.pocean.2007.08.016

Dall'Olmo, G., Mork, K.A., 2014. Carbon export by small particles in the Norwegian Sea.

    Geophys. Res. Lett. 41, 2921–2927. doi:10.1002/2014GL059244

Dilling, L., Alldredge, A.L., 2000. Fragmentation of marine snow by swimming

    macrozooplankton: A new process impacting carbon cycling in the sea. Deep. Res. I 47,

    1227–1245.

Dilling, L., Wilson, J., Steinberg, D., Alldredge, A., 1998. Feeding by the euphausiid *Euphausia*

    pacifica and the copepod *Calanus pacificus* on marine snow. Mar. Ecol. Prog. Ser. 170,

    189–201.

Durkin, C.A., Estapa, M.L., Buesseler, K.O., 2015. Observations of carbon export by small

    sinking particles in the upper mesopelagic. Mar. Chem. 175, 72–81.

    doi:10.1016/j.marchem.2015.02.011

Ebersbach, F., Trull, T.W., 2008. Sinking particle properties from polyacrylamide gels during the

    Kerguelen Ocean and Plateau compared Study (KEOPS): Zooplankton control of carbon

    export in an area of persistent natural iron inputs in the Southern Ocean. Limnol. Oceanogr.

    53, 212–224. doi:10.4319/lo.2008.53.1.0212

Elimelech, M., Gregory, J., Jia, X., Williams, R., 1995. Particle Deposition and Aggregation:

    Measurement, Modelling and Simulation. Butterworth-Heinemann, Inc, Oxford.

Feely, R., Baker, E.T., Schumacher, J.D., Massoth, G.J., Landing, W.M., 1979. Processes

    affecting the distribution and transport of suspended matter in the northeast Gulf of Alaska.

    Deep Sea Res. 26, 445–464.

Feely, R., Massoth, G.J., 1982. Sources, composition and transport of suspended particulate

    matter in lower Cook Inlet and northwestern Shelikof Strait, Alaska. NOAA Tech. Rep.

    ERL 415-PMEL 34.

Feely, R., Massoth, G.J., Landing, W.M., 1981. Major- and trace-element composition of

    suspended matter in the north-east Gulf of Alaska: Relationships with major sources. Mar.

    Chem. 10, 431–453. doi:10.1016/0304-4203(81)90020-7

Forest, A., Babin, M., Stemmann, L., Picheral, M., Sampei, M., Fortier, L., Gratton, Y., Bélanger, S., Devred, E., Sahlin, J., Doxaran, D., Joux, F., Ortega-Retuerta, E., Martín, J., Jeffrey, W.H., Gasser, B., Carlos Miquel, J., 2013. Ecosystem function and particle flux dynamics across the Mackenzie Shelf (Beaufort Sea, Arctic Ocean): an integrative analysis of spatial variability and biophysical forcings. Biogeosciences 10, 2833–2866. doi:10.5194/bg-10-2833-2013

Forest, A., Stemmann, L., Picheral, M., Burdorf, L., Robert, D., Fortier, L., Babin, M., 2012. Size distribution of particles and zooplankton across the shelf-basin system in southeast Beaufort Sea: combined results from an Underwater Vision Profiler and vertical net tows. Biogeosciences 9, 1301–1320. doi:10.5194/bg-9-1301-2012

Fowler, S.W., Knauer, G., 1986. Role of large particles in the transport of elements and organic compounds through the oceanic water column. Prog. Oceanogr. 16, 147–194. doi:10.1016/0079-6611(86)90032-7

Freidlander, S.K., 2000. Smoke, Dust, and Haze: Fundamentals of Aerosol Dynamics. Oxford Univ. Press, New York.

Goldthwait, S., Yen, J., 2004. Quantification of marine snow fragmentation by swimming euphausiids. Limnol. Oceanogr. 49, 940–952. doi:10.4319/lo.2004.49.4.0940

Grebmeier, J., McRoy, C., Feder, H., 1988. Pelagic-benthic coupling on the shelf of the northern Bering and Chukchi Seas. I. Food supply source and benthic bio-mass. Mar. Ecol. Prog. Ser. 48, 57–67. doi:10.3354/meps048057

Grossart, H., Simon, M., 1998. Bacterial colonization and microbial decomposition of limnetic organic aggregates (lake snow). Aquat. Microb. Ecol. 15, 127–140. doi:10.3354/ame015127

Guidi, L., Calil, P.H.R., Duhamel, S., Björkman, K.M., Doney, S.C., Jackson, G., Li, B., Church, M.J., Tozzi, S., Kolber, Z.S., Richards, K.J., Fong, A., Letelier, R.M., Gorsky, G., Stemmann, L., Karl, D.M., 2012. Does eddy-eddy interaction control surface phytoplankton distribution and carbon export in the North Pacific Subtropical Gyre? J. Geophys. Res. 117, G02024. doi:10.1029/2012JG001984

Guidi, L., Gorsky, G., Claustre, H., Miquel, J.C., Picheral, M., Stemmann, L., 2008a. Distribution and fluxes of aggregates >100 μm in the upper kilometer of the South-Eastern Pacific. Biogeosciences 5, 1361–1372. doi:10.5194/bg-5-1361-2008

Guidi, L., Jackson, G., Stemmann, L., Miquel, J.C., Picheral, M., Gorsky, G., 2008b. Relationship between particle size distribution and flux in the mesopelagic zone. Deep Sea Res. Part I Oceanogr. Res. Pap. 55, 1364–1374. doi:10.1016/j.dsr.2008.05.014

Guidi, L., Stemmann, L., Jackson, G., Ibanez, F., Claustre, H., Legendre, L., Picheral, M., Gorsky, G., 2009. Effects of phytoplankton community on production, size, and export of large aggregates: A world-ocean analysis. Limnol. Oceanogr. 54, 1951–1963. doi:10.4319/lo.2009.54.6.1951

Hopcroft, R.R., Coyle, K.O., Weingartner, T.J., Whitledge, T.E., 2010. Gulf of Alaska Long-term Observations: the Seward Line 2008 / 9, NPRB Project Final Report. Fairbanks, Alaska.

Ittekkot, V., 1993. The abiotically driven biological pump in the ocean and short-term fluctuations in atmospheric CO_2 contents. Glob. Planet. Change 8, 17–25. doi:10.1016/0921-8181(93)90060-2

Iversen, M.H., Ploug, H., 2010. Ballast minerals and the sinking carbon flux in the ocean:
    carbon-specific respiration rates and sinking velocity of marine snow aggregates.
    Biogeosciences 7, 2613–2624. doi:10.5194/bg-7-2613-2010

Jackson, G., 1995. Comparing observed changes in particle size spectra with those predicted
    using coagulation theory. Deep Sea Res. Part II Top. Stud. Oceanogr. 42, 159–184.
    doi:10.1016/0967-0645(95)00010-N

Jouandet, M.-P., Jackson, G., Carlotti, F., Picheral, M., Stemmann, L., Blain, S., 2014. Rapid
    formation of large aggregates during the spring bloom of Kerguelen Island: observations
    and model comparisons. Biogeosciences 11, 4393–4406. doi:10.5194/bg-11-4393-2014

Kilps, J.R., Logan, B.E., Alldredge, A.L., 1994. Fractal dimensions of marine snow determined
    from image analysis of *in situ* photographs. Deep Sea Res. Part I Oceanogr. Res. Pap. 41,
    1159–1169. doi:10.1016/0967-0637(94)90038-8

Kiørboe, T., 2001. Formation and fate of marine snow: small-scale processes with large-scale
    implications. Sci. Mar. 65, 57–71.

Klaas, C., Archer, D.E., 2002. Association of sinking organic matter with various types of
    mineral ballast in the deep sea: Implications for the rain ratio. Global Biogeochem. Cycles
    16, 1–14. doi:10.1029/2001GB001765

Ladd, C., Stabeno, P., Cokelet, E.D., 2005. A note on cross-shelf exchange in the northern Gulf
    of Alaska. Deep Sea Res. Part II Top. Stud. Oceanogr. 52, 667–679.
    doi:10.1016/j.dsr2.2004.12.022

Laevastu, T., Favorite, F., Larkins, H.A., 1979. Resource Assessment and Evaluation of the
    Dynamics of the Fisheries Resources in the Northeast Pacific with Numerical Ecosystem
    Models. US Department of Commerce, National Marine Fisheries Service.

Lampitt, R.S., Noji, T., von Bodungen, B., 1990. What happens to zooplankton faecal pellets?

Implications for material flux. Mar. Biol. 104, 15–23. doi:10.1007/BF01313152

Lampitt, R.S., Wishner, K.F., Turley, C.M., Angel, M.V., 1993. Marine snow studies in the

Northeast Atlantic Ocean: distribution, composition and role as a food source for migrating

plankton. Mar. Biol. 116, 689–702. doi:10.1007/BF00355486

Landing, W.M., Feely, R.A., 1981. The chemistry and vertical flux of particles in the

northeastern Gulf of Alaska. Deep Sea Res. 28A, 19–37.

Martin, J.H., 1987. VERTEX: Carbon cycling in the northeast Pacific. Deep Sea Res. 34, 267–

285.

Martin, J.H., Gordon, R.M., Fitzwater, S., Broenkow, W.W., 1989. Vertex: phytoplankton/iron

studies in the Gulf of Alaska. Deep Sea Res. Part A. Oceanogr. Res. Pap. 36, 649–680.

doi:10.1016/0198-0149(89)90144-1

McCave, I.N., 1984. Size spectra and aggregation of suspended particles in the deep ocean. Deep

Sea Res. Part A. Oceanogr. Res. Pap. 31, 329–352. doi:10.1016/0198-0149(84)90088-8

McCave, I.N., 1975. Vertical flux of particles in the ocean. Deep Sea Res. Oceanogr. Abstr. 22,

491–502. doi:10.1016/0011-7471(75)90022-4

McDonnell, A.M.P., Buesseler, K.O., 2012. A new method for the estimation of sinking particle

fluxes from measurements of the particle size distribution, average sinking velocity, and

carbon content. Limnol. Oceanogr. Methods 10, 329–346. doi:10.4319/lom.2012.10.329

McDonnell, A.M.P., Lam, P.J., Lamborg, C.H., Buesseler, K.O., Sanders, R., Riley, J.S.,

Marsay, C., Smith, H.E.K., Sargent, E.C., Lampitt, R.S., Bishop, J.K.B., 2015. The

oceanographic toolbox for the collection of sinking and suspended marine particles. Prog.

Oceanogr. 133, 17–31. doi:10.1016/j.pocean.2015.01.007

Napp, J.M., 1996. The plankton of Shelikof Strait, Alaska: Standing stock, production, mesoscale variability and their relevance to larval fish survival. Fish. Oceanogr. 5, 19–38. doi:10.1111/j.1365-2419.1996.tb00080.x

Neal, E.G., Hood, E., Smikrud, K., 2010. Contribution of glacier runoff to freshwater discharge into the Gulf of Alaska. Geophys. Res. Lett. 37, 1–5. doi:10.1029/2010GL042385

Ohman, M.D., Powell, J.R., Picheral, M., Jensen, D.W., 2012. Mesozooplankton and particulate matter responses to a deep-water frontal system in the southern California Current System. J. Plankton Res. 34, 815–827. doi:10.1093/plankt/fbs028

Parker, D.S., Kaufman, W.J., Jenkins, D., 1972. Floc breakup in turbulent flocculation processes. J. Sanit. Eng. Div. 98, 79–99.

Peterson, M.L., Wakeham, S.G., Lee, C., Askea, M., Miquel, J.C., 2005. Novel techniques for collection of sinking particles in the ocean and determining their settling rates. Limnol. Oceanogr. Methods 3, 520–532. doi:10.4319/lom.2005.3.520

Picheral, M., Guidi, L., Stemmann, L., Karl, D.M., Iddaoud, G., Gorsky, G., 2010. The Underwater Vision Profiler 5: An advanced instrument for high spatial resolution studies of particle size spectra and zooplankton. Limnol. Oceanogr. Methods 8, 462–473. doi:10.4319/lom.2010.8.462

Powell, R.D., Molnia, B.F., 1989. Glacimarine sedimentary processes, facies and morphology of the south-southeast Alaska shelf and fjords. Mar. Geol. 85, 359–390. doi:10.1016/0025-3227(89)90160-6

Reimnitz, E., 1966. Late quaternary history and sedimentation of the Copper River delta and vicinity, Alaska. University of California La Jolla.

Richardson, T.L., Jackson, G.A., 2007. Small phytoplankton and carbon export from the surface ocean. Science 315, 838–840. doi:10.1126/science.1133471

Riley, J.S., Sanders, R., Marsay, C., Le Moigne, F.C., Achterberg, E.P., Poulton, J., 2012. The relative contribution of fast and slow sinking particles to ocean carbon export. Global Biogeochem. Cycles 26, 1–10. doi:10.1029/2011GB004085

Roullier, F., Berline, L., Guidi, L., Durrieu De Madron, X., Picheral, M., Sciandra, A., Pesant, S., Stemmann, L., 2014. Particle size distribution and estimated carbon flux across the Arabian Sea oxygen minimum zone. Biogeosciences 11, 4541–4557. doi:10.5194/bg-11-4541-2014

Royer, T.C., 2005. Hydrographic responses at a coastal site in the northern Gulf of Alaska to seasonal and interannual forcing. Deep Sea Res. Part II Top. Stud. Oceanogr. 52, 267–288. doi:10.1016/j.dsr2.2004.09.022

Royer, T.C., 1982. Coastal fresh water discharge in the northeast Pacific. J. Geophys. Res. 87, 2017–2021.

Royer, T.C., 1975. Seasonal variations of waters in the northern Gulf of Alaska. Deep Sea Res. 22, 403–416.

Sambrotto, R.N., Lorenzen, C., 1987. Phytoplankton and primary production, in: Hood, D.W., Zimmerman, S.T. (Eds.), The Gulf of Alaska, Physical Environment and Biological Resources. NOAA, US Government Printing Office, Washington, DC, pp. 249–282.

Sharma, G.D., Wright, F.F., Burns, J.J., Burbank, D.C., 1974. Sea surface circulation, sediment transport and marine mammal distribution. Alaska Cont. Shelf ERTS Final Report. Natl. Tech. Serv. Rep. E74-10711. 77 pp.

Sieburth, J.M., Lenz, J., 1978. Pelagic ecosystem structure : heterotrophic compartments of the plankton and their relationship to plankton size fractions. Limnol. Oceanogr. 23, 1256

Siegenthaler, U., Wenk, T., 1984. Rapid atmospheric CO_2 variations and ocean circulation. Nature 308, 624–626. doi:10.1038/308624a0

Silver, M.W., 1978. Marine snow: microplankton habitat and source of small-scale patchiness in pelagic populations. Science 201, 371–373.

Smayda, T.J., 1969. Some measurements of the sinking rate of fecal pellets. Limnol. Oceanogr. 14, 621–625. doi:10.4319/lo.1969.14.4.0621

Smith, D.C., Simon, M., Alldredge, A.L., Azam, F., 1992. Intense hydrolytic enzyme activity on marine aggregates and implications for rapid particle dissolution. Nature 359, 139–142.

Stemmann, L., Boss, E., 2012. Plankton and particle size and packaging: from determining optical properties to driving the biological pump. Ann. Rev. Mar. Sci. 4, 263–290. doi:10.1146/annurev-marine-120710-100853

Stemmann, L., Eloire, D., Sciandra, A., Jackson, G., Guidi, L., Picheral, M., Gorsky, G., 2008. Volume distribution for particles between 3.5 to 2000 µm in the upper 200 m region of the South Pacific Gyre. Biogeosciences Discuss. 5, 299–310. doi:10.5194/bgd-4-3377-2007

Stemmann, L., Jackson, G.A., Gorsky, G., 2004. A vertical model of particle size distributions and fluxes in the midwater column that includes biological and physical processes—Part II: application to a three year survey in the NW Mediterranean Sea. Deep Sea Res. Part I Oceanogr. Res. Pap. 51, 885–908. doi:10.1016/j.dsr.2004.03.002

Syvitski, J.P.M., 1989. On the deposition of sediment within glacier-influenced fjords: Oceanographic controls. Mar. Geol. 85, 301–329. doi:10.1016/0025-3227(89)90158-8

Takahashi, K., Fujitani, N., Yanada, M., 2002. Long term monitoring of particle fluxes in the Bering Sea and the central subarctic Pacific Ocean, 1990-2000. Prog. Oceanogr. 55, 95–112. doi:10.1016/S0079-6611(02)00072-1

Tang, Q.S., Gulick, S.P.S., Sun, L.T., 2014. Seismic observations from a Yakutat eddy in the northern Gulf of Alaska. J. Geophys. Res. Ocean. 119, 3535–3547. doi:10.1002/2014JC009938.Received

Verdugo, P., Alldredge, A.L., Azam, F., Kirchman, D.L., Passow, U., Santschi, P.H., 2004. The oceanic gel phase: a bridge in the DOM–POM continuum. Mar. Chem. 92, 67–85. doi:10.1016/j.marchem.2004.06.017

Volk, T., Hoffert, M.I., 1985. Ocean carbon pumps: analysis of relative strengths and efficiencies in ocean-drive atmospheric CO_2 changes. Geophys. Monogr. Ser. 32, 99–110.

Walsh, I.D., Gardner, W.D., 1992. A comparison of aggregate profiles with sediment trap fluxes. Deep Sea Res. Part A. Oceanogr. Res. Pap. 39, 1817–1834. doi:10.1016/0198-0149(92)90001-A

Wong, C.S., Whitney, F.A., Crawford, D.W., Iseki, K., Matear, R.J., Johnson, W.K., Page, J.S., Timothy, D., 1999. Seasonal and interannual variability in particle fluxes of carbon , nitrogen and silicon from time series of sediment traps at Ocean Station P , 1982-1993 : relationship to changes in subarctic primary productivity. Deep Sea Res. II 46, 2735–2760.

Young, H.D., 1962. Statistical Treatment of Experimental Data. McGraw-Hill Book Company, Inc., San Francisco, CA.

Appendix

Underwater Vision Profiler Deployment and Zooprocess Data Processing: A User Manual

1. **Installing Zooprocess**
   a. Install Java
      i. Make sure the folder "Java" is in Program Files, not only Program Files(x86)
   b. Install Image J
      i. install it right on the desktop
      ii. When computer tells you it cannot locate a Java file, wait until it lets you browse
      iii. Go into Program Files→ Java→ jre6→ bin
      iv. Select "javaw" (application). Image J will pop up with a window saying this is your new Java file.
   c. Install RS232 Tools
      i. These are 4 files located in the desktop folder UVP → pc_applications_drivers and softwares → W7_64bits → rs232_w64. It is an unzipped, normal folder. The zip folder only has 2 of the 4 necessary files.
      ii. All 4 files are also located in the Downloads folder and on the blue USB drive, if you can't find them.
      iii. Copy and paste: **RXTXcomm.jar** and **serial_ext.jar** into the Program Files folder ImageJ - plugins
      iv. Copy and paste: **rxtxParallel.dll** and **rxtxSerial.dll** into the C drive folder Program Files - Java - jre6 - bin
   d. Install Zooprocess
      i. Find the zip file "Zooprocess_version_7.19" located in the desktop folder UVP (or on the flashdrive) → pc_applications_drivers and softwares → Softwares → Zooprocess719
      ii. Create a folder called "Zooprocess" on the C drive (NOT in Program Files)
      iii. Extract all files to the C drive Zooprocess folder you just made
      iv. Open the Zooprocess folder and sort by file type.
      v. Highlight ALL the *.txt files. Copy and paste into the folder ImageJ → macros. Choose "Copy and Replace" for all if prompted.

vi.   In the Zooprocess folder, highlight all the *.class and *.java folders (should be 6 total files). Copy and paste into the folder ImageJ→ plugins

e. Open Zooprocess and set it up for the UVP

    i.   Click the ImageJ desktop icon

    ii.   A series of pop-up windows will flash, starting with a grey colored one reading "WAIT! Zooprocess being started"

    iii.   When prompted, fill in the following information:

        1. C: drive location for any folders to be installed

        2. Device: uvp5

        3. Serial number: 009

        4. COM port: check in Start menu→ Devices and Printers to see which COM port you plugged the cord into. Note which space this is on the laptop.

    iv.   In the EDIT CONFIGURATION FILE window, leave everything as is, EXCEPT for the three bottom boxes. Each path, HD and FD, should contain "sn009" (NOT sn003)

    v.   Most of the numbers in the configuration data file windows are fine as-is. You need to make sure the following are changed:

        1. Light 1: h25

        2. Light 2: h26

        3. Image volume: 0.93

        4. Pixel size: 0.148

        5. Smbase(pixel): 1

        6. Smzoo min(pixel): 30

        7. aa: 0.0032

    vi.   It will ask you to create a new project. Create it in the C: drive, and name it something appropriate.The resulting project folder created by the software will read C:\uvp5_sn009_"your project name"

    vii.   If asked to create Pilot files for the UVP, click yes or ok. Choose the appropriate COM port.

    viii.   Important: make sure the path is to the correct serial number 009!

    ix.   When this is done, the starting point window for anything you will do in Zooprocess should open up, looking like this:

ZOOPROCESS   version 7.16   2013/0...   X

--------------------- Instrument : UVP5 ---------------------

--------------------- ZOOPROCESS ---------------------

--------------------- for ImageJ version 1.41o ---------------------

----

Laboratoire d'Oceanologie de Villefranche sur mer

CNRS - UPMC

marc.picheral@obs-vlfr.fr

Please refer to Zooprocess and ImageJ if used for Publication

http://rsb.info.nih.gov/ij/index.html

SELECT PROJECT

C:\uvp5_sn009_test   ▼

OK   Cancel
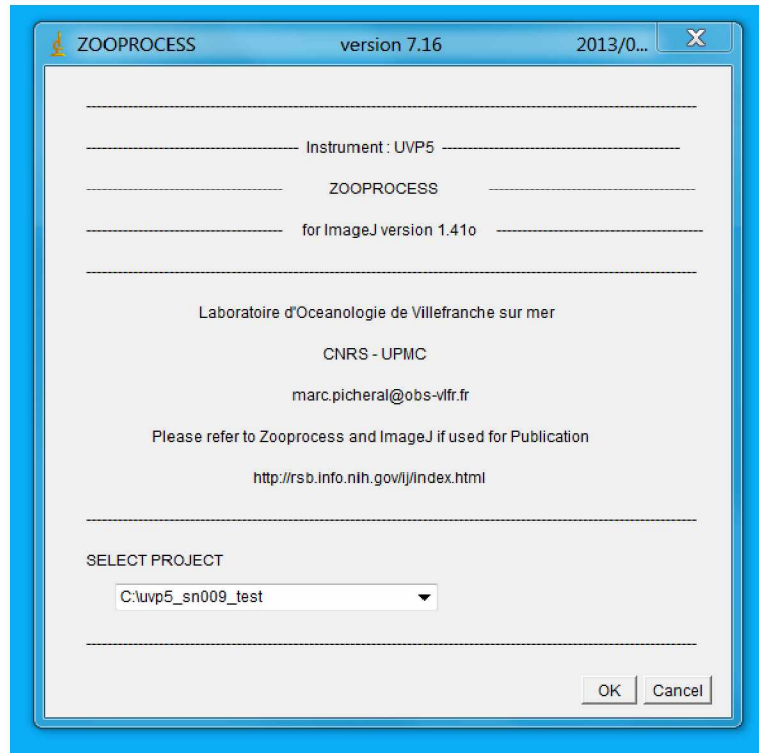
  x. You can either close Image J for now, OR move on to section 4, "Downloading Data off the UVP"

2. Testing that the UVP camera is functioning

 a. Attach Lights to UVP

  i. Assemble the metal frame to the light unit, using provided hardware (see UVP5 manual for pictures)

  ii. Assemble the brackets to the metal frame, very loosely for now.

  iii. With help (this is a two-person operation) slide the UVP cylinder slowly through the brackets. One person needs to look at the alignment, meanwhile: line up the arrow sticker on the cylinder EXACTLY with the arrow sticker on the metal frame. This is so that the lights and camera are the correct distance from each other, like the flash on a regular camera.

  iv. Screw the brackets tighter when the cylinder is in just the right place.

  v. Connect the blue cable to each light and to the top of the UVP cylinder. Make sure the space between the camera and the lights is still unobstructed by the thick part of the cable.

 b. Power up UVP using shunts

  i. This section is called "Steps to be happy when receiving UVP" in the UVP5 manual from M. Picheral.

  ii. First, plug in the pink-colored Power Shunt to its place EITHER at the end of the pink power 1 m extenstion cord OR to the top of the instrument.

iii.   Second, plug in the yellow colored Input/Output (I/O) Shunt to its place EITHER at the end of the yellow power 1 m extenstion cord OR to the top of the instrument. This has to be done AFTER the power shunt, in this order only.

iv.   Note: there are five different color-coded connector ports on the top of the main stainless steel cylinder of the camera (pictured below).

    1. the blue-colored port connected the camera to the LED lights.

    2. the red-colored port powered the UVP.

        a. For deployment, a power shunt was connected to this red port on the cylinder using an extension cord to tell the camera to turn on. During deployment, all other communication ports housed dummy plugs except for the power port and the lighting port. During time on deck in transit, the UVP was connected to the deck unit to charge the camera battery using the red power port.

    3. the green-colored port was used to transfer data to and from the camera.

        a. While on deck, the UVP was connected to the deck unit using this green port to download and delete data off the camera.

    4. the orange-colored analog output port enabled real-time communication between the CTD and the UVP.

    5. the yellow-colored port provided the option to start sampling via an input-output (I/O) shunt.
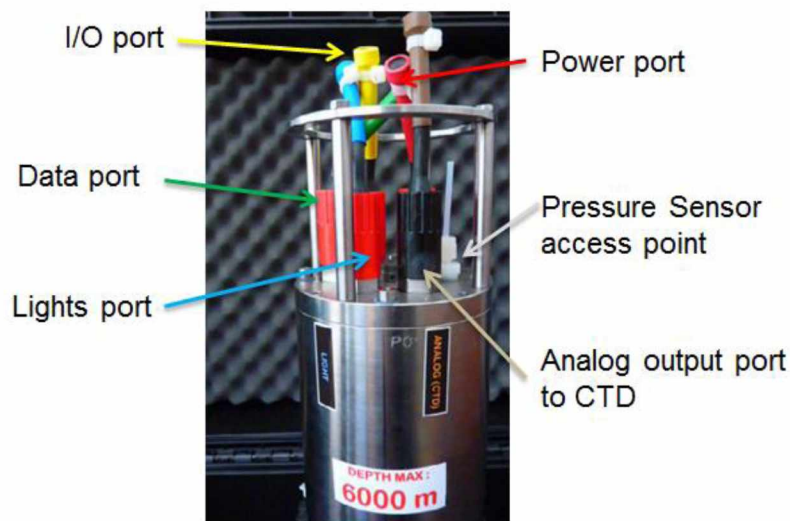
     v.   Within 2 minutes, the light unit should begin flashing. It is functioning!

     vi.   Now, unplug the yellow I/O Shunt. This tells the UVP to stop sampling.

     vii.   Wait AT LEAST 1 minute. This is a good time to hose off the instrument with freshwater, move it to a better location, tie it down, etc. if you are out on the water.

     viii.   After a minute or two, unplug the pink Power Shunt. This turns the UVP off.

     ix.   Note: always keep very good track of all dummy plugs, they are small and easy to misplace. Always place them back on the ends of the exposed metal prongs, which should be dried off and greased up when necessary.

3. Connecting the UVP to the computer

    a.   Set up the deck unit (pictures provided in UVP5 manual)

        i.   Plug in the deck unit with the black power cable to a normal outlet.

        ii.   Connect the Power Cable to the deck unit (circular, metal end) and the UVP (pink colored end)

        iii.   Connect the Sea Cable to the deck unit, and the UVP (green colored end)

        iv.   Connect the Ethernet cord to the deck unit and to the computer

        v.   Connect the Serial port cord to the deck unit, and plug the USB end of the cord into the computer.

    b.   Turn on and charge the UVP

        i.   Turn on the deck unit with the red rectangular switch on the back of the unit. The small red light labeled "POWER ON" should light up on the front of the unit, though it will be hard to see in bright light.

        ii.   Turn on the volt meter, small metal switch labeled "VU METER ON/OFF"

        iii.   Turn on the Red UVP External Power switch. The V and I numbers will read the charge and flow, respectively. The left (V) box will read 29.5 when fully charged. The right (I) box will read a negative number for now, since power is flowing out of the UVP.

        iv.   Turn on the Green UVP Charger switch. The right (I) box will now read a positive number – this means you are charging the UVP and energy is flowing into the device from the deck unit.

4. Troubleshooting Connection Problems

    a.   Check computer IP settings

        i.   In Windows, go to the start menu. Click Control Panel, then Network and Internet, then Network and Sharing Center.

        ii.   Make sure deck unit and UVP are turned on.

iii. There will be an "Unidentified network" in the Network and Sharing Center. To the right of that, click the "Local Area Connection" in blue lettering.

iv. Under the General tab, click the Details... button.

v. The Network Connection Details listed need to match the numbers in the UVP5 manual. It should look like this when done correctly:

Network Connection Details

Network Connection Details:

Property	Value
Connection-specific DNS S...	
Description	Intel(R) 82579LM Gigabit Network Conr
Physical Address	3C-97-0E-BC-F1-57
DHCP Enabled	No
IPv4 Address	193.49.112.105
IPv4 Subnet Mask	255.255.255.0
IPv4 Default Gateway	193.49.112.1
IPv4 DNS Server	193.49.112.3
IPv4 WINS Server	
NetBIOS over Tcpip Enabl...	Yes

vi. If it does not look like this, take the following steps:

1. In the start menu, click on Control Panel. In the search box, type "adapter." When items come up, under Network and Sharing Center, click "View network connections" in blue type.

2. Right click on "Local Area Connection." Click Properties. Under the Networking tab, Select "Internet Protocol Version 4 (TCP/IPv4)" and click the Properties button below.

3. In the General tab, type the following 4 sets of numbers in the appropriate boxes. Leave the "Alternate DNS server" box blank.
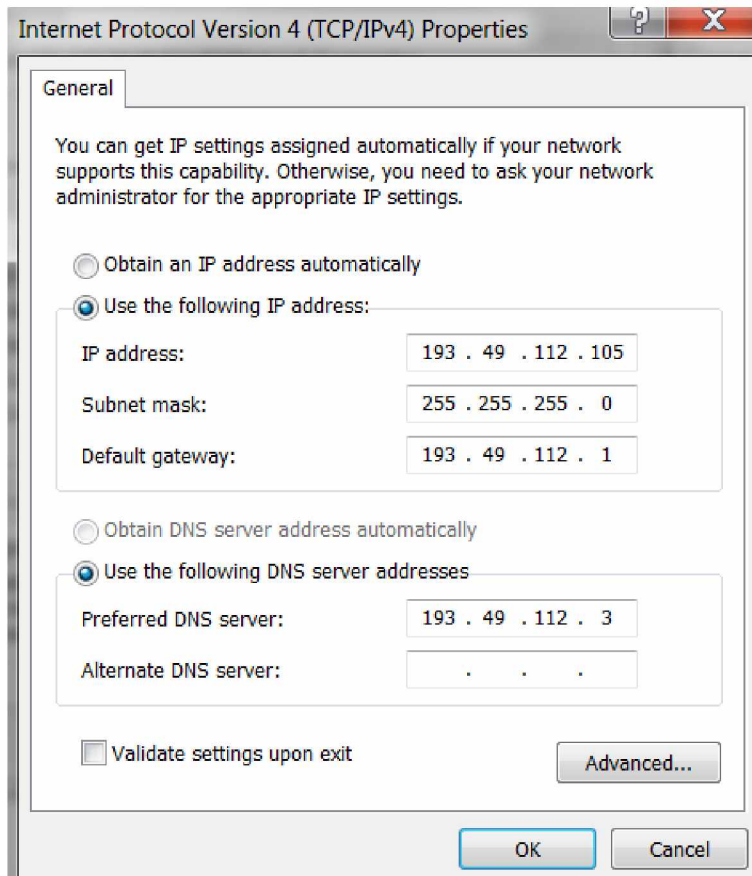
b. Check/fix computer COM port settings
   i. Plug in the blue USB flash drive. It contains the driver for the serial port.
   ii. In Computer → USB flash drive (called SN009), Copy and paste the Edgeport driver into the desktop of the computer. This may require administrator passwords.
   iii. In Windows, go to the start menu and click "Devices and Printers." Under "Unspecified" there should be a device called UC232R.
   iv. Double click on UC232R and go to the Hardware tab. The information listed shows you which COM port it is plugged into. (In the example below, it's COM port 7):
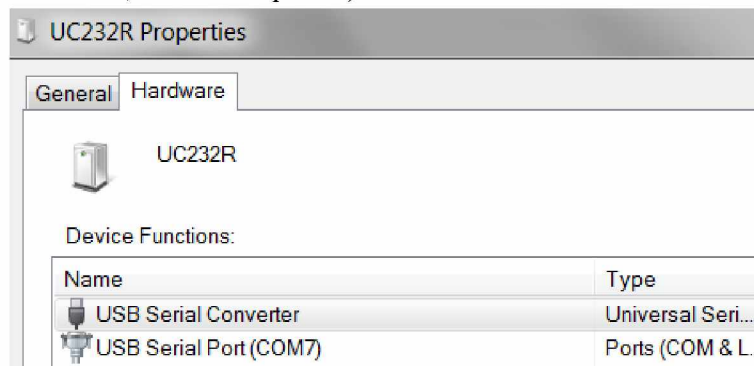
c. Test the COM port in Zooprocess
    i. Whenever you create a new project, you can enter the COM port again.
    ii. Open Image J, wait for the Zooprocess window to show SELECT PROJECT. Select your most recent project folder, click Ok.
    iii. Select "SWITCH mode" and click Ok. The bottom of the window will now read ADVANCED MODE. Always do this.
    iv. Under the drop down menu named SELECT PROCESS for UVP5, select "UVP5 PILOT TOOLS (port com needed)" and click Ok.
        1. Common problem here: sometimes a pop-up window appears displaying the following message:

Macro Error

Index (0) out of 0--1 range in line 54.

dat = split (data [0 <]> , " ") ;

OK
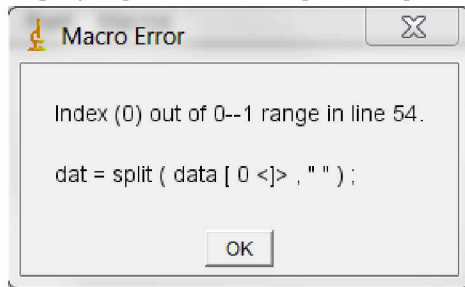
This means the COM port is not working correctly. To fix it, you have to completely reinstall ImageJ and Zooprocess over again. Delete all the files and icons for those two programs, then start over from section 1 of this manual.

    v. If you are allowed to go into Pilot tools: a window will pop up saying "Check that UVP is ON." Make sure the deck unit is on and the Red UVP External Power switch is on.
    vi. A window called "UVP5 PILOT MODULE" will pop up. In the drop down menu select "TEST & MONITOR COM PORT"
    vii. A window will pop up telling you what to do. Press Ok. Click in the Image J window and hit space bar as prompted. The Log will show you that you just opened and closed the COM port.
    viii. On the drop down menu, select EXIT PILOT MODULE and click Ok.
    ix. Turn off the UVP Red Power switch and turn off the deck unit.

5. **Programming the UVP for Deployment**
    a. Select new instrument, enter the following parameters:

EDIT CONFIGURATION FILE

Instrument : uvp5
Source folder :   C:\Zooprocess\
Config file : process_install_config.txt

Pixel size (mm)   `0.148`

VALUES to be utilized for the processing of VIGNETTES & PID files

Threshold for segmentation (upper)   `235` ▾
Gamma for vignette display (0.5 - 5)   `4`
Length of the scale line to be displayed in vignettes (mm)   `5.0` ▾

If "advancedi" option is enabled, the previous Learning sets may not be usable for this project !

Process option   `advancedi` ▾
Minimum depth to start to process vignettes (m)   `0.500`
ESD min for organisms to be analyzed (mm), note : 0.5 should be a minimum   `0.500`
ESD max for organisms to be analyzed (mm)   `100000`

These values will be writen in the modfile ("mixtfh", "mixhd", "fullhd") or to be defined for re-processing

Fields with * must be carefully documented. They influence the UVP5 image process.

Threshold*   `21`
Smbase* (pixel)   `1`
Smzoo min* (pixel)   `30`
Vignette size ratio   `3`
Full image width   `1280`
Full image heigth   `960`
Vignette ratio (2)   `2`

b. Select the appropriate Com port
   i. check this in Windows: Devices and Printers - look at which port Edgeport is listed under (COM __).
c. Set the following parameters. Most stayed the same except Select Upturn Depth range (m): which I set to 55 to enable CTD operator to lower it that deep to clear bubbles at start of cast (if necessary). You can also edit these by selecting "Edit Pilot Board Configuration File" while in Pilot Mode.
d. Into Pilot Mode, Selected READ/PROGRAM sequence
e. Click Yes here, then Click OK.
f. Upturn Flag =1 means the upturn flag is activated. 55 m is the vertical rise needed to shut down aquisition. If you want to edit these, select "Edit Pilot Board Configuration File" while in Pilot Mode.
g. After editing Pilot Board Configuration File, make sure to then select "SEND configuration file to UVP" before exiting Pilot Module!

h. Set Computer clock to UTC (Coordinated Universal Time)
i. Select "Synchronize UVP5 time with Computer Time"
j. This didnt seem to work. I had to edit the time manually.

6. **Troubleshooting Battery Problems**
   a. Lithium-Ion battery life decreases with time.
   b. The battery is doing well IF:
      i. Casts capture the full-depth profiles, the whole downcast.
      ii. Maximum voltage of the instrument is greater than 28.5 V when fully charged.
      iii. Charging unit successfully charges the UVP for more than 1 hour uninterrupted, with the current flowing out (right hand window on the deck unit) slowly decreasing from ~0.80 down to ~0.30 over the course of the charging time.
   c. It is time to rejuvenate the battery IF:
      i. Casts do not give you full depth profiles - this means the UVP is low enough in voltage that it turns off before it reaches the bottom.
      ii. Maximum voltage of the instrument is less than 27.5 V, i.e. you have trouble charging it beyond this voltage.
      iii. Charging unit is misbehaving - the current flowing into the UVP (right hand window on the deck unit) flickers from a positive number 0.60-0.90 down to "-0.00" after 30 minutes or so...not sufficient charging.
   d. To rejuvenate the battery:
      i. Detach all cables and remove UVP from the rosette. Strap it down in a secure location.
      ii. Attach the 1-m power extension cable. Use a vice or other securing device to keep the male end of this extension cable totally immobile.
      iii. Place electrical tape between the pins of the male end to separate them (see photo)

iv.   Use some kind of electrically-powered device (i.e. computer fan) that draws up to, but no more than, 1.0 Amps to drain the battery by attaching the cables to the pins of the male end of the power extension cable.

v.   The object you use to drain the battery should be simple to check whether your setup is working or not. For example, using 4 computer fans, the fans are visibly whirring when the setup is connected well, and the speed of the whirring decreases as the battery runs lower and lower (see phot
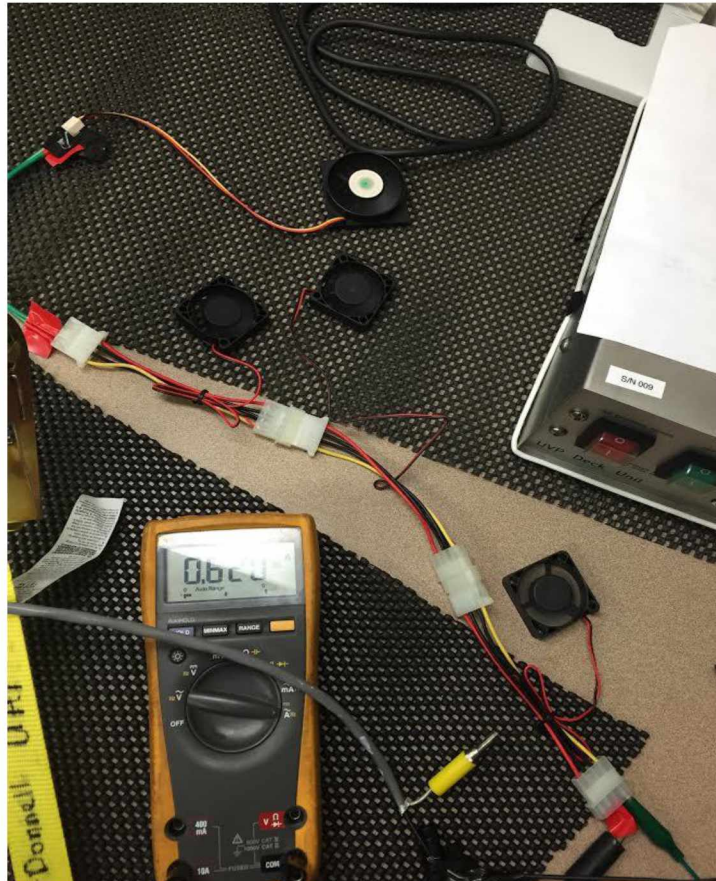
vi.   Attach a volt meter and periodically check the current flowing out of the UVP (Amps, DC) and the voltage of the instrument (V) by moving the cables and clamps around to the right locations.

vii. Write down the current and voltage changes along with what time you checked.

viii. The goal is for the voltage of the instrument to read as Zero.

ix.   When it's low enough, take down your discharging setup and reconnect the Data and Power cables that attach to the deck unit.

x.   Try to check the voltage using the deck unit: if it does not read anything (blank windows), that's fine, it means you have fully drained the battery.

xi.   Check the deck unit frequently to monitor the recharging process. WRite down the current and voltage changes along with the time as it recharges.

xii.   A successful recharge should result in a higher maximum voltage of the UVP when fully charged (greater than 28.5 V).

7. **Downloading data**
   a. For this, you can use the cylinder alone (no need to reassemble the frame or light unit).
   b. Connect everything as specified above. Turn all the switches on the desk unit on. UC232R should appear in Devices, and Unidentified network should appear in the Network and Sharing Center.
   c. Open ImageJ. Select your project.
   d. In the dropdown menu, select "UVP5 PILOT TOOLS (port com needed)" and click Ok.
   e. Make sure you are operating in ADVANCED MODE. If not, switch modes.
   f. In the next dropdown menu, select "DOWNLOAD data from UVP5"
   g. The Log window will begin to read lines of code. (things like "WATCHDOG")
   h. Look in the ImageJ window bar, and watch the text that appears there. A progress bar will appear when the camera is turning on inside the UVP.
       i.   One problem here: a pop up window will appear saying something about the event log. Ignore this box, Click Ok, it means nothing.
       ii. Another common problem here: after a few moments of the camera being on, all windows disappear. Then a pop-up window appears reading: "sn009/HD does not exist." After clicking ok, another pop-up window appears reading "sn009/FD does not exist."
   i. When the download begins, you will see a phrase beginning with the word "Opening…" flashing in the Image J window and a status bar. After the status bar fills, a series of windows will flash on the screen. This process will repeat itself several times.
   j. Downloading multiple profiles is time consuming. One profile can be ~10-20 minutes, but a whole cruise will take hours.
   k. In Control Panel → Hardware and Sound → Power Options: make sure the computer power settings are adjusted to "Never" for both sleep mode and hibernate mode, so that it will not turn off.
   l. After some time, return and check in the C:// drive to see the folder has been created and the "raw" folder has data inside of it.
   m. Select Exit Pilot Module from the dropdown menu, press Ok, and turn off the UVP deck unit switches when it has exited the Pilot Module.

8. **Troubleshooting Corrupted Files**
   a. Common problem: download ends prematurely with an error message saying "File is not in a supproted format…"

i. This means a file is corrupted in that cast, usually due to an early end to the cast to bring the rosette back on deck.

ii. Note the name of the corrupted raw file. In this case it was "20150611181137_468_0054.bmp"

iii. Go into UVP Pilot tools.

iv. Choose "turn UVP camera ON"

v. A pop up window will appear when the camera is on. LEAVE it there!

vi. Meanwhile, go into Windows: Computer: Map Network Drive. Choose a letter that is not used for other drive (i.e. not C or D or Z). Type "\\uvp5_sn009\FD"

vii. Now you can go into the UVP and manually delete files. 2 options are:
  1. Delete the whole raw folder that has the corrupted file. Especially if it was an aborted or incomplete cast anyway.
  2. Go into the corrupted folder, find the file, and delete all files from that number to the end.

viii. Exit the windows explorer window(s) you are using,

ix. push "Yes" in Image J to shut down the camera.

x. Before trying to download again, make sure to delete the raw folder from your project folder on the laptop.

9. **Entering Metadata**
   a. Choose "Fill in Metadata" from the dropdown menu and click Ok.
   b. When a pop up window appears saying there is not Metadata folder yet, you have to create one, click Ok.
   c. A status bar will start filling in in the Image J window, with the message "Checking RAW folders, WAIT!"
   d. Metadata window will pop up, under SELECT profile status bar, scroll down to a folder. A good choice is the first day of your data.
      i. The first 8 digits show the date. For example, a folder with a name beginning "HDR20140502…" is a profile taken on May 2, 2014.
      ii. The last 6 digits of the file name are the time in military GMT format. For example, last digits "042042" mean that profile was taken in GMT time 04:20:42, which is 8:20 pm the previous day in Alaska time.

     iii.   Important: when selecting a profile to enter metadata, ALWAYS check the box in the line that reads "Automatic First Image Selection (when possible)"
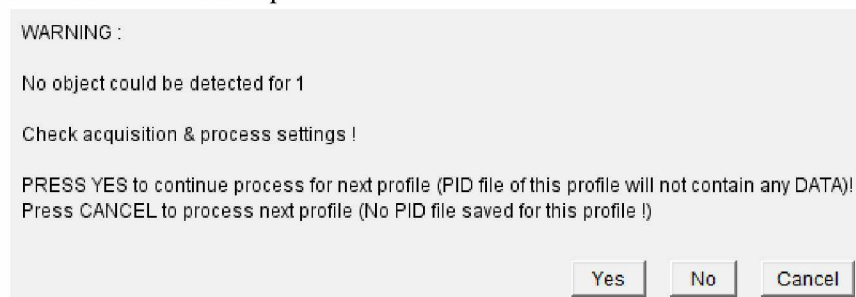
```
SELECT profile

    HDR20150729181730  ▼

---------------------------------------------------------------

☑ Automatic First Image selection (when possible) ?
```

e.   The next pop up window has lots of boxes to fill. Make sure to do:
     i.   Profile ID
     ii.   Station ID
     iii.   Bottom Depth
     iv.   CTD cast name (usually the station name, check with CTD watch)
     v.   Day or Night cast
     vi.   Latitude (during downcast)
     vii.   Longitude (during downcast)

f.   The rest can be left as-is, unless there are comments.

g.   Click Ok, and a pop up window will appear asking if you want to enter another station. Click Yes and repeat the process.

h.   When done, you can export the resulting .txt file from the meta folder to excel.
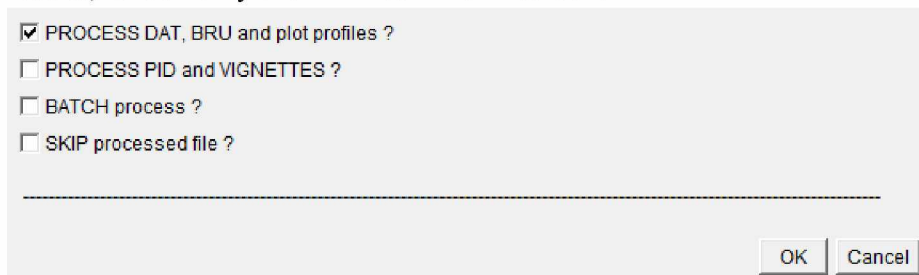
10. Processing Raw Data

a.   Choose "Process DAT, BRU, PID and VIGNETTES" from the dropdown menu and click Ok.

b.   If you have lots of time: Check all 5 of the boxes in the pop up window.

```
☑ PROCESS DAT, BRU ?
☑ Plot profiles ?
☑ PROCESS PID and VIGNETTES ?
☑ BATCH process ?
☑ SKIP processed file ?

----------------------------------------------------------------

                                            OK    Cancel
```

c.   Note the status bar in the Image J window slowly filling up, and/or blinking rapidly with different file names.

d.   This may take a while, for example 6-8 hours to process 24 casts.

e.   When this option works, your resulting data will be stored in the "work" and "results" folders, ordered by cast (Profile ID). See below for more on Data Storage Format.

f. Processing happens in order of the first digit of the Profile ID (i.e. "1" and "11" will be processed before "2" and "21")

g. Common problem: In places with very high particle concentrations, the UVP will create more than 6 .bru files in the raw data, which take a lot of memory to process. A pop up window titled "Exception" may appear with the top line of the box inside reading "java.lang.OutOfMemoryError.Java heap space." If this happens:

    i. Check the RAM of the computer you are using (usable, not total). Note what size would be ⅔ of that usable RAM.

    ii. Open Image J, and close all windows except for the main "ImageJ" menu window.

    iii. Edit > Options > Memory & Threads…

    iv. Set the memory usage to ⅔ of your usable RAM.

    v. Restart ImageJ and things should process without the memory error now.

h. Common problem: When a Profile ID has no images captured for it, the following window will come up:

```
WARNING :

No object could be detected for 1

Check acquisition & process settings !

PRESS YES to continue process for next profile (PID file of this profile will not contain any DATA)!
Press CANCEL to process next profile (No PID file saved for this profile !)

                                              Yes     No     Cancel
```

    i. In the case above, "1" was an upcast, so we wouldn't want images from it anyway.

    ii. Click Yes

    iii. Click Ok for the following 2 pop up windows

    iv. Continue processing

i. Common problem: sometimes only the DAT and BRU files will be processed, and something goes wrong with the PID and vignettes. A completely blank pop up window will appear with an Ok button, which, when clicked, doesn't close the window. If this happens, use task manager to close Image J, then start it again.

j. Troubleshooting: When checking all the boxes (as in 7.b. above) yields no results, Check only the DAT & BRU files box:

```
☑ PROCESS DAT, BRU and plot profiles ?
☐ PROCESS PID and VIGNETTES ?
☐ BATCH process ?
☐ SKIP processed file ?

--------------------------------------------------------------------------------

                                              OK    Cancel
```

i. This will not process the PID or vignettes, but will be a faster process and will provide all the data needed for basic particle concentrations and size distributions.

ii. Check: on the C:// drive → your project folder → "work" folder. You should see that a folder has been created for each ProfileID number you entered in the metadata (NOT the stations, just the profile numbers).

iii. In Zooprocess, after selecting your project, from the dropdown menu select "PLOT profiles from DAT files" and click Ok.

iv. Select the profile number you want to plot, click Ok.

v. In the boxes: Set maximum depth to greater than your deepest cast. Use the default settings for depth interval and smoothing.

vi. Windows will pop up, the last of which will tell you that your plots have been saved in the "results" folder.

vii. Find the window that popped up that contains the best-looking or best-plotted graph. In the lower lefthand corner of the window, click the box that says "List"

viii. A table will appear, with 2 columns showing depth and particle abundance. In the top of the window click File → Save As. Name it the station where this profile was taken.

ix. Double check that the file saved in the location you specified.

x. Close all the open windows and restart Image J.

xi. Repeat steps e. through l. for all profiles. Note which profiles you've plotted, which station it corresponds to, etc until all the .txt files have been saved.

11. Data Storage Format
a. File size:
   i. a typical whole-cruise project folder will be 20-30 GB after first-order processing (dat files, bru files, pid files, and vignettes).
b. Locations of files after processing BRU and DAT files:
   i. In the "results" folder
      1. The *.bru file for each profile will be much larger than the *_datfile.txt
      2. Both are organized into columns separated by semicolons.

The BRU file has the following columns:

Column	1	2	3	4	5	6
Data	Image #	Particle #	Area (pixels)	Grey scale	X position in image	Y position in image

The DAT file has the following columns:

Column	1	2	3	4-5	6-14	15	16	17	18	19
Data	Image #	Date & Time	Depth (centi-bars)	Camera angle	Battery info	# of small particles	Mean area of small p.	Grey scale of small p.	# of large particles	Grey scale of large p.

 c. Locations of files after processing PID and vignettes:

  i. In the "work" folder of your project folder: a folder for each Profile ID (each cast), containing:

   1. many 8-bit images in .jpeg format

   2. *_dat1.pid

   3. *_datfile.txt

   4. *_measurements.txt

   5. *_meta.txt

   6. HDR… .txt

   7. HDR… .dat

 d. Other note about processing:

  i. Zooprocess will process the files in order of the first digit of that file. i.e. it will process something labeled as "10" before it processes "6" because the first digit of 10 is a 1. This applies to both the particle data (DAT and BRU files) and the image sorting process later on.

  ii. PID & Vignettes processing takes MUCH longer than just DAT & BRU. If you are sampling lots of stations close together and are short on time, you can process DAT & BRU only and save the image step for later.

12. **Sorting Vignette images**

STEP 1. Build a learning set...

 a. Manually create a folder in Windows explorer full of empty folders.

  i. it's best to use the folder already called "Learning_set" which is located in your project folder → in "PID_process"

  ii. named the empty folders you create with the categories you are sorting (calanoid, aggregate, fecal, etc)

  iii. Make about 10-15 empty folder. More than this will confuse the software when it comes time for it to predict.

b. Open Plankton Identifier

c. Click the "Learning" button and a screen will open
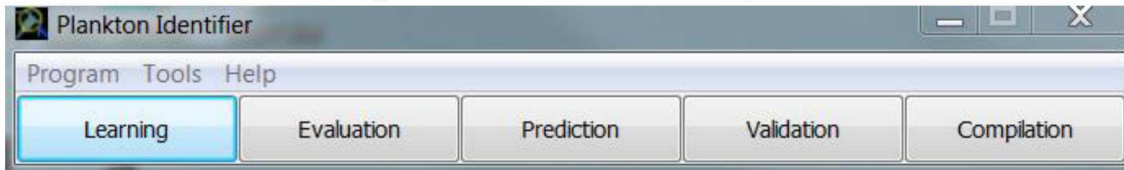
d. In the window called "Select Learning Set Folder," select the folder you want to sort images INTO (ideally "Learning_set"). click the Ok /check mark button.

e. The sorting window will open. On the right are the empty folders you created to build your learning set.

f. On the upper half of the main window, you must select the images you want to use to build the learning set.

g. In the "Sample Set" dropdown menu, choose one of the folders in the "work" folder of your project folder that contains lots of .jpeg images. (In the image below I chose the cast which had the profileID "24")
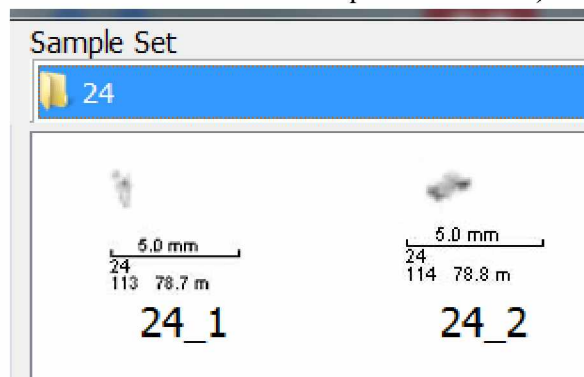
h. Drag and drop images into the folders on the right.

    i. As you do this, the sorted images will have a red X in the main window.

    ii. Also as you do this, in Windows explorer you will see the .pid files for the profile(s) you are selecting images from appearing in your "Learning_set" folder. Leave them there, this is just what the software does.

i. Use images from lots of different casts within each cruise. The better the variety, the more accurate the predictions will be when you actually use the learning set.

    i. include blurry, hazy, images and all orientations of an object, so the computer can learn based on all the possible representations.

j. Sort until you have about 300 images in each folder in your learning set.

    i. 300 won't be possible for some categories - just enough of those objects in the water.

k. When you are satisfied, Click the "Create Learning File" button at the bottom
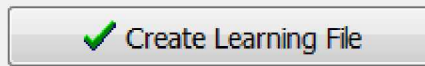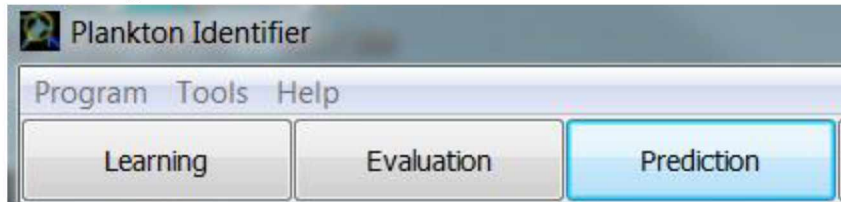

right corner of the screen

l. Note where you saved the learning data file (.pid file) - easy to lose

STEP 2: Ask the computer to predict for you

    m. In the original Plankton Idenfifier window, Click "Prediction"

    n.

    o. In the top left corner under "Select learning file" find the .pid file you just created

    p. Under "Select sample file(s)" choose the "_dat1.pid" files that you want to classify using your new learning set

        i. can be just one station, or all the files for the whole cruise.

        ii. locate them in the "PID-process" folder of your project folder, then in "Pid_results"

    q. Under "Select a method" select the Random Forest Algorithm, "Spv learning 6 (Random Forest).tdm"

    r. Make sure to check the box for "detailed results" - this will help with later steps.

        i. If you are just testing it out and don't plan to actually use this prediction, don't bother checking this box.

    s. Click "Run"

        i. A window will pop up called Results Destination, save the resulting file in the "Prediction" folder in the "PID_process" folder of your project folder

        ii. Uncheck boxes in the "Customized Variables" column as necessary. For example, when I ran a learning set, error messages popped up for PerimAreaexc, FeretAreaexc,and CDexc, so I unchecked those boxes and it ran successfully.
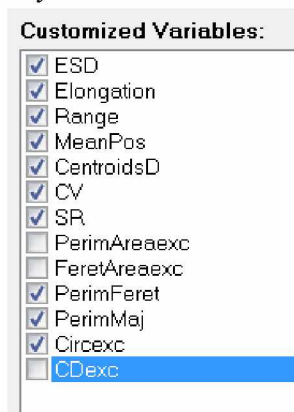
          iii.   Note: this may take a few minutes to process if you choose multiple casts/stations
   t.   When done, it will generate a file that pops up in an internet browser to view. The two most interesting parts of this file are:
          i.   "Bagging 1 (Rnd Tree)" is the confusion matrix generated by the computer's sorting
          ii.   "Univariate discrete stat 1" is the percentage of objects in each category sorted by the computer
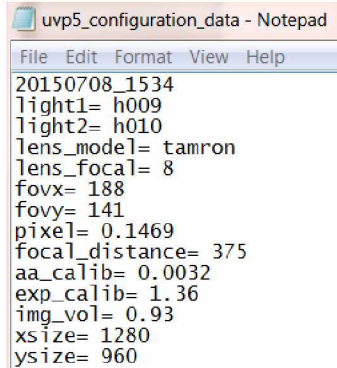
STEP 3: Validate what the computer predicted
   u.   Open Zooprocess by clicking on Image J
          i.   choose your project
          ii.   in the dropdown menu, choose "SORT…"
          iii.   choose the Prediction folder (located in your project folder → PID_process → prediction)
          iv.   choose "Process ALL files in the selected folder"
          v.   choose the prediction file (a .txt file that is a list of identifications) of your choice - I prefer "…reduced"
          vi.   This will take a while
          vii. in the dropdown menu, choose "EXTRACT…"
   v.   Sort the images in XnView (much more user friendly)
          i.   When opening XnView for the first time, make sure to check the box "all image files" in the very first startup window

13. Calculating Concentration and Size distribution
     Below is a list of general steps that can be used to calculate particle concentrations and size distributions based off the numerical particle data.

1. Load data from "results" folder
   a.   MATLAB will load the _.bru file as X_ (for example, for a profile given the Profile ID "4" MATLAB would import "4.bru" as a matrix called "X4"
   b.   MATLAB will load the _datfile.txt as X__datfile (for example, for Profile ID "4" MATLAB would import "4_datfile.txt" as a matrix called "X4_datfile"
2. Loop code for all stations in a transect
3. Delete data from upcasts or CTD-soaking, when descent rate is below a certain threshold
   a.   Convert depth in datfile from centibars to decibars
   b.   Add a column for depth to the .bru file, using datfile as an index
4. Create vector to tally the number of images taken at each depth
5. Based on data distribution, create depth bins that work (5 m is ideal in most cases).
6. Create vector to tally the number of particles detected within each depth bin

7. Divide particle number in each depth bin by sum of image volumes taken in that depth bin to get overall particle concentration (#/L)
   a. For a given depth bin: Image volume is set to 0.93 L. Sum of all particles detected in depth bin / (0.93 *sum of all images) = concentration (#/L).
8. Convert area in pixels to area in mm^2, removing glow, based on the equation from Picheral et al. 2010:
   a. $A_m = 0.0032 * A_p^{1.36}$
   b. where A_p is the area of the photographed particle surface in pixels and A_m the surface in mm^2.
   c. 0.0032 and 1.36 are constants derived from testing this individual UVP instrument in a tank with objects of known size, and comparing their known sizes to the sizes calculated by the UVP.
   d. These constants for each UVP can be found in the project folder > config > uvp5_settings > "uvp5_configuration_data.txt" . The multiplier is listed as "aa_calib" and the exponent is listed as "exp_calib."

```
uvp5_configuration_data - Notepad

File  Edit  Format  View  Help

20150708_1534
light1= h009
light2= h010
lens_model= tamron
lens_focal= 8
fovx= 188
fovy= 141
pixel= 0.1469
focal_distance= 375
aa_calib= 0.0032
exp_calib= 1.36
img_vol= 0.93
xsize= 1280
ysize= 960
```

9. Convert area to equivalent spherical diameter(ESD), adding a column for ESD to the .bru file
10. Each pixel is 148 µm^2 in the UVP images, so assuming a sphere would be photographed as a circle.
11. Based on the range of ESDs, create a log-spaced vector for size bins (example: 100 µm to 3 cm)
12. Tally the number of particles detected whose ESD are in each size bin
    a. For the whole station
    b. Within each depth bin
13. You will end up with a 3-dimensional block of data. This is the concentration size distribution, which is a concentration (count per liter) of the number of particles 1) at each depth, 2) at each station, 3) in each size bin.